Title	Influence of rare earth metal added to electrode on plasma characteristics in gas metal arc welding
Author(s)	Methong, Titinan
Citation	大阪大学, 2018, 博士論文
Version Type	VoR
URL	https://doi.org/10.18910/69578
rights	
Note	

Doctoral Dissertation

Influence of rare earth metal added to electrode on plasma characteristics in gas metal arc welding

Methong Titinan

January 2018

Division of Materials and Manufacturing Science
Graduate School of Engineering
Osaka University

Contents

Chapter 1

Introduction and literature review

1.1 Background and motivation

Gas metal arc welding (GMAW) is a welding process that has been commercially available for around 60 years. The basic operation of the GMAW process occurs when an electrical arc is established and maintained between a base material and a continuously feed wire electrode. The molten weld pool is shielding from the atmospheric conditions by an envelope of shielding gas that is flowed continuously around both the wire filler metal feeding in the weld pool and the weld pool itself. The formation and transfer of metal droplets to the weld pool are governed by the balance of forces. They are also affected by the heat transfer from the arc plasma. For this reason the energy source characteristics of the GMAW strongly depend on physical properties of the arc plasma.

During welding, molten metal from a consumable wire electrode is transferred to a workpiece metal under various modes of metal transfer. The mode of metal transfer depends on various welding parameters and has an important influence on welding quality. The most common transfer modes in GMAW are: short-circuit, globular, and spray transfer [1]. Direct current electrode positive (DCEP) polarity has the characteristics of deep penetration, very good arc stability, and the ability to operate in any of the metal transfer modes. Direct current electrode negative (DCEN) polarity has the characteristic of low penetration, higher wire melting rates for a given current, and low heat input, but has been largely limited to globular transfer. As a result of the globular transfer, DCEN polarity suffers from stability problems and therefore has had very limited use [1-5].

However, GMAW wire electrode has been developed by adding rare earth metal elements as the stabilizing elements into wire electrode [57]. One of the main feature of the rare earth metal-added wire electrode is the low spatter welding process. The rare earth metal-added wire electrode demonstrated better arc stability, smooth metal transfer and produce smaller metal droplet size comparing with wire electrode diameter. This transfer phenomenon can be classified as spray transfer mode. Nevertheless, only few research group studies arc plasma characteristic of GMAW process with metal droplet transfer behavior. Likewise, the effect of rare earth metal element on plasma characteristics are not completely understood mainly due to the difficulty involved in performing accurate measurements.

1.2 Objective and focus

In this research, the experimental measurement of the arc plasma characteristics of GMAW process with rare earth metal added wire electrode are presented. The experimental measurement were compared with arc plasma characteristics of conventional wire electrode with different shielding gas composition of argon and carbon dioxide. Moreover, the metal transfer behaviors were investigated by high-speed color camera. The arc plasma temperature, metal vapor concentration and electrical conductivity were obtained using emission spectroscopic technique. The main objective of the study is to understand the arc plasma and metal transfer behaviors of GMAW process for the conventional wire electrode and rare earth metal added wire electrode. Pure carbon dioxide, pure argon and mixture between carbon dioxide and argon were used in this study.

1.3 Gas metal arc welding and process review

Welding is the most common method used for joining materials. When compared to other joining processes, such as riveting or bolting, welded structures tend to be stronger, lighter-weight and cheaper to produce. There are over 100 different welding processes that can be employed, but GMAW is the most commonly used process today. The initial development of GMAW during the late 1940s focused on joining reactive metals such as aluminum and magnesium [1-2]. These metals were difficult to join with the standard Shielded Metal Arc Welding (SMAW) process of the time because they oxidized readily with the decomposition products of the flux that coated the finite-length metal electrodes. The GMAW process differed significantly with its use of continuously fed spools of electrode wire and argon gas as shielding to protect the molten metal from chemical reactions.

A schematic diagram of a standard GMAW setup is shown in Figure 1.1. The key pieces of equipment are the power source, the wire feeding mechanism, the welding torch, and the workpiece. The process uses a continuous metal wire electrode coiled on a spool that is fed through the wire feeder to the welding torch. At this point, the electrical current from the power source is transferred to the electrode through the contact tip. The wire then encounters the electric arc. The arc is maintained between the electrode and the workpiece and is controlled by the welding power source. The heat produced from the arc melts both the workpiece and the electrode, creating a molten weld pool.

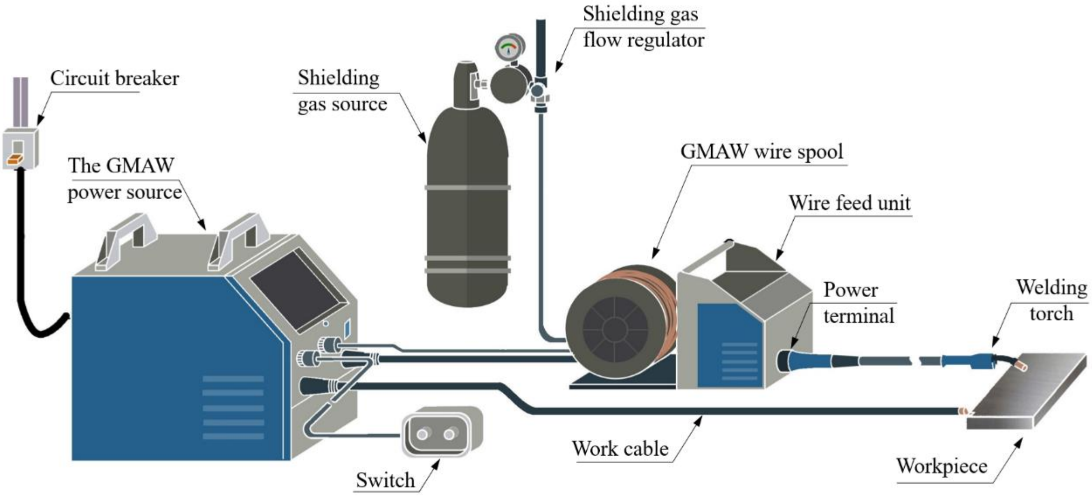

Figure 1.1 Schematic layout of the welding circuit for a typical GMAW process.

At the arc region, molten droplets produced at the end of the electrode are transferred across the arc into the weld pool. The droplets can be transferred in a variety of ways and this detail of GMAW is of primary importance in the current study. The next section describes the phenomenon known as metal transfer.

1.4 Metal transfer modes

The molten droplets of electrode metal can be transferred to the workpiece in a variety of ways that depend on factors including, but not limited to, current, voltage, shielding gas composition, electrode diameter, and electrode material [3 – 6]. The metal transfer modes occurring during GMAW can be divided into two main groups, short-circuiting and free-flight. Each of these groups can then be divided into smaller subgroups.

1.4.1 Metal transfer mode classification

Lancaster [7] wrote one of the most comprehensive reviews on the transfer of metal during arc welding. The International Institute of Welding (IIW) has classified this metal transfer into different categories. They are shown schematically in Figure 1.2. During short-circuiting transfer, the electrode periodically contacts the weld pool. The electrode never contacts the weld pool during free flight transfer; molten droplets detach from the electrode, travel through the arc, and deposited in the weld pool. The six other drawings represent different droplet morphologies that are seen during free-flight transfer. Further classification is given in Table 1.1.

The free-flight metal transfer mode that operates depends on several variables. For a given wire diameter and shielding gas, the voltage and wire feed speed are the main variables that control metal transfer mode. Current and wire feed speed are directly proportional to each other, as described in Section 1.5. At low welding currents in an argon-reached atmosphere, the system operates in drop transfer, also known as globular transfer. As current increases, the metal transfer mode shifts from drop to projected spray. This transition is unique to the consumable electrode processes. It was first reported by Lesnewich [8] and has seen extensive characterization since then. Figure 1.3 shows the characteristic changes that occurring during the transition. The transition is marked by a variety of changes in the system, including a rise in droplet detachment frequency and a correlating decrease in droplet volume. A second characteristic change that occurs in the transition region is the shift in arc attachment point. Many researchers [10 - 14] have concluded that the arc is supported beneath the droplet during globular metal transfer and completely envelopes the droplet in spray mode. So as the welding current increases, the area of the anode spot becomes larger. Once the area of the anode spot exceeds the area of the exposed droplet, the transition from globular to spray mode occurs.

Table 1.1 International Institute of Welding classification of metal transfer [9]

Designation of transfer type		Welding processes (examples)
1.	Free flight transfer	-
1.1	Globular transfer	-
1.1.1	Drop transfer	MIG welding
1.1.2	Repelled transfer	MAG welding with CO_2
1.2	Spray transfer	MIG welding, MAG welding with gas mixtures
1.2.1	Projected transfer	MIG welding of Al-alloys, Pulsed-arc welding
1.2.2	Streaming transfer	MAG welding with gas mixtures
1.2.3	Rotating transfer	Plasma-MIG welding, MIG and MAG welding with high current density
1.3	Explosive transfer	Metal arc welding
2	Bridging transfer	-
2.1	Short-circuiting transfer	MAG welding with short arc process
2.2	Bridging transfer without interruption	Welding with cold or hot wire addition -
3	Slag-protected transfer	-
3.1	Flux-wall guided transfer	Submerged arc welding
3.2	Other modes	Metal arc, electro slag, cored wire

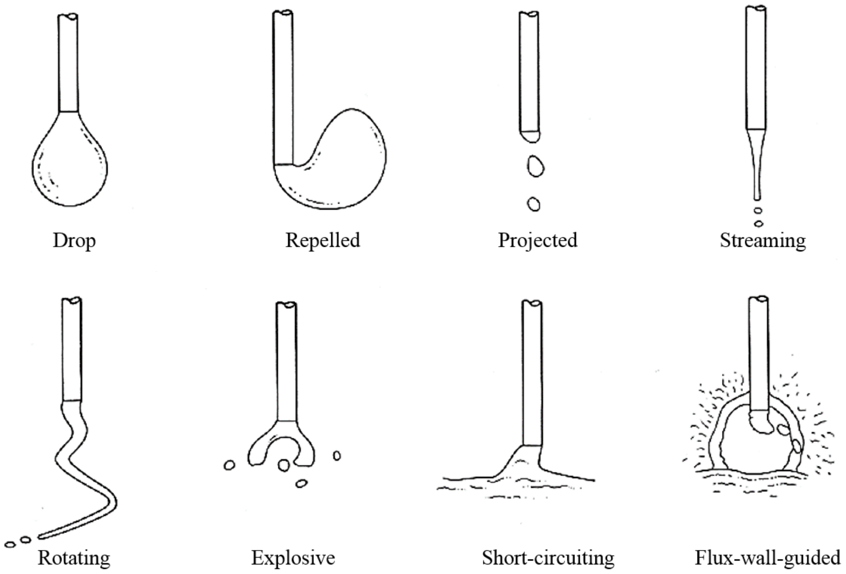

Figure 1.2 Metal transfer modes in arc welding according to the IIW classification. [7]

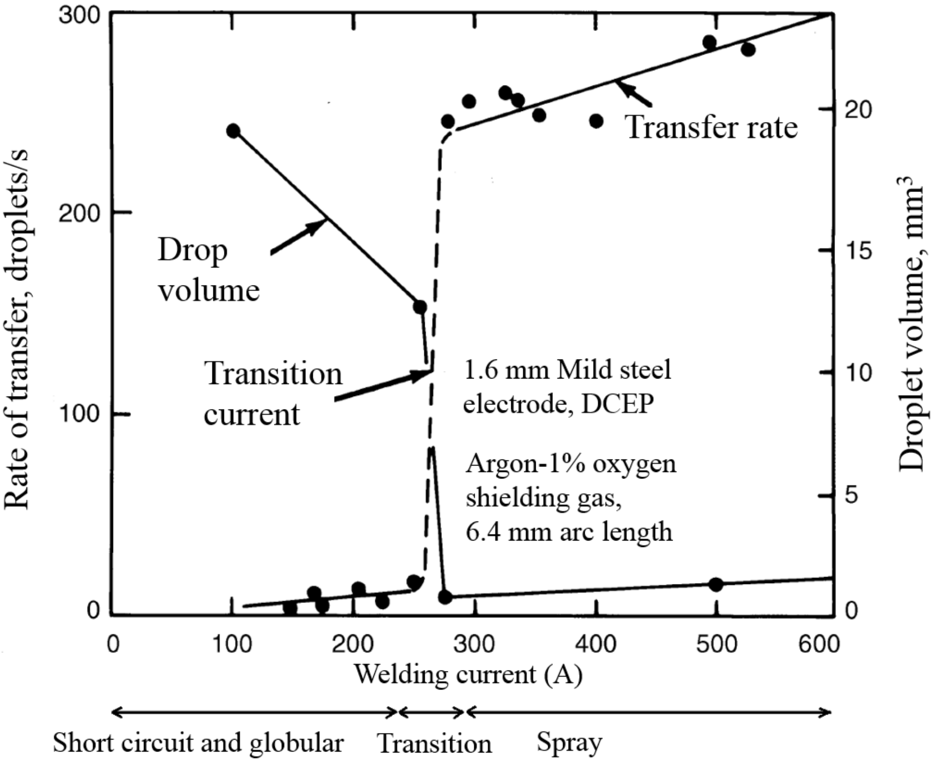

Figure 1.3 Effect of current on droplet detachment frequency and droplet volume in 1% oxygen-argon shielding gas. [7]

1.4.2 The physics of metal transfer mode

The physics involved in metal transfer are complex. Several dominating forces act on the liquid droplet as either attaching or detaching in nature. Researchers [11, 14 – 19] have shown four main forces on the droplet during GMAW in argon atmospheres: gravity, shielding gas drag, surface tension and electromagnetic (Lorentz) force. The Lorentz pinch force acts radially inward and down [10] in argon atmospheres. They are shown schematically in Figure 1.4. The balance of these forces determines the shape, volume and frequency of detachment of droplets formed at the tip of wire electrode. In addition to this, the instantaneous temperature and temperature distribution at the end of wire play an important role in the material transfer.

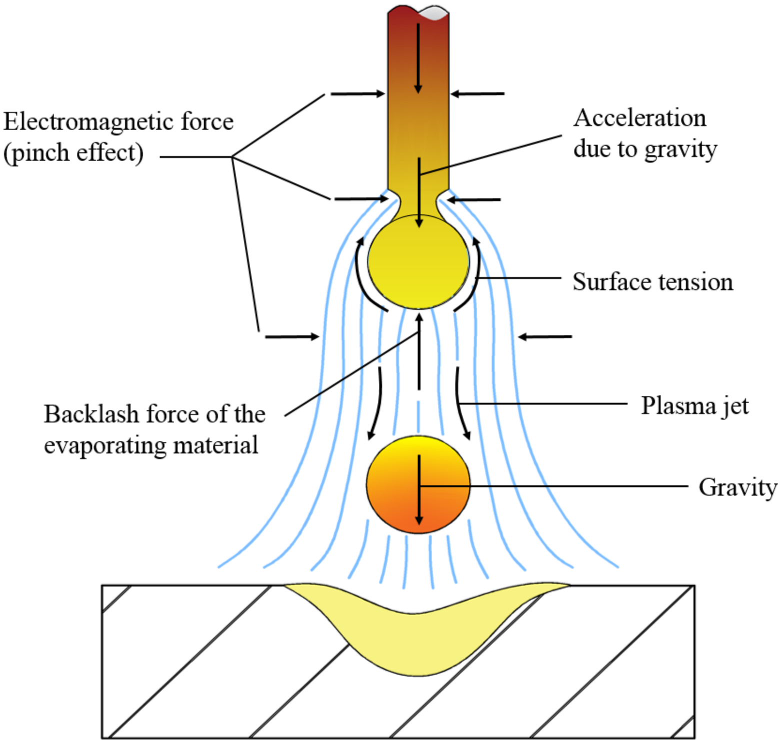

Figure 1.4 Forces at metal transfer in GMAW process.

At the transition, a change in the force balance attributes to the change in droplet size and geometry. Gravity and surface tension are the balancing forces for low-current globular transfer. When welding current is increased, the anode spot covers the droplet, and current flow geometry acts to constricts the size of the droplet and propel it away from the electrode. At very high currents, a liquid jet of metal may form because Lorentz forces become dominant [21 – 22]. Significant changes occur to the geometry of the liquid droplet and the anode spot changes as the metal transfer mode transitions from globular to spray. These changes also control heat transfer in the arc plasma region.

1.5 GMAW process parameters

The GMAW process is able to produce high quality welded for a variety of different applications. This is due to the flexibility of welding parameters. Figure 1.5 shows the basic parameters and terminology for a standard GMAW torch setup. Two primary adjustments are made on a standard GMAW setup: wire feed speed

(WFS) and welding arc voltage. By adjusting these two parameters, the welding current and arc length can be controlled. As shows in Figure 1.5, electrode extension is the length of electrode measured from the distal end of the contact tip to the arc. The summation of arc length and electrode extension gives the contact tip to work distance (CTWD). Shielding gas composition and CTWD can be directly controlled with a gas mixer and adjustable fixture, respectively. This section covers the variables associated with GMAW and how they influence metal transfer.

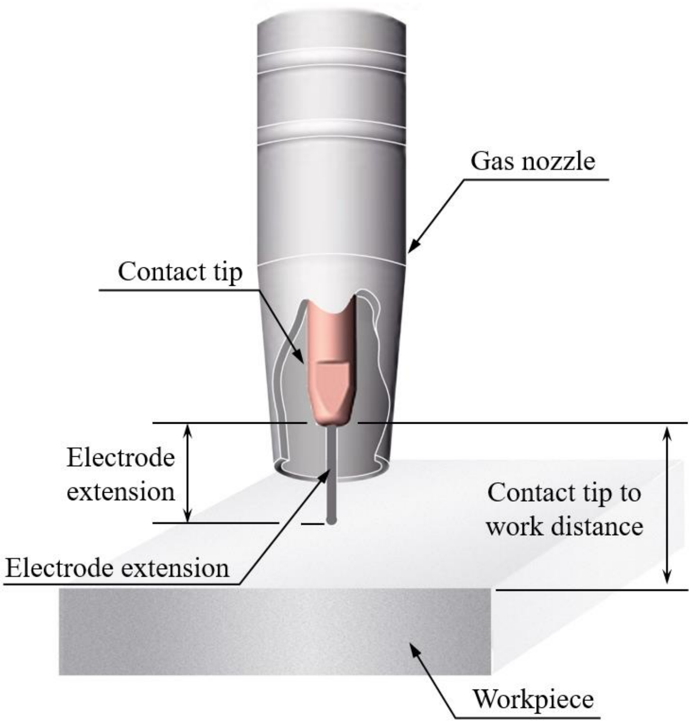

Figure 1.5 Common terminology and basic parameters.

1.5.1 Welding arc voltage

On a standard of GMAW machine, arc voltage and arc length are often used interchangeably, but they are different. For a given welding setup, arc voltage and arc length vary in similar ways. However, for a given arc voltage, the arc length will change with shielding gas types, current, and electrode extension. If all other variables remain constant, an increase the voltage setting will increase arc length. Arc voltage is a key element during process monitoring.

1.5.2 Welding current

During GMAW, the welding current is roughly proportional to the wire feed speed. It is one of the main inputs for current density and has a large influence on the magnitude of Lorentz forces. The welding current also contributes significantly to the resistive heating of the electrode extension. Furthermore, the welding current has the greatest effect on penetration. Penetration is increased by using higher currents with a corresponding increase in wire feed speed.

1.5.3 Welding power source

The welding power source delivers electrical power to the electrode and the workpiece to produce the arc. For the vast majority of GMAW applications, direct current electrode positive (DCEP) is usually used, the positive lead is connected to the welding torch and the negative lead to the workpiece.

Power sources can be designed and built to provide either constant current (CC) or constant voltage (CV). Early applications of the GMAW process used constant-current power sources. Constant-current characteristic maintain a relatively fixed current level during welding, regardless of variations in arc length.

1.5.4 Electrode extension

Electrode extension, commonly called stick-out, has a significant influence on the metal transfer modes due to the resistive heating in this region. Figure 1.5 illustrates that, for a given current, an increase in extension results in greater resistive heating prior to encountering the arc.

1.5.5 Shielding gas

The shielding gas used in welding has a significant influence on metal transfer. A variety of gases are available for use in the GMAW process. Depending on the gas, it is classified as inert or active. Argon and helium do not react with the liquid metal, they are inert. Carbon dioxide, oxygen, Hydrogen, and nitrogen are multi-atomic molecules that dissociate when exposed to temperatures in the arc and are able to react with the metal. Many times, a mixture of gases is used that is suited for the particular application. The gas affects the plasma properties and the flow of current as it travels through the electrode and plasma. Shielding gas composition also affects the surface tension of the metal. This leads to changes in the Lorentz pinch force in both the plasma and the electrode. Generally, the manufacturer of the electrodes chosen for the welding application is a good source of information on selecting the optimum shielding gas for use with their electrodes.

Argon shielding gas

The atomic symbol for argon is Ar, and it is an inert gas. Inert gases do not react with any other substance and are insoluble in molten metal. One hundred percent argon is used on nonferrous metals such as aluminum, copper, magnesium, nickel, and their alloys; but pure argon is not normally used for making welds on ferrous metals. Because argon is denser than air, it effectively shields welds by pushing the lighter air away. Argon is relatively easy to ionize. Easily ionized gases can carry long arcs at lower voltages. This makes it less sensitive to changes in arc length.

Argon shielding gas mixtures

Oxygen, carbon dioxide, helium, and nitrogen can be blended with argon to change argon’s welding characteristics. Adding reactive gases (oxidizing), such as oxygen or carbon dioxide, to argon tends to stabilize the arc, promote favorable metal transfer, and minimize spatter. As a result, the penetration pattern is improved, and undercutting is reduced or eliminated. Adding helium or nitrogen gases (nonreactive or inert) increases the arc heat for deeper penetration.

Argon-carbon dioxide mixtures (up to 20% CO_2) are used on carbon and low-alloy steels, and to a lesser extent on stainless steels. The addition of carbon dioxide may produce adverse effects such as an increase in spray transition current, increased spatter, deeper penetration, and decreased arc stability. Argon-carbon dioxide mixtures are primarily used in short-circuiting transfer applications, but are also usable in spray transfer and when pulsed currents are employed.

Carbon dioxide shielding gas

Carbon dioxide is a compound made up of one carbon atom (C) and two oxygen atoms (O_2), and its molecular formula is CO_2. One hundred percent carbon dioxide is widely used as a shielding gas for GMAW of steels. It allows higher welding speed, better penetration, good mechanical properties, and costs less than the inert gases. The chief drawback in the use of carbon dioxide is the less-steady arc characteristics and a considerable increase in weld spatter. The spatter can be kept to a minimum by maintaining a very short, uniform arc length. CO_2 can produce sound welds provided a filler wire having the proper deoxidizing additives is used.

1.5.6 Electrode diameter

The electrode diameter is an important parameter in GMAW because it has a large influence on the deposition rate, the welding current and the subsequent heat input to the workpiece. Usually, the size of the electrode is matched to the thickness of the workpiece [20].

1.5.7 Travel speed

In a standard GMAW setup, the welding torch advances in relation to the seam being welded. This can happen either by moving the welding torch against a stationary workpiece or moving the workpiece against a stationary torch. The travel speed controls the amount of material and heat that is deposited on the workpiece and the cooling rate. The experimental setup used for testing uses a stationary torch and no workpiece, so travel speed is not an issue.

1.6 The physics of gas metal arc welding arc

Detailed modelling of GMAW with carbon dioxide shielding gas by Haidar and Lowke [23] have successfully simulated some behaviors of the GMAW arc plasma. For the welding current from 325 to 400 A, formations of both large and small droplets were predicted over a period of 250 ms. The majority of the metal transfers occur when larger droplets fall from the electrode, as their weight exceeds surface tension and other upward forces. The production of a large droplet is attributable to arc constriction beneath the droplet. When arc plasma is constricted, the current pathway is concentrated to the molten metal droplet at the arc attachment point and the upward axial component of the electromagnetic force increases. The arc constriction, which creates the undesirable effects on GMAW with carbon dioxide shielding gas, is caused by non-monotonic variation in the thermal conductivity of the carbon dioxide gas with temperature, while monatomic gases such as argon exhibit thermal conductivities that monotonically increase with temperature [24].

Zielinska et al [25] investigated arc plasma properties by optical imaging and emission spectroscopy for pure argon and mixtures of argon and carbon dioxide, including arc temperature, electron density and transition current, and found that increasing the proportion of carbon dioxide could resulted in a reduction of arc conductivity and an increased transition current. In recent years, there have been many research efforts aimed at studied the behavior of Fe vapor with different shielding gases. Their results showed the existence of a local temperature minimum in the arc axis due to the presence of metal vapor for gases with a high proportion of argon, which disappeared in pure carbon dioxide shielding gas [26]. This can be explained by the higher metal vapor concentrations near the arc axis will increase the radiative emission coefficient [27 – 29].

Argon–CO_2 mixtures shielding gas are widely used in steel welding due to the low cost of carbon dioxide compared to oxygen. The use of argon–CO_2 mixtures shielding gas not only overcomes issues of unstable arc attachment region and undesired weld shape in pure Ar arc welding of steels, but also leads to less spatter than pure carbon dioxide arc welding [30 – 31]. Increasing carbon dioxide content in the mixture increases the heat input to the weld and promotes deep penetration of the weld. Warinsiriruk E. [32] studied the effect of carbon dioxide addition in argon gas mixture by using high speed camera. The results showed clear behaviour in three regions; short circuit, globular and spray transfer. Soonrach R. [33] studied the effect of oxygen addition in argon and carbon dioxide gas mixture on metal transfer behaviour in GMAW process. The results shows that the mixed mode of globular and spray transfer occurs when welding current above 250 A.

1.7 Thesis outlines

Chapter 1: Introduction and literature review

In this chapter, a general overview of the problem statement being studied, the background and motivation of this study are presented. A short overview over the GMAW process arc given, which includes the process parameters, GMAW equipment, metal transfer modes and the physics of metal transfer mode. The GMAW process is described in greatest detail included advantage and disadvantage of the process.

Chapter 2: Fundamental physics of arc plasma and measurements method

The fundamental of physics of arc plasma including the arc plasma characteristics measurement methods are described in this chapter. The objective is to present the measurement process of the arc plasma characteristics, particularly for the spectroscopic methods. A brief overview of spectroscopic methods of arc plasma properties are also presented.

Chapter 3: Experimental set-up

The experimental set-up, procedure for the experiments used in this research are given in this chapter. The experimental set-up is divided into different sections as experimental setup for emission spectroscopic system, experimental setup for the observation of metal transfer behaviors that cover the design, setup, equipment and procedure that are made. The welding materials, welding parameters and experimental procedure are presented. The measurement methods for GMAW plasma are also given in this chapter.

Chapter 4: Experimental results

The result of optical emission spectroscopic investigation and visualization of arc plasma with metal transfer are presented. The results is covered two different type of wire electrodes (conventional wire electrode and rare earth metal added wire electrode). The effect of shielding gas composition and electrode polarity are discussed through the arc plasma properties and metal transfer behaviors.

Chapter 5: Mechanisms of GMAW using carbon dioxide shielding gas

This chapter presents mechanisms of arc plasma characteristics, metal droplets transfer mode and surface temperature of metal droplet in gas metal arc welding with conventional carbon steel electrode (MG-50) and rare earth metal added wire electrode (KC-500) by compared between direct current electrode negative polarity and direct current electrode polarity

Chapter 6: Conclusions

The conclusion for each section are summarized and discussed in term of arc plasma characteristic and metal transfer behaviors. The effect of rare earth metal added on plasma properties also discussed in this chapter.

Chapter 2

Fundamental physics of arc plasma measurements method

2.1 Spectroscopic methods of arc plasma properties

2.1.1 Basic principles of spectroscopic methods

The measurement apparatus typically consists of two parts, a focusing system and a spectroscopic instrument. The focusing system contains lenses, mirrors and dichroic beam splitter, the role of which is to image the arc at a known magnification onto the entrance slit of the spectrometer or monochromator. The monochromator consists of a dispersive instrument that images a portion of the spectrum onto the exit plane which is then recorded using high-speed video camera.

2.1.2 Spectroscopic measurements of GMAW arc plasma

Measurements of GMAW arc plasma are more difficult than those of GTAW arc plasma. The arc is not steady and stable because metal droplets are continually forming at the wire anode, then detaching and falling through the arc plasma. These metal droplets also interrupt the line of sight in spectroscopic and laser laser-scattering measurements. As a consequence, there have been many fewer measurements of GMAW arc plasma.

Ton [44] presented measurements of the temperature distribution and composition for plasma–MIG welding. This is a hybrid process, in which a filler metal is introduced into an arc between a tungsten electrode and the workpiece. Both the filler wire and tungsten electrode are connected to power supplies, with a potential difference between the electrode and the wire, and the wire and the workpiece, with the electrode and wire having the same polarity. Results were presented for an argon arc with a carbon steel filler wire, and for both positive and negative electrode and wire polarities. In all cases, the arc consisted of a highly luminous inner core and a surrounding plasma of lower luminosity. Temperatures were measured by comparing the intensities of different spectral lines. The central part of the arc was found to contain iron, manganese, copper, calcium and argon at temperatures in the range 6,000 to 7,000 K, while the outer region showed only argon spectral lines and was at a temperature of about 13,000 K. The metals detected were all present in the filler wire. Ton calculated that the electrical conductivity and therefore the current density in the central region were much smaller than in the outer region.

Zielinska et al [25] measured the temperature distribution in GMAW spray-transfer mode and globular-transfer mode. Results were given for arcs in pure argon shielding gas and in mixtures of argon and 5.4% and 20.2% carbon dioxide by mole, with a mild steel anode. In the first two cases, spray transfer occurred, while globular transfer occurred for the higher carbon dioxide concentration. In all cases, a bright central region with strong emission from iron species was observed. The Stark broadening of an Ar I and an Fe I spectral line was measured; together these measurements allowed the electron temperature and number density to be determined, independent of any assumption of local thermodynamic equilibrium (LTE). For the arcs in argon and argon with 5.4 % carbon dioxide shielding gas by volume, the electron temperature was found to have a local radial minimum on axis, while for the arc in argon with 20.2 % carbon dioxide, the temperature was maximum on axis. For example, for the pure argon arc, the electron temperature was 8,500 K on axis for axial positions 3 mm and 4.5 mm above the workpiece, and the maximum temperature of 11,500 K occurred at radius 1.3 mm and 2.3 mm.

Valensi et al [28] present a further investigation of the argon GMAW arc in spray-transfer mode. They again used Stark broadening of an Ar I and an Fe I spectral line to measure electron temperature, but also measured the excitation temperature with a Boltzmann plot of three Fe I lines. The good agreement suggested that the arc is in partial LTE (i.e. the electron temperature is equal to the excitation temperature of the atoms).

Zielinska et al [45] present results indicating that a GMAW arc can be used to determine the Stark parameters of atomic metal spectral lines, and apply this to the measurement of the Stark parameters of Mn I and Fe I lines, as well as the temperature dependence of the broadening of one of these lines. They suggest that because the composition of the wire electrode is easily altered.

Rouffet et al [27] measured the properties of a GMAW arc operating in one-drop-per-pulse mode. A steel wire and argon shielding gas were used, and measurements were made in the high-current phase of the cycle, for which the current was 450 A. A Boltzmann plot of Fe I lines was used to determine temperature, while the electron density was obtained from the Stark broadening of an Ar I line. The latter measurement was independent of the assumption of LTE. The temperature was measured to be about 8,000 K in the central region of the arc, rapidly increasing to about 13,000 K at larger radius. The iron concentration was about 60% by mole in the central region, falling to at most a few percent in the hotter regions of the arc. The iron concentration is largest at the start of the high-current pulse, and gradually decreases as the iron vapor diffuses to larger radius over a period of just under 1 ms during the pulse.

Wilhelm et al [26] investigated GMAW operating in the dip transfer mode. A steel wire, and carbon dioxide and argon–oxygen shielding gases were used, and the cold metal transfer process was adopted, in which the current was controlled so that it was minimum during the short circuit and rapidly increased after separation of the wire and workpiece. The emission from Fe I lines, and O I or Ar I lines, depending on the shielding gas, was measured during the current pulse after the short circuit. The emission from iron was strongly concentrated in the arc axis, and increased rapidly over the first millisecond or so of the pulse, before becoming reasonably steady. The oxygen and argon concentration peaked on the arc axis at the start of the pulse, but the peak subsequently moved radially outwards. Iron vapor mole concentrations on the arc axis were estimated to be about 25% for argon–oxygen shielding gas, about 75% for carbon dioxide, with temperatures of around 8,000 K in this region. By analyzing the radial dependence of the measured line emission, the arc voltage, and calculated thermophysical properties of the plasma, it was concluded that the arc was more strongly constricted when the shielding gas was carbon dioxide.

2.2 The physical properties and characteristics of arc plasma

The fusion welding of metals relies for its effectiveness on the use of a heat source of power density in the range 10^6 to 10^{13} W/m^2. Most commonly the heat source is an electric arc and the power density lies between about 3 x 10^6 and 1 x 10^{10} W/m^2. The arc temperature is highest in the gas near to the electrode, where it may range from a value of 6,000 K to 20,000 K or more and lowest in the vicinity of the weld pool. The metal that is melted by the arc may be raised to its boiling point at the tip of the electrode. Information is therefore required as to the physical properties of engineering metals in the range from the melting point to boiling point, and gases within the temperature range indicated. These properties will be discussed below, firstly for gases and secondly for liquid metals. They will be divided into two categories; firstly the thermodynamic properties such as internal energy, specific heat, dissociation, ionization and secondly the transport coefficients such as those of thermal conductivity, diffusivity and viscosity.

2.2.1 Dissociation and ionization

As a gas is heated the individual molecules acquire more energy. At low temperatures this energy is mainly translational: i.e. it is the energy associated with velocity of motion. At higher temperatures diatomic molecules such as hydrogen, nitrogen or oxygen absorb energy firstly by rotation and secondly by vibration in and out movement of the two atoms relative to each other. When the vibrational energy reaches a sufficiently high level it may rupture the valence bonds holding the two atoms together, causing them to dissociate into a monatomic state. At higher temperatures still, part of the energy is absorbed by the outer electron band of individual atoms, and eventually causes detachment of one of the outer electrons - the atom ionizes into one electron and a positively-charged ion. Further increase in temperature may cause multiple ionization, when the atoms lose more than one electron.

2.2.2 Transport phenomena

The transfer of energy in a gas results from the interaction of the particles of which it is composed. These individual particles are in a state of continual random motion, and energy is transferred from one particle to another by collisions. Such collisions are said to be elastic if the total kinetic energy of the particles involved remains unchanged. Quantitative relationships such as the distribution of velocity, frequency of collision, etc., may be determined by the kinetic theory of gases, and from these basic relationships it is possible to obtain expressions for electrical conductivity and other properties.

2.2.3 Thermodynamic properties and characteristics of high-temperature carbon dioxide and argon gas

The most significant difference between GMAW processes using carbon dioxide and argon-based shielding gases is that the carbon dioxide process does not exhibit a spray transfer mode. For low currents the carbon dioxide shielding gas process operates in short circuit transfer mode. The overall behavior is similar to that for argon, but spatter levels tend to be higher and the bead finish is not as smooth. These differences are due to the lower surface tension of molten steel in carbon dioxide, and the non-axial forces generated by the arc in carbon dioxide.

The production of a large droplet is attributed to the high degree of arc constriction in carbon dioxide shielding gas at DCEP polarity. The corresponding constriction of the current in the molten droplet at the arc attachment point causes an increase in the upward axial component of the magnetic force in the liquid. The rapid formation of very small droplets at the arc root is also due to the same constriction of current at that point, creating an electromagnetic pinch force. In contrast, the “arc root” in argon encompasses a much larger area of the droplet. The constriction of the current occurs at the top of the droplet, tending to pinch off the entire molten droplet rather than a small volume at the base.

The arc constriction, which creates the undesired behavior of the GMAW process with carbon dioxide shielding gas, is caused by the non-monotonic variation in the thermal conductivity (K) of the gas with temperature. While monatomic gases like argon exhibit a specific heat that rises steadily with temperature (T), the addition of a dissociative gas such as carbon dioxide creates the relationship between specific heat ($W.m^{-1}.K^{-1}$) and Temperature (K) as shown in Figure 2.1. The rise in specific heat is due to dissociation of the gas at those particular temperatures. The arc is concentrated, or constricted, to a smaller radius at a given current, since the electrical conductivity of gases increases rapidly with temperature, as shown in Figure 2.2. The electrical conductivity of carbon dioxide is markedly higher than argon above 17,000 K.

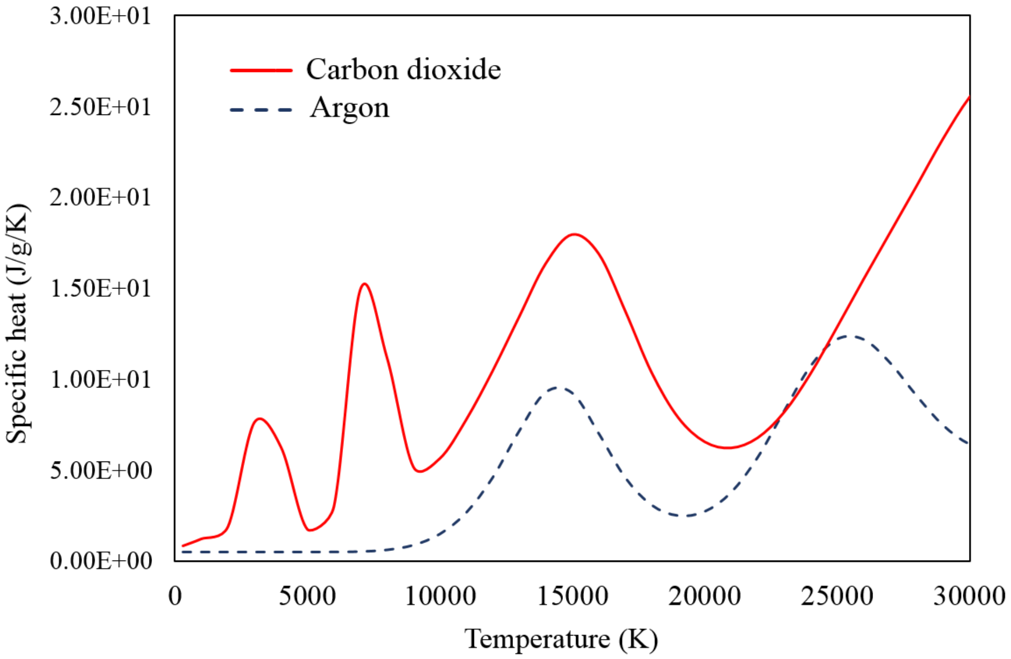

Figure 2.1 Relationship between specific heat and temperature for carbon dioxide and argon gas [59].

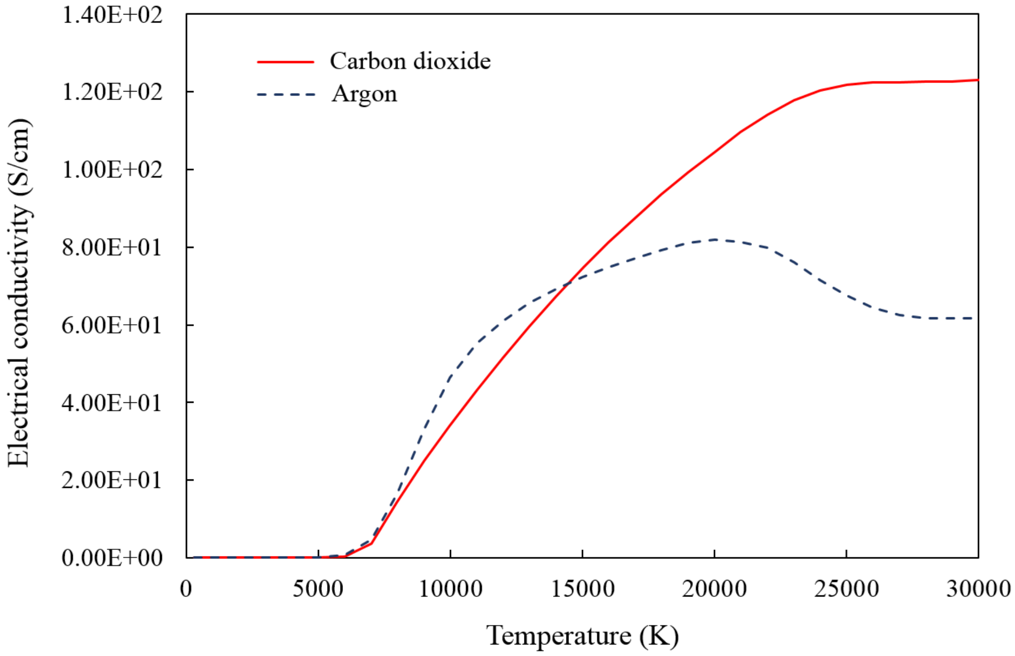

Figure 2.2 Relationship between electrical conductivity and temperature for carbon dioxide and argon gas [59].

2.3 Plasma composition

For the sake of simplicity, the following considerations will be based on thermal plasmas that contain only one type of ion, namely, singly ionized atoms. If such a plasma is generated from a monatomic gas (for example argon gas), then only three species compose the plasma-electrons, neutral argon atoms, and positive argon ions [34].

$$\mathrm{Ar} \leftrightarrow \mathrm{Ar}^{+} + e$$

The plasma composition in this situation is described by a set of equations: the Eggert-Saha equation, Dalton's law, and the condition for quasineutrality of the plasma:

$$\frac{n_e n_i}{n} = \frac{2Q_i}{Q}\left(\frac{2\pi m_e kT}{h^2}\right)^{3/2} exp\left(\frac{E_i}{kT}\right) \tag{2.1}$$

$$p = (n_e + n_i + n)kT \tag{2.2}$$

$$n_e = n_i \tag{2.3}$$

In the Eggert-Saha equation (2.1), n_e is the electron number density, while n_i and n represent ion and neutral number densities, respectively, regardless of whether the ions and neutrals are in an excited state or in the ground state; Q_i and Q_i are the partition functions of the ions and neutrals, respectively, h is Planck's constant, and E_i represents the ionization energy. The partition functions are given by

$$Q_i = \sum_s g_{i,s}\, exp\left(-E_{i,s}/kT\right) \tag{2.4}$$

$$Q = \sum_s g_s\, exp(-E_s/kT) \tag{2.5}$$

where $g_{i,s}$ and g_s are the statistical weights of the energy levels of the ions and neutrals, respectively, while $E_{i,s}$ and E_s are the corresponding energy levels of their excited states. The equations for the partition functions imply that the populations of the excited states follow a Boltzmann distribution.

For a given pressure, Equations. (2.1) - (2.3) permit the calculation of the plasma composition as a function of temperature. Since the previously mentioned ionization-energy correction term is primarily a function of the electron (or ion) density, a few iterations are necessary to calculate $n_e(T) = n_i(T)$ and $n(T)$. Figure 2.3 shows the composition of a thermal argon plasma at a pressure of 100 kPa. Since the pressure is kept constant, the total particle number density $n_t = n_e + n_i + n$ decreases with increasing temperature.

If a plasma is generated from a molecular gas (for example, nitrogen, carbon dioxide), the number of possible species comprising the plasma will be increased due to the presence of molecular species. The chemical processes that may occur in the plasma will include dissociation of molecules into atoms and ionization of some atoms. The formation of molecular ions will be neglected. The dissociation process in a carbon dioxide plasma

$$CO_2 \leftrightarrow CO + O$$

can be described by an equation similar to the Eggert-Saha equation. The results for a carbon dioxide plasma at p = 100 kPa are shown in Figure 2.4. For In the range from 5,000 to 8,000 K, carbon dioxide molecules decompose, thus producing CO, O_2, C, O, C_2O, and other species. In this temperature range, electrons are produced mainly by ionization of O_2. Above 8,000 K, monatomic particles and ions as well as electrons become dominant [35].

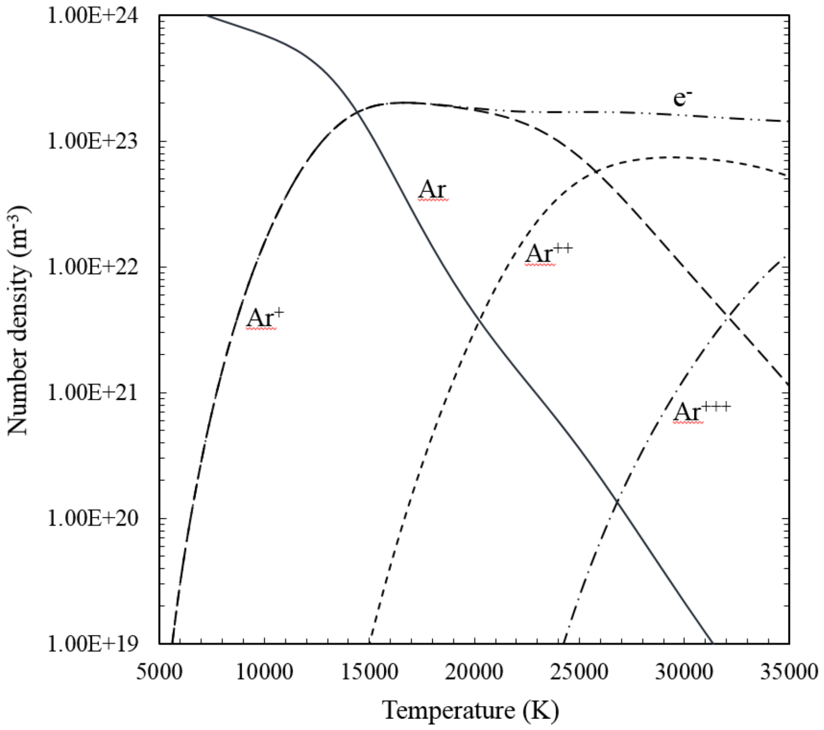

Figure 2.3 Equilibrium composition of argon at pressure of 100 kPa.

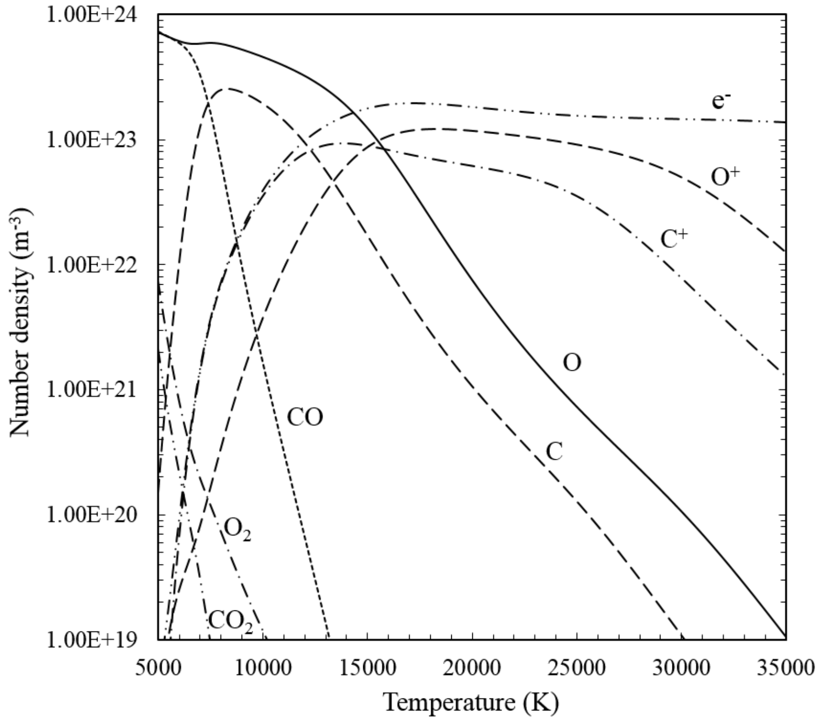

Figure 2.4 Equilibrium composition of carbon dioxide at pressure of 100 kPa.

2.4 Abel inversion method

The inversion of the Abel integral equation is a widely used technique in the study of extended radiation sources [46 – 48]. External measurements of the radiance (W m^{-2} sr^{-1}) produced by the source are used to deduce the radial distribution of the emission coefficient (W m^{-3} sr^{-1}) and hence the radial distribution of such parameters as temperature and density of the emitting matter.

An important aspect of the spectroscopic method refers to the way of capturing luminous intensity of arcs. One must be aware of the fact that is a luminous "line" rather than a point that is measured. As shown in Figure 2.5 and Figure 2.6. Thus, the spectral intensity will be composed by difference energetic states at difference temperatures. The intensity distribution is the same of both direction x and y, it is possible to eliminate this effect by using the Able inversion for the transformation of line-integrated data to localized values. The circular cross section is defined by;

$$x^2 + y^2 = r^2 \quad (0 \leq r \leq R) \tag{2.6}$$

The signal along the vertical view chord, $I(x)$ can be expressed by the local signal, $\varepsilon(r)$, as follows;

$$I(x) = 2\int \varepsilon(\mathrm{r})\, dy = 2\int_x^R \frac{\varepsilon(r)r}{\sqrt{(r^2 + x^2)}}\, dr \tag{2.7}$$

The solution of Equation 2.7 for the circular cross section and the principle Able inversion is given by Equation 2.8

$$\varepsilon(r) = -\frac{1}{\pi}\int_r^R \frac{1}{\sqrt{r^2 - x^2}} \frac{dI(x)}{dx} dx \tag{2.8}$$

Where the R is the maximum plasma radius. The units for the line integrated intensity is $Wm^{-3}sr^{-1}$.

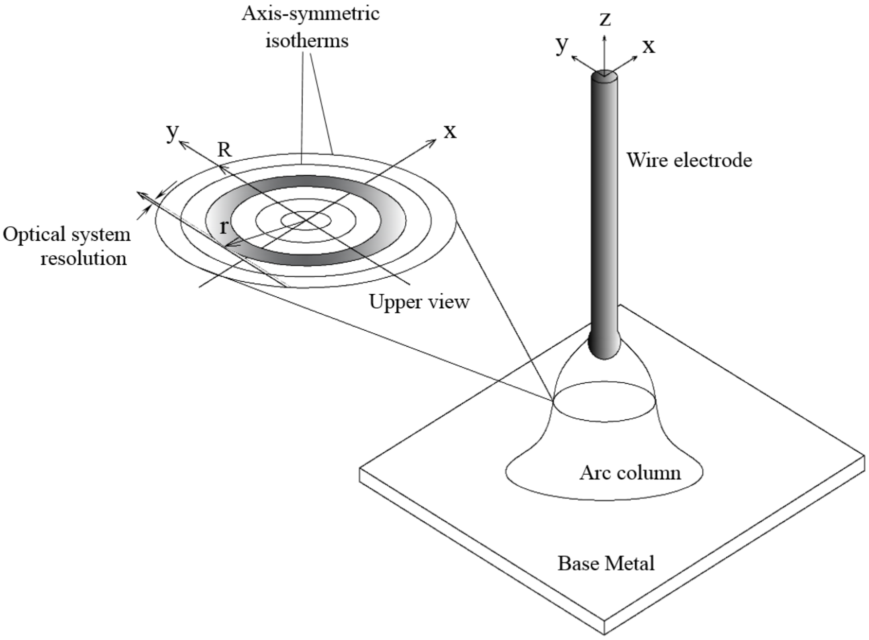

Figure 2.5 Integrated intensity along line of sight of an arc transverse section.

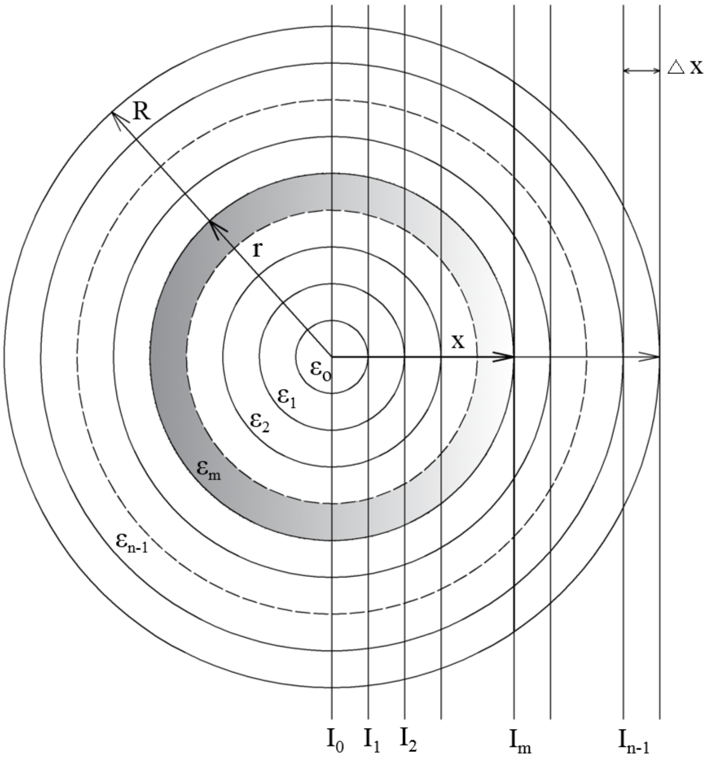

Figure 2.6 Schematic illustration of Able inversion.

2.5 Local thermodynamic equilibrium (LTE) [34]

Local thermodynamic equilibrium (LTE) is a concept in which all thermodynamic equilibrium laws are verified except the Planck radiation law. For a plasma at a given temperature, the LTE condition is valid when the characteristic collision time between electrons and heavy particles is shorter than the characteristic time for any other process taking place in the plasma, particularly the radiative processes. This occurs when the electron density is high enough and plasma flows and gradients are negligible. The knowledge of the equilibrium state of the plasma is an important feature since as the LTE condition is verified it is possible to characterize the plasma by a unique temperature, which considerably simplifies the description of the plasma properties. In addition, for a plasma at LTE, it is possible from the measurement of the temperature and electron density to calculate the emission spectrum of plasma lines by simply applying Boltzmann and Saha equilibrium laws. In this way, the LTE concept, if verified, could be particularly useful for the use of the optical emission spectroscopy technique.

These requirements may be expressed through the concept of a multiple temperature plasma. For a three component plasma separate kinetic temperatures, $T_e,\ T_A,\ T_{A^+}$ may be associated with each of the species. In addition, the excitation temperatures $T_{ex,A}$, and T_{ex,A^+} are defined with the use of a Boltzmann distribution to describe the neutral atom and ionic bound states. The ionization temperature T_I, is associated with the description of the species populations described by the Saha equation. Thus LTE will exist when

$$T_e = T_A = T_{A^+} = T_{ex,A^+} = T_{ex,A} = T_I$$

in which case it is possible to describe to a local thermodynamic temperature T.

2.6 The measurement of spectral lines

In this study, the measurement and analysis of the spectrum of the visible radiation of the GMAW arc plasma are applied in investigations of the welding process in order to find out the temperature distribution of arc plasma and others plasma properties. The spectral lines used in this research were selected from the spectrum of the visible radiation of the GMAW arc plasma with difference type of shielding gas and compared with the database of National Institute of Standards and Technology (NIST) [58]. The experimental setup for measurement spectrum of the visible radiation of GMAW arc plasma have been performed on the motor-driven linear stage. The welding torch has been fixed while the testing plate (JIS G 3101 SS400 with thickness of 10 mm) has been moved at controlled speed. The torch was located perpendicularly to the welding surface. All the experiments were performed by bead-on-plate welding. The measuring system consisted of HORIBA Triax 190, imaging spectrometer and HORIBA Syncerity. CCD detection system. This spectrometer enables to have detailed spectral information of GMAW arc plasma. The tests have been performed using YGW11 MG-50 wire electrode with three types of shielding gas consisted of pure carbon dioxide, pure argon and 80% Ar + 20% CO_2. The main purpose in the measurement was determined the spectrum of GMAW arc light emission. Then, selected suitable spectral lines of oxygen argon and iron. All spectral lines were checked the specific properties from NIST. The results of spectrum of GMAW arc light emission with difference types of shielding gas and wire electrodes were showed in Figure 2.7 – 2.9.

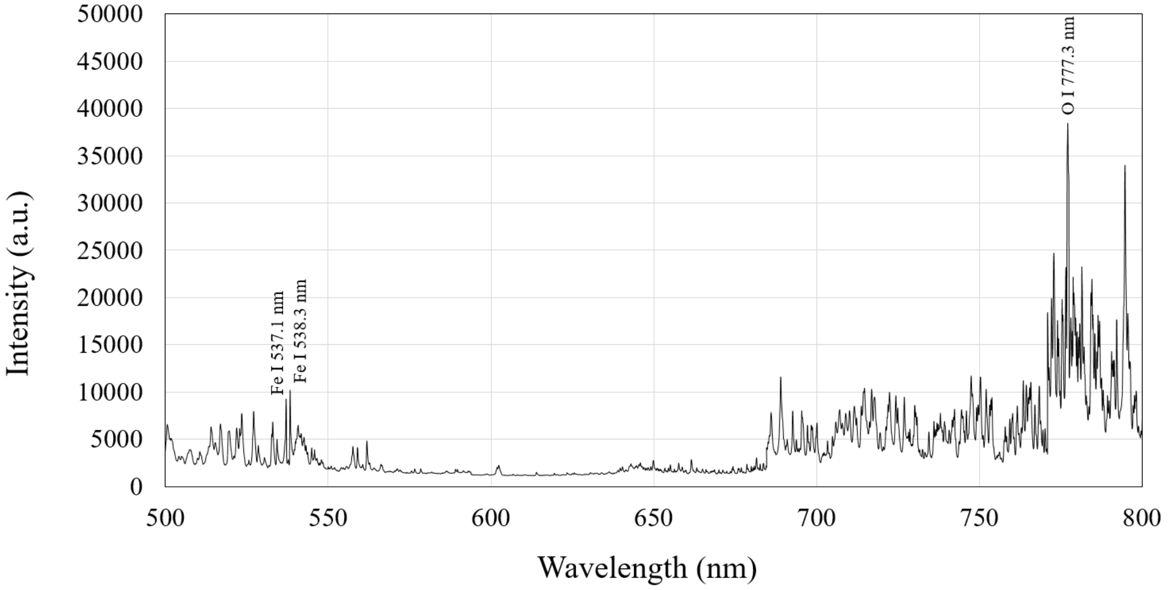

Figure 2.7 The spectrum of GMAW arc light emission with two types of wire electrode using pure carbon dioxide shielding gas.

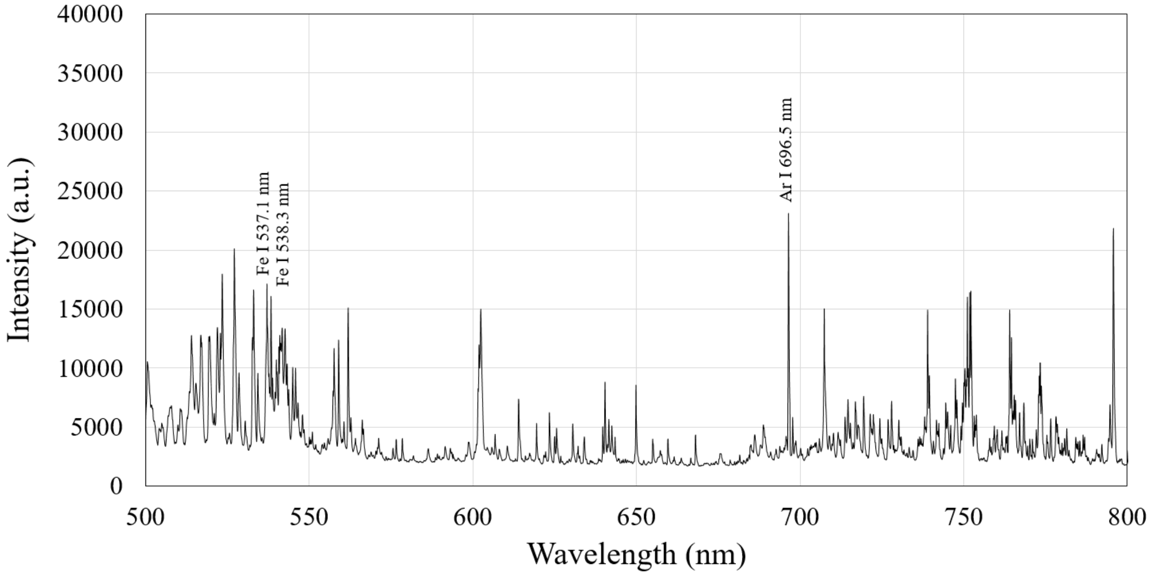

Figure 2.8 The spectrum of GMAW arc light emission with two types of wire electrode using pure argon shielding gas.

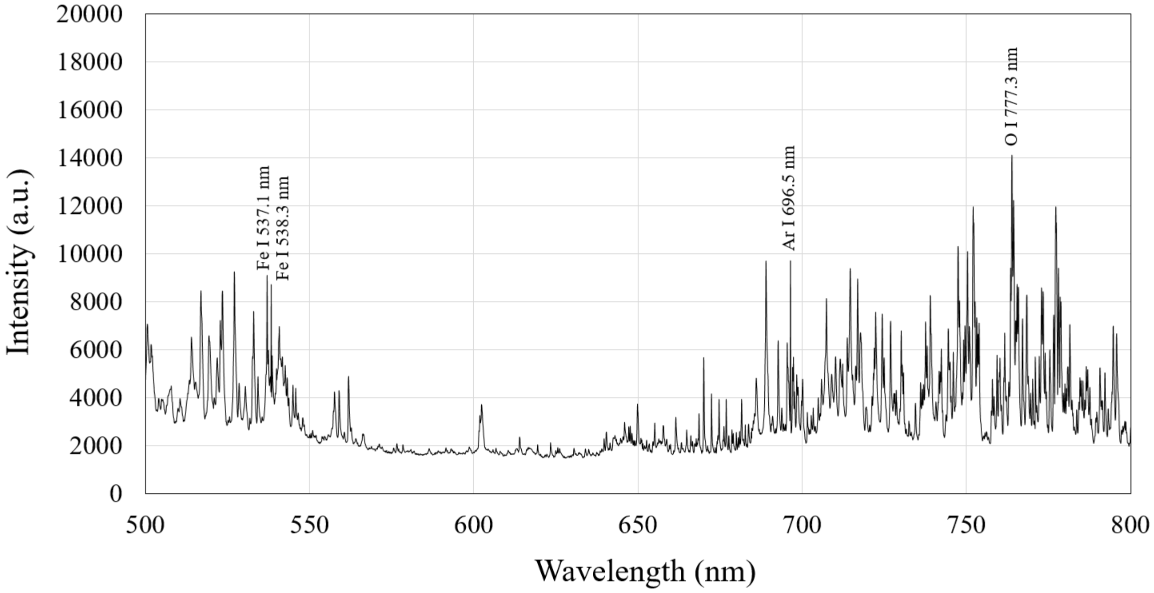

Figure 2.9 The spectrum of GMAW arc light emission with two types of wire electrode using 80% Ar + 20% CO_2 shielding gas.

As a result of the spectrum of GMAW arc light emission, the spectra of Ar I 696.5 nm line was chosen to measure arc plasma temperature of GMAW with pure argon, 40% CO_2 + 60% Ar and 20% CO_2 + 80% Ar shielding gas mixtures because of its separation from other lines and its strong maximum emission coefficient. The spectra of O I 777.3 nm line was chosen to measure arc plasma temperature of GMAW with pure carbon dioxide, 80% CO_2 + 20% Ar, and 60% CO_2 + 40% Ar shielding gas mixtures because of its separation from other lines and its strong maximum emission coefficient. During recorded arc plasma radiation, the continuum spectrum is simultaneously observed in addition to the argon atoms and oxygen atoms line spectrum. Consequently, in order to remove the effect of continuum spectrum, the radiation intensity at wavelength 694.0 nm was recorded simultaneously and subtracted from the 696.5 nm of the argon wavelength. Furthermore, the radiation intensity at wavelength 780.0 nm was also recorded simultaneously and subtracted from the 777.3 nm of the oxygen wavelength.

In order to determine Fe plasma properties, The Fe I 537.1 nm and 538.3 nm lines were selected since the maximum emission coefficient. The details of the spectroscopic parameters of each spectral lines were given in Table 2.1.

Table 2.1 Spectroscopic data used for diagnostics [58].

λ (nm)	Type	Configurations	Terms	E_n (eV)	g_n	A_{nm} (10^8 s^{-1})
777.31	O I	$2s^22p^33s$ - $2s^22p^33p$	$^5S^o$ - ^5P	10.7409	7	0.3690
696.54	Ar I	$3s^23p^54s$ - $3s^23p^54p$	$^2[3/2]^o$ - $^2[1/2]$	13.3278	3	0.0639
537.14	Fe I	$3d^74s$ - $3d^64s4p$	a^3F - z^5D^o	3.2657	5	0.0105
538.33	Fe I	$3d^74p$ - $3d^74b$	z^5G^o - e^5H	6.6149	13	0.0781

2.7 Fowler-Milne method for arc plasma temperature measurement

The arc temperatures were determined by using the Fowler–Milne method, which is also known as the normal temperature method. This method does not require absolute intensity calibration and the knowledge of atomic transition probabilities, thus precise values of temperature can be derived from reconstructed radial emission coefficients. The only restriction is that the plasma investigated should be in local thermodynamic equilibrium and the radial distribution of the emission coefficients should have an off-axis maximum. The Fowler-Milne method is based on the relationship between the line spectrum intensity I_{nm} and the temperature of arc plasma. The line spectrum intensity I_{nm} is given by

$$I_{nm} = \frac{A_{nm}hc}{4\pi\lambda_{nm}} \cdot \frac{g_n N_n exp(-E_n/kT)}{Z(T)} \tag{2.9}$$

where A_{nm} is the transition probability from upper level n to lower level m, h is the Planck's constant (J.s), c is the speed of light in vacuum (m.s^{-1}), λ_{nm} is the wavelength of the radiation emitted, N_n is the number density (m^{-3}) of upper level n [59 – 61], g_n is the statistical weight of upper level n, E_n is the energy of upper level n (eV), k is the Boltzmann's constant (J.K^{-1}), T is the temperature (K), and $Z(T)$ is the partition function. Equation 2.9 shows that the line spectrum intensity depends on the arc plasma temperature. Therefore, the plasma temperature can be inversely calculated by measuring the line spectrum intensity and convert using Equation 2.9. Fowler-Milne method relies on the facts that, for a plasma in LTE and at a constant pressure. The line spectrum intensity I_{nm} has a maximum at the well–defined temperature T_c known as the normal temperature. Figure 2.10 shows the calculated normalised intensity as a function of temperature of Ar I 696.5 nm and O I 777.3 nm lines.

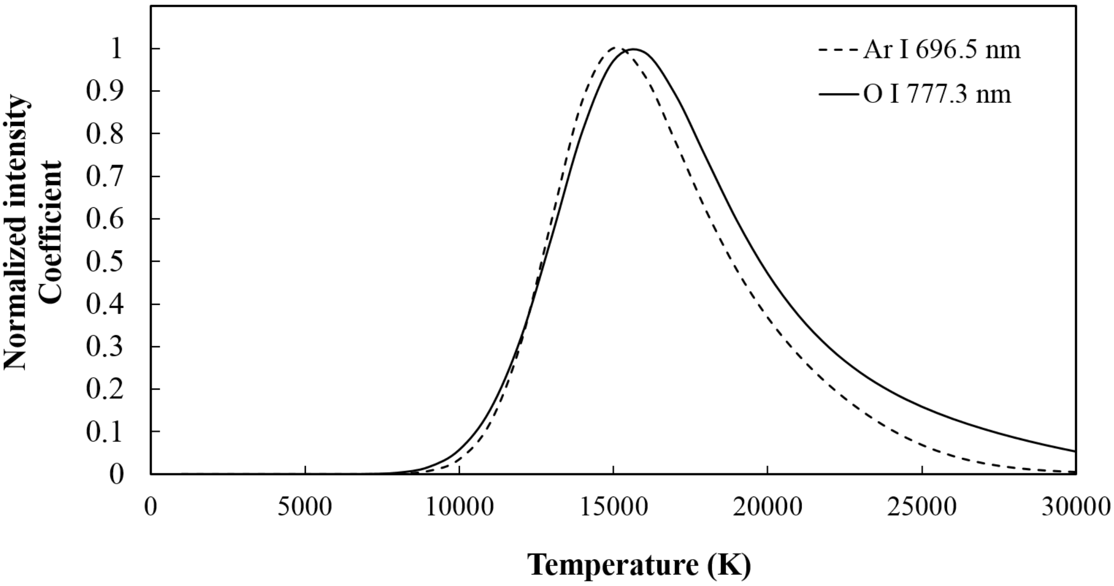

Figure 2.10 Calculated normalized intensity as a function of temperature of Ar I 696.5 nm and O I 777.3 nm lines.

The temperature dependence of the intensity coefficient of an Ar I 696.5 nm line of argon shielding gas and an O I 777.3 nm line for carbon dioxide. The emission coefficients are calculated from Equation 2.9 at different ratios, and normalized to their respective maximum values in pure argon arc. Since the normal temperature of Ar I 696.5 nm line is 15,000 K for GMAW arc with pure argon shielding gas and the normal temperature of O I 777.3 nm line is 15,600 K for GMAW arc with pure carbon dioxide shielding gas.

2.8 Two-line relative intensity method for Fe plasma temperature measurement

The two-line intensity correlation method is similar to the Fowler–Milne method. The only difference is the way to obtain emission coefficients**.** The two-line intensity correlation method also requires to measure the line intensities of two lines emitted by the same particles (atom or ion). Fe I 537.1 nm and Fe I 538.3 nm spectra were chosen for the two line intensity correlation method. The relative line intensity is described using the following equation.

$$\frac{I_{(1)}}{I_{(2)}} = \frac{A_{nm(1)} g_{n(1)} \lambda_{(2)}}{A_{nm(2)} g_{n(2)} \lambda_{(1)}} \exp\left\{-\left(\frac{E_{n(1)} - E_{n(2)}}{kT}\right)\right\} \tag{2.10}$$

The temperature can be calculated from the relative intensity using Equation 2.11 which is obtained by the deformation of Equation 2.10.

$$T = -\frac{E_{n(1)} - E_{n(2)}}{k} \cdot \frac{1}{ln\left(\frac{A_{nm(2)} g_{n(2)} \lambda_{(1)} I_{(1)}}{A_{nm(1)} g_{n(1)} \lambda_{(2)} I_{(2)}}\right)} \tag{2.11}$$

where *n* designates the upper and *m* the lower levels of the respective line, A_{nm} is the transition probability, g_n is the statistical weight of the upper levels, $\lambda_{(i)}$ are wavelengths of the line centers, $E_{n(i)}$ are energies of the upper levels of lines, k is Boltzmann constant, and T is temperature. Figure 2.11 shows the relationship between two iron line intensity ratios of Fe I 537.1 nm and Fe I 538.3 nm obtained from Equation 2.11

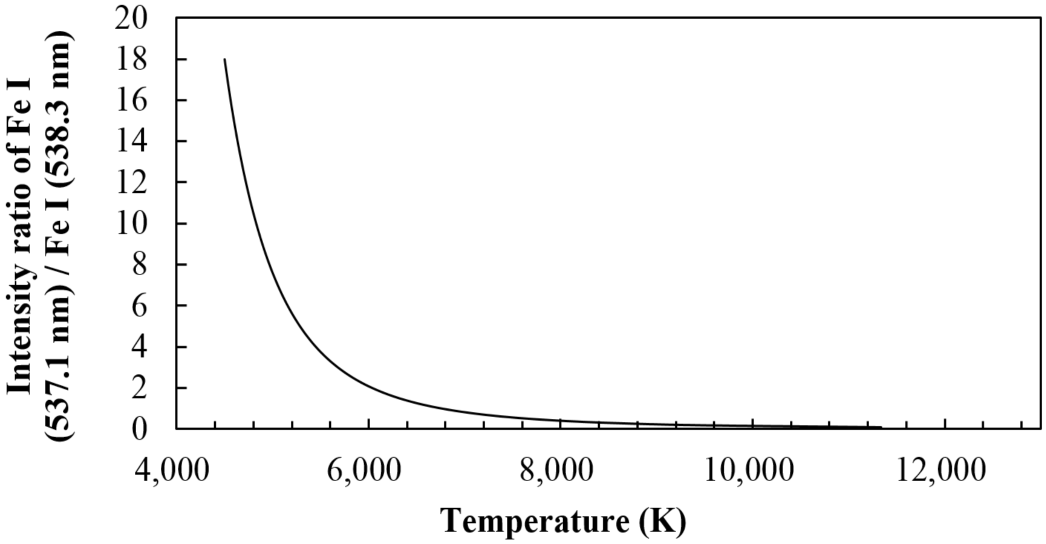

Figure 2.11 Relationship between line intensity ratio of Fe I 537.1 nm and Fe I 538.3 nm as a function of temperature.

2.9 Metal vapor concentration measurement

The Fe vapor concentration was obtained by the relationship between mole fractions, Fe atoms number density and temperature [25 - 27]. For calculation of the Fe vapor concentration, liner interpolation was used. The number density of Fe atoms was given by the following equation which is obtained by the deformation of Equation 2.9.

$$N_n = \frac{Z(T)}{A_{nm} g_n h v_n \, exp(-E_n/kT)} \cdot I_{nm} \tag{2.12}$$

where I_{nm} is intensity distribution of Fe line spectrum obtained from the experiment, N_n is the number density (m^{-3}), $Z(T)$ is the partition function. The Fe vapour concentration can be obtained using the relationship between Fe plasma temperature and the number density of Fe atoms of each Fe mole fraction [59 - 61]. Figure 2.12 shows the relationship between temperature and number density of Fe atoms for different Fe and CO_2 mole fractions. Also, Figure 2.13 shows the relationship between temperature and number density of Fe atoms for different Fe and Ar mole fractions. However, the intensity distribution obtained from the experimental measurement was corrected by the apparatus constant. The apparatus constant can be obtained by comparing the intensity distribution by Stark broadening technique [29, 48] with that obtained from the experimental measurement.

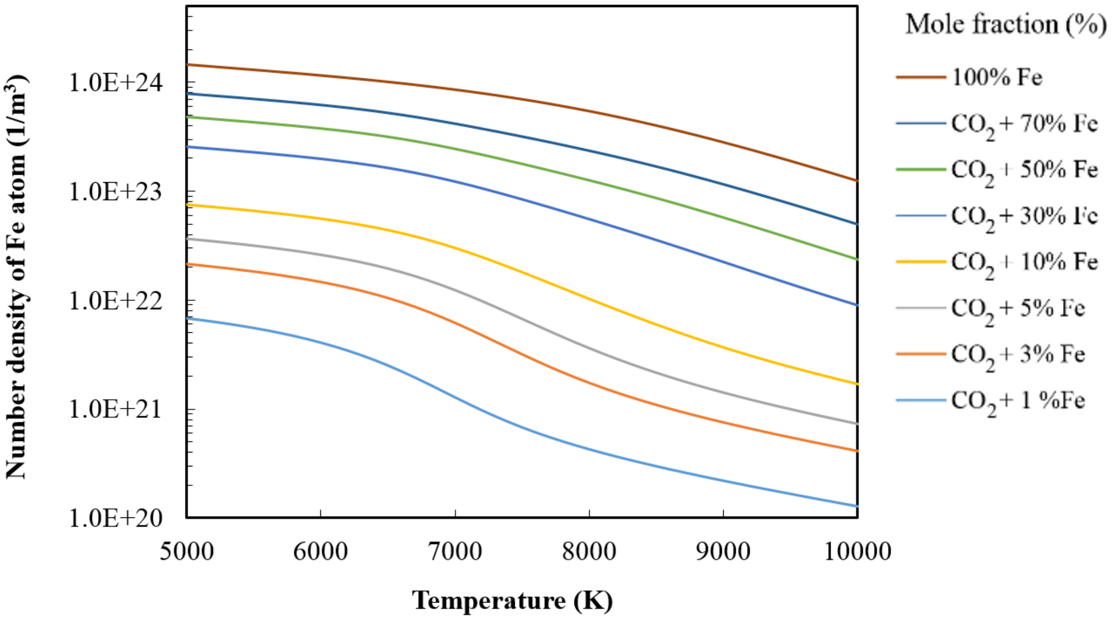

Figure 2.12 Relationship between temperature and number density of Fe atoms for different Fe and CO_2 mole fractions [59].

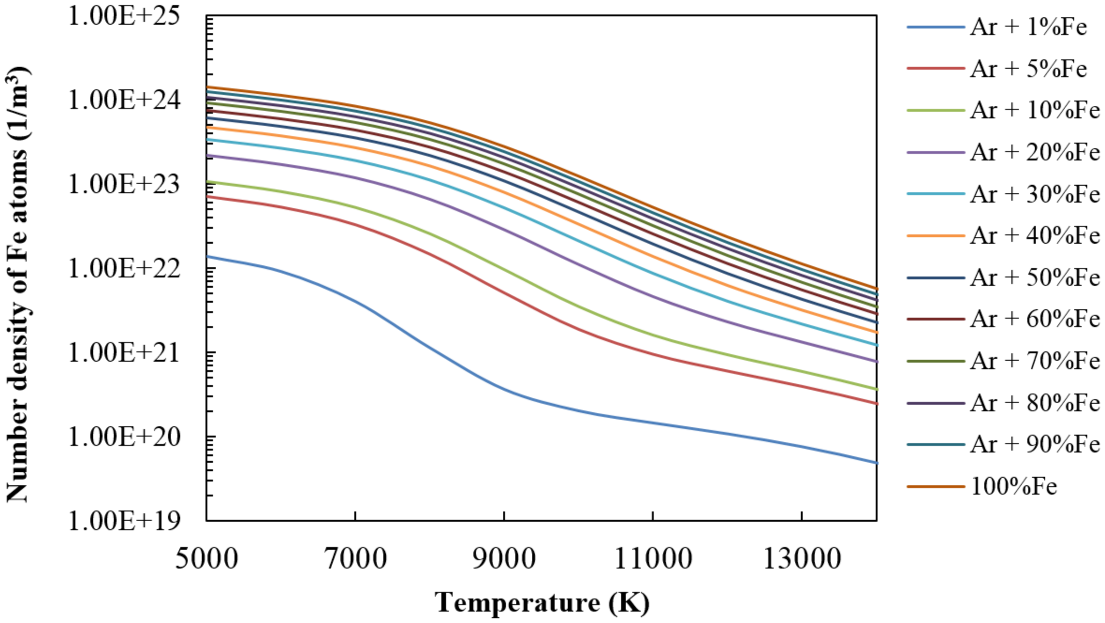

Figure 2.13 Relationship between temperature and number density of Fe atoms for different Fe and Ar mole fraction [56].

2.10 Two-color temperature method for metal droplet temperature measurement

In order to understand the plasma characteristic of GMAW and the effect of rare earth metal on droplet transfer mechanism. The metal droplet temperature has an important effect on the metal droplet phenomena. However it is difficult to measure the temperature of a droplet forming on the tip of the wire during welding and most often used in the past has been an indirect method in which droplets are gathered in a calorimeter and the heat content measured [62 - 64]. In this method, however, it is necessary to make an appropriate estimate of the heat lost by the droplet in the time between its detachment from the wire and its arrival in the calorimeter, and it cannot be described as a highly reliable method. Hirata et al. have experimentally used a direct temperature measurement method using two-color pyrometer [65]. However, the method was only used with Ar + 20% CO_2 shielding gas and the measurement wavelengths were 689.0 and 590.2 nm, in the visible light range, the measurements were timed for the short times when the arc was extinguished and thus were limited to measurement at a relatively low current range.

This research, high-speed color video camera was used to measure a metal droplet temperature using two-color temperature measurement algorithm (Thermera-HS, Nobby tech). The analysis on droplet temperature was done at the timing of an arc effect vanished completely. The color camera image consists of three images, which are in red (R), green (G) and blue (B). These three images are taken by different color sensors corresponds to a particular wavelength sensitivities. The sensitivities of these color sensors are 570 – 700 nm, 480 – 600 nm and 400 – 570 nm, subject to red, green and blue, respectively. Figure 2.14 indicates the spectral sensitivities of $Q_R(\lambda)$, $Q_G(\lambda)$ and$Q_B(\lambda)$ for red, green and blue sensors in the high-speed video color camera. Low pass and high pass filters were used to limit the spectral sensitivities range. Use of high speed video color camera enables all the radiation intensities ($I_{R^{meas}}$, $I_{B^{meas}}$ and$I_{B^{meas}}$) of each color to be measured simultaneously during experiment. By assuming the grey body radiation from the droplet surface, the theoretical intensity ratios $I_{R^{theo}}/I_{B^{theo}}$, $I_{G^{theo}}/I_{B^{theo}}$ and $I_{R^{theo}}/I_{G^{theo}}$ can be calculated as follows:

$$I_{R^{theo}}(T) = \sum_{\lambda=0}^{\infty} Q_R\,(\lambda)\varepsilon B(\lambda, T) \tag{2.13}$$

$$I_{G^{theo}}(T) = \sum_{\lambda=0}^{\infty} Q_G\,(\lambda)\varepsilon B(\lambda, T) \tag{2.14}$$

$$I_{B^{theo}}(T) = \sum_{\lambda=0}^{\infty} Q_B\,(\lambda)\varepsilon B(\lambda, T) \tag{2.15}$$

Where:

$$B(\lambda, T) = \frac{2hc^2}{\lambda^5} \cdot \frac{1}{e^{hc}/\lambda k_b T^{-1}} \tag{2.16}$$

Here, ε is the emissivity of the droplet, $B(\lambda, T)$ (Wsr^{-1}m^{-3}) is the black body radiation intensity, h is Planck constant, c is speed of light, k_b is Boltzmann constant and T is droplet surface temperature in kelvin.

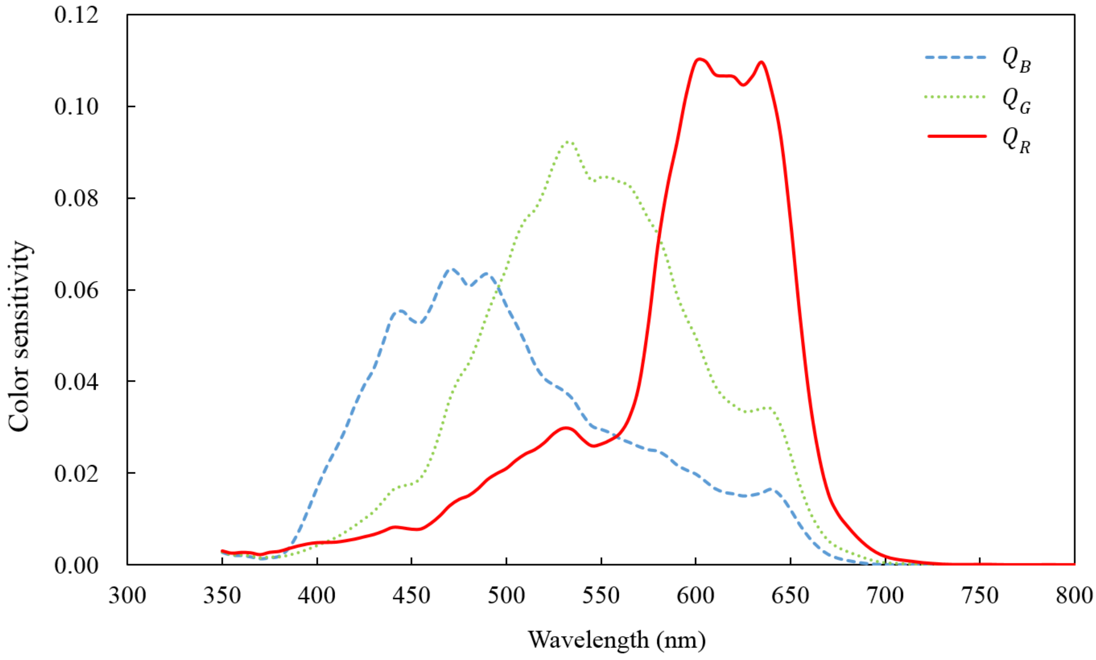

Figure 2.14 Spectral sensitivities of red, green and blue sensor in the high-speed video camera MIRO eX used in this research.

From equation (2.13), (2.14) and (2.15), the ratios of$I_{R^{theo}}/I_{B^{theo}}$, $I_{G^{theo}}/I_{B^{theo}}$ and $I_{R^{theo}}/I_{G^{theo}}$ only depend on T if ε is constant. Accordingly, temperature T on metal droplet surface can be determined by the value of the measured radiation intensity ratios $I_{R^{meas}}/I_{G^{meas}}$, $I_{G^{meas}}/I_{B^{meas}}$ and $I_{R^{meas}}/I_{G^{meas}}$ through the curve in Figure 2.15. Nevertheless, in this research, the intensity ratio of red to green ($I_{R^{meas}}/I_{G^{meas}}$) was used to measure the surface droplet temperature since the intensity of the blue color is observed to be very low. And also, in this experiment, ε is assumed to be the same because the difference in centre wavelength of red and green is small (approximately 50 nm). In order to assure an accuracy of the measurement, the sensitivities of the whole optical system were calibrated using a standard tungsten–halide lamp.

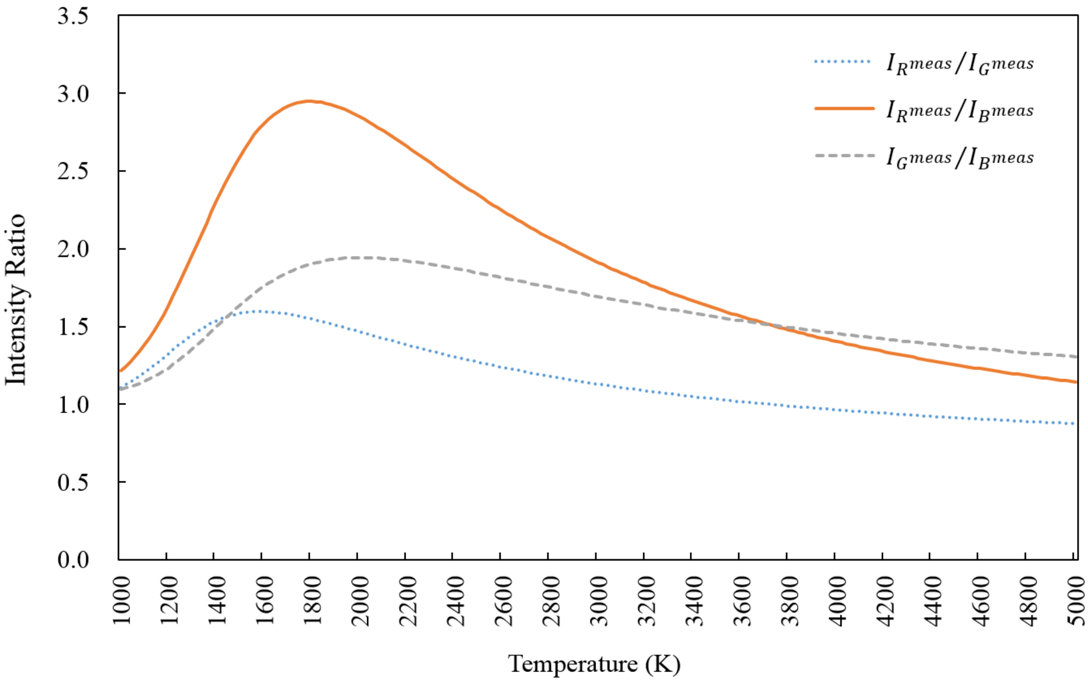

Figure 2.15 Calculated intensity ratio of red to green ($I_{R^{meas}}/I_{G^{meas}}$), red to blue ($I_{R^{meas}}/I_{B^{meas}}$), and green to blue ($I_{G^{meas}}/I_{B^{meas}}$) sensor as a function of temperature.

2.11 An evaluation of the accuracy of metal droplet temperature measurement

The accuracy of a metal droplet temperature measurement using Thermera-HS algorithm was evaluated over a range of metal droplet temperature in gas metal arc welding process. The measurement of tungsten electrode temperature was compared with the results from previous study. Haidar J. and Farmer A.J.D. [75] measured temperature profiles for various oxide-tungsten cathodes and for pure tungsten using a two-wavelength pyrometer technique. From Haidar J. and Farmer A.J.D. experiments, cathode surface temperature measurements for the tungsten-based with 2% by mass oxide-tungsten, La_2O_3-W are shown in Figure 2.16. These measurement was made for arcs operated with an arc currents of 200 A, a gas flow of 5 LPM of pure argon shielding gas, an arc length of 5 mm and cathode of 3.2 mm diameter initially shaped to a cone with 60º vertex angle. In order to evaluation an accuracy of metal droplet temperature measurement using Thermera-HS algorithm, the measurement of temperature profiles for 2% by mass oxide-tungsten, La_2O_3-W with the same experimental condition with Haidar J. and Farmer A.J.D. was compared. The cathode surface temperatures are similar to the measurements presented in this thesis. The maximum cathode surface temperature measured by Thermera-HS algorithm was around 3,360 K at the tip of cathode surface and decreasing to about 2,500 K at 2 mm axial distance from the cathode tip. The error of this experimental results compared with Haidar J. and Farmer A.J.D. was less than 5%.

Figure 2.17 shows a cathode temperature distribution for 2% La_2O_3-W measured by Thermera-HS algorithm. The cathode color image in Figure 2.17 (a) was captured immediately after an arc is extinguished to eliminate the effect of arc plasma during welding operation. Figure 2.17 (b) shows a cathode surface temperature distribution.

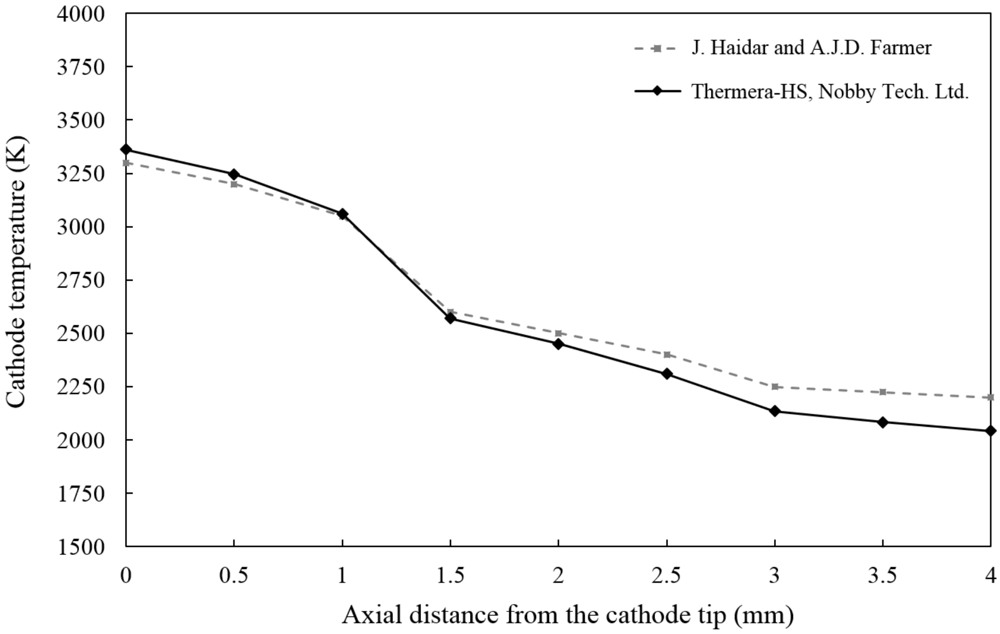

Figure 2.16 Surface temperature profile for 2% La_2O_2 cathode for two different measurement method.

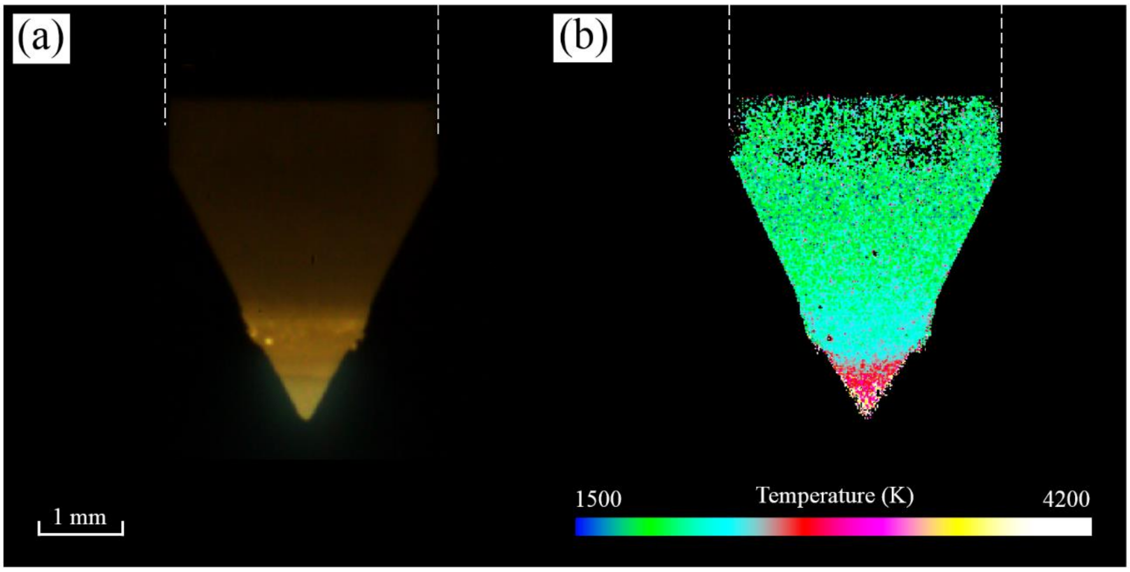

Figure 2.17 High speed color image of 2% La_2O_2 cathode immediately after the arc is: (a) High speed color image (b) two-dimensional distribution of cathode surface temperature

Chapter 3

Experimental set-up

This chapter presents the setup, procedure for the experiments used in this research. The overall goal of these experiments is to measure the plasma characteristics and droplet transfer phenomena during different welding conditions and modes of metal transfers. Two different types of wire electrode (conventional wire electrode and rare earth metal added wire electrode) used to compare thermophysical properties metal transfer behaviors. The basic GMAW welding principles were given in Chapter 1. These principles remain the same in the present configuration. The experimental set-up has capable to investigate arc plasma by emission spectroscopic techniques. Also high-speed camera system allowed counting droplet frequency and observed GMAW arc appearance.

3.1 Experimental setup for emission spectroscopic system

The optical measurement system has a capable of capturing four intensity images at the same time during welding. Figures 3.1 showed a schematic illustration of the optical system and the experimental set-up. It consists of three main sections, including the arc plasma source, the optical system, monochromator and high-speed camera system. These components are described in later paragraphs.

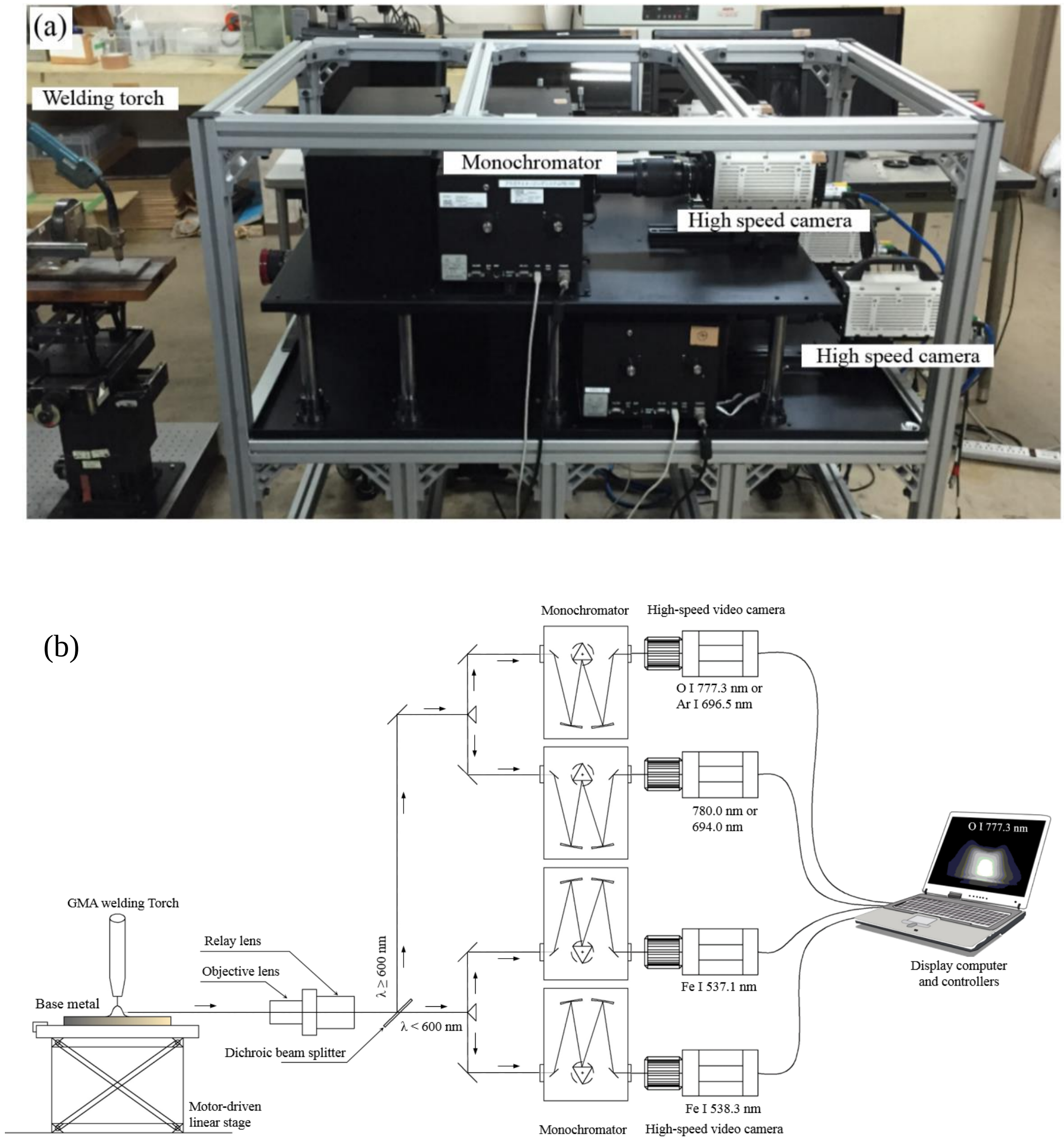

Figure 3.1 Schematic illustration of the (a) optical system and monochromator set-up and (b) schematic diagram of the experimental set-up

3.1.1 The arc plasma source

The main components of any GMAW welding system are the power source, the wire feed unit, and the welding torch. The arc plasma source used in this research includes all of these basic components in addition to sub-systems that allow precise measurement and control of welding variables. This section explains each component, how it works, and its importance to the overall system.

The GMAW power source

The power source used in this research is an OTC DAIHEN DM-350 [49] machine. It is a commercially available system that used in an industry. This function is capable for maintain superior weld integrity via uniform penetration throughout the weld. Power supply technology has come a long way since the advent of computers and the advanced outputs of these machines are capable of completely changing operating characteristics. The output signal for the present configuration is direct current - constant voltage. No pulsing welding current or waveform programming is implemented in the experiments.

Wire feeding unit

The model of wire feeding unit used in this research is a CM-7401 [50]. The maximum wire feed speeds is 22 m/mim. This wire feeding unit communicates directly with the power supply for precise process control. No modifications are made to the wire feeding unit that would change its output characteristics and process control of the system.

Welding torch and contact tips

The welding torch used in the research is a DAIHEN type WTCX-3503 U4167 [51]. This torch is water cooled and rate up to 500 A with rated duty cycle of 70%. The welding torch head is fixed in position to control the contact tip to work distance. The material to be welded is moved past the torch with constant travel speed. The contact tips used in this research is a standard commercially part from DAIHEN with diameter of 1.2 mm.

Shielding gas control

The shielding gas regulator is necessary to monitor the flow of shielding gas to the welding bead. The gas regulator for carbon dioxide and carbon dioxide -reached shielding gas used in the research is a Crown FCR-2501: carbon dioxide gas regulator with a heater. The pressure regulator is designed for connection to a compressed gas cylinder, whose pressure is 25 MPa or less. The carbon dioxide heater is designed to prevent carbon dioxide gas regulator freeze-up and prevent porosity in weld beads from loss of shielding gas. Furthermore, the gas regulator for Ar and Ar-reached shielding gas used in the research is Crown FR-IS-P: Ar gas regulator.

Motor-driven linear stage

The motor-driven linear stage used in this research is ROBO Cylinder RCS2-SA7C-I-60-4-300-T2-S [52]. It is a commercially available stage that used in an industry. This linear motor stage combines a rugged bearing and drive design with precision positioning capabilities for single and multi-axis applications requiring travels up to 800 mm. The aluminum stage base and carriage are designed to be very stiff, yet lightweight structures. Incorporated into the stage are matched linear guides capable of speeds up to 200 mm/s. The linear brushless servomotor provides non-contact linear drive forces allowing rapid rates of move and settle. The positioning repeatability of this stage is ± 0.02 mm. All of these functions are capable for maintaining precise welding travel speed.

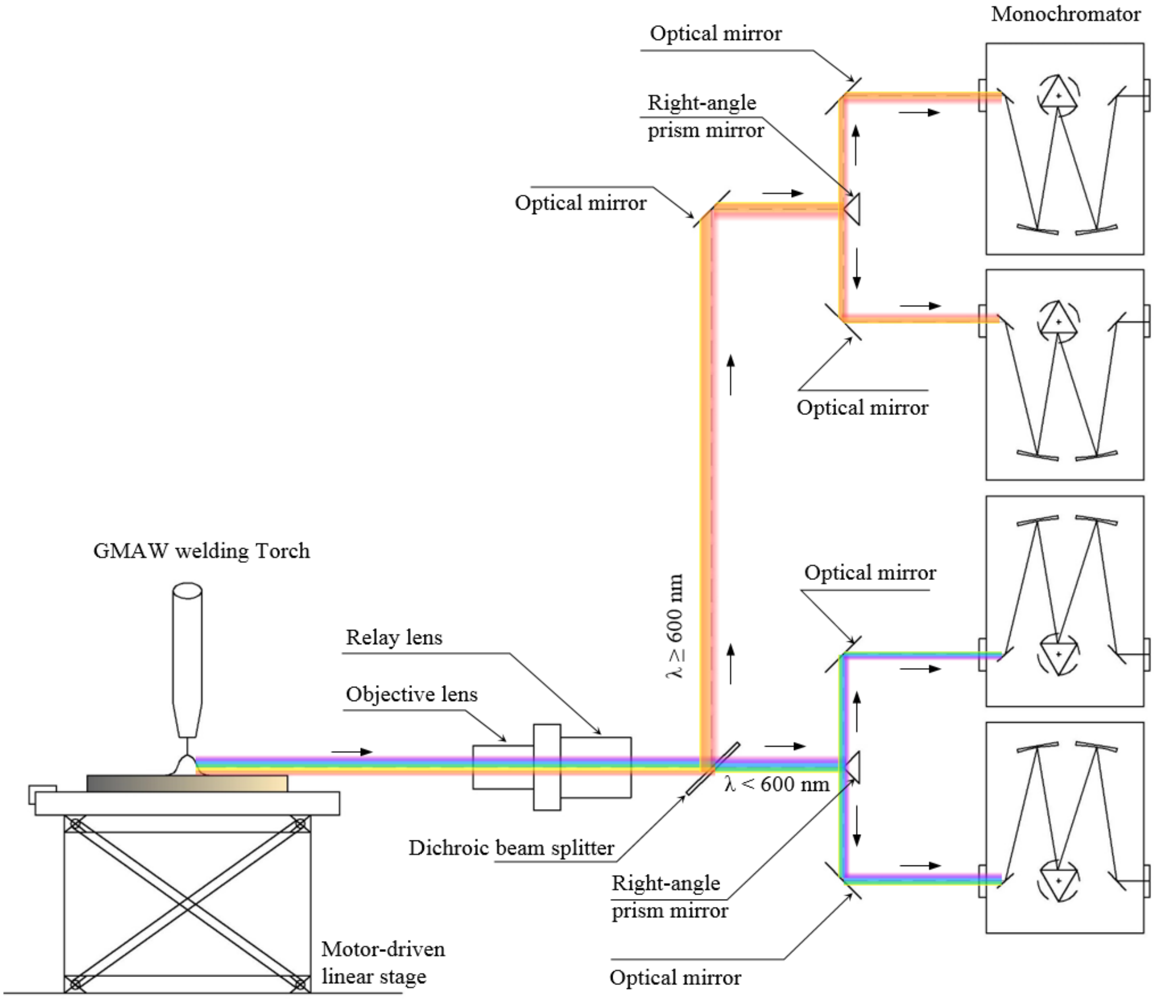

Figure 3.2 Schematic illustration of lens and mirror system.

3.1.2 Lens and mirror system

The lens and mirror system used in this research is designed for reflect and separate arc plasma radiation to four pathways of light with the same intensity. All four pathways of light was focused on to 0.5 mm entrance slit of monochromator. Figure 3.2 showed a schematic illustration of the lens and mirror system. The major components of a lens and mirror system are:

Objective lens

Objective lens in the emission spectroscopic system is the lens that is closest to the arc plasma being magnified. The main function of objective lens is to focus an arc plasma image from GMAW. The objective lens used in this research is Micro-NIKKOR 55mm 1:3.5. This lens is suitable for getting GMAW arc image with good focus and proper image size. The distance between objective lens and GMAW torch are 550 mm and 750 mm for GMAW arc with carbon dioxide shielding gas and for GMAW arc with Ar shielding gas.

Relay lens

The main function of the relay lens is to inverts an image and extends the length of optical system. Relay lens used in this research is Micro-NIKKOR 105 mm 1:2.8. This relay lens placed behind the objective lens. Both set of lens are connected by special designed fixture.

Dichroic beam splitter

Dichroic beam splitter is an optical device that splits a beam of light in two. Figure 3.3 (a) showed schematic of beam splitter used in this research. The dichroic beam splitter used in this research is Edmund, TECHSPEC 600 nm dichroic shortpass Filter, 25.2 x 35.6 mm. This dichroic beam splitter allows light with wavelength upper 600 nm are reflected and light wavelength lower and equal 600 nm are transmitted with angle of incidence 45º.

Optical Mirror

The optical mirror is an optical device that designed to reflect light for a variety of applications. The optical mirror used in this research is Edmund, TECHSPEC first surface mirrors, 50.0 x 50.0 mm. The coated surface is to be facing the in incident light in order to minimize energy loss by not allowing light to pass through the glass substrate. The main purposes of the optical mirror in this research was to reflect the arc light emission to the entrance slit of monochromator.

Knife-edge right-angle prism mirror

Right-angle prisms mirror is typically used to reflect image light paths on to two legs and offer a clear aperture extending across the 90º angle between the coated surfaces. The precise knife-edge corner between the two coated surfaces allows two counter propagating beams to be made collinear with the output orthogonal to the input light. Figure 3.3 (b) showed schematic illustration of Beam splitter used in this research. The right-angle prisms mirror used in this research is THORLABS, Knife-Edge Right-Angle Prism Mirrors 25 x 25 mm reflective surfaces. The main purposes of the optical mirror in this research were to split and reflect the arc light emission from dichroic beam splitter and optical mirror into left and right path.

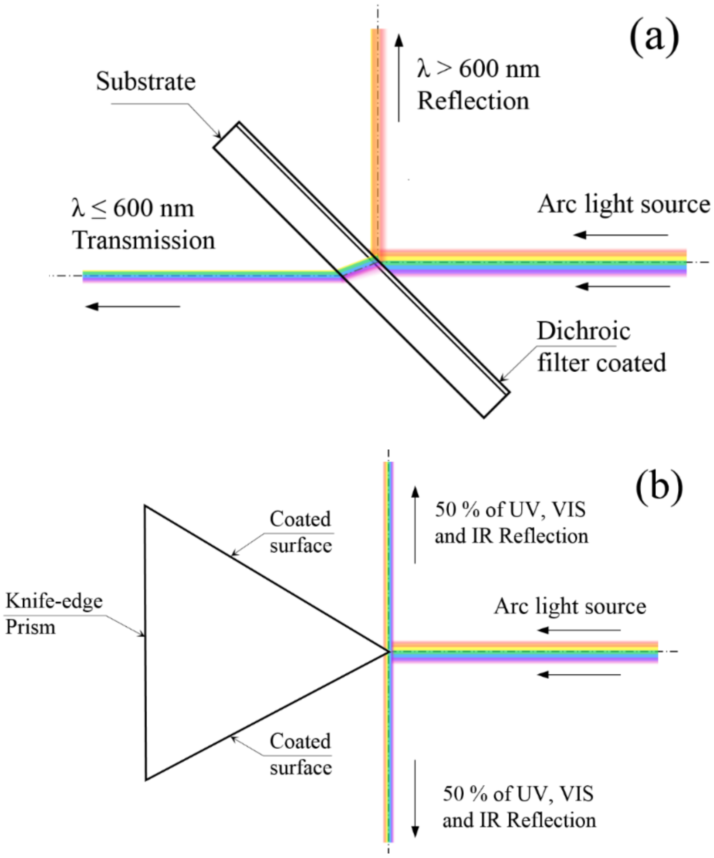

Figure 3.3 Schematic illustration of (a) a dichroic beam splitter with 600 nm shortpass filter and (b) knife-edge right-angle prism mirror

3.1.3 Monochromator [53]

Monochromator is an optical device that transmits a mechanically selectable narrow band of wavelengths of light or other radiation chosen from a broadband (multi-wavelength) source. In spectrometers, this can be used to collect light from an atomic emission source, like the atomic emission detector, and allow only a specific line to exit. The monochromator used in this research is called a Czerny-Turner monochromator, Princeton Instruments, Acton SpectraPro SP-2300 with a focal length of 300 mm, triple grating. Figure 3.4 showed schematic illustration of Czerny-Turner monochromator used in this study. The major components of a monochromator are as follows:

Entrance and Exit slits

The purpose of the two slits in this monochromator is to control the size and "position" of the beam of light passing through the slit. On the way in, the entrance slit makes sure that only a small area of the input beam passes into the monochromator and that the light waves are relatively parallel coming from the source. Since the light will be carefully allowed to shine amount the mirrors and grating inside the monochromator, parallel beams insure alignment of the light beams with the internal optics and cut down on stray light that might end up where it's not wanted. The edges of the slit are very carefully machined so that the distance between the two edges through which the light passes are equidistant all along the slit opening. The entrance slit and exit slit were adjusted at 0.5 mm.

Collimating mirror and focusing mirror

Once light enters from the entrance slit, it is redirected by collimating mirror toward the grating. After light is dispersed by the grating it is captured by focusing mirror and redirected towards the exit slit. The surface of these mirrors must be reflective in the wavelength region of the light involved.

Diffraction grating

The dispersion element in this monochromator is a grating. Its job is to take parallel light incoming from the entrance slit, light that contains multiple different wavelengths included ultraviolet ray, visible light, infrared ray and to disperse the wavelengths in space such that they are no longer parallel but instead leave the grating at slightly different angles, angles dependent upon the wavelength. Since light passes off the grating at angles dependent upon its wavelength, it will also reflect off the mirror at different angles. So that means that at the second mirror the individual wavelengths are some distance apart and after reflecting of flat mirror, the beams diverge even further. When they arrive at the exit slit they are so substantially separated in space that they fall like a rainbow across the plane of the exit slit. The diffraction grating used in this study is 68.0 x 68.0 mm grating with 1,200 grooves per millimeter.

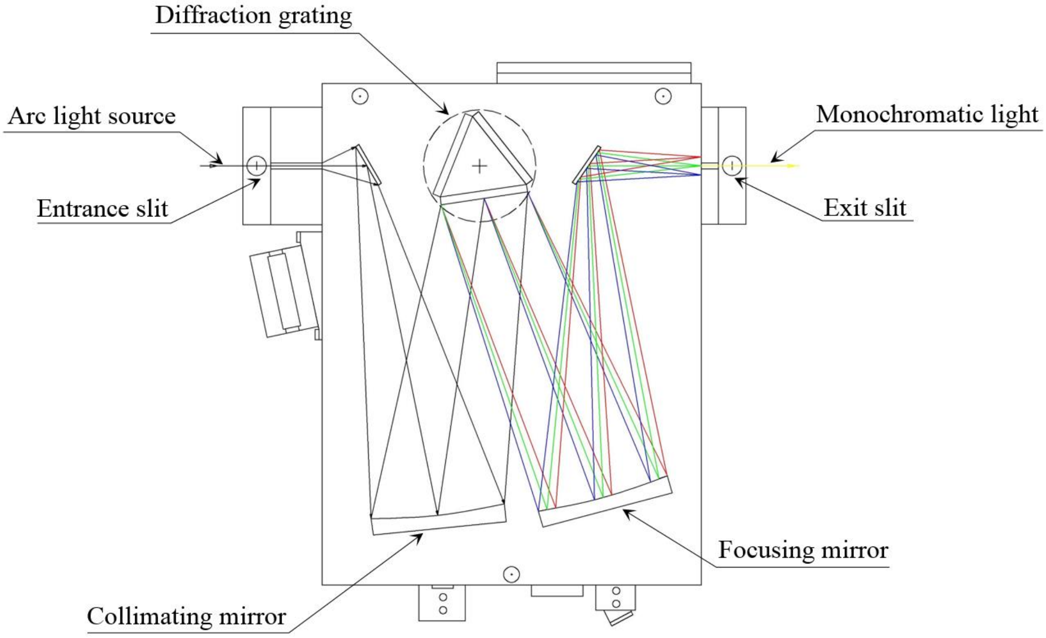

Figure 3.4 Schematic illustration of the Czerny-Turner monochromator.

3.1.4 High-speed video camera

A high-speed camera is a device capable of capturing moving. It used for recording fast-moving objects as photographic images onto a storage medium. The main purposes of a high-speed camera was to capture the spectrum lines (also called monochromatic light). High-speed cameras used in this research is NAC’s Memrecam GX-1. This high-speed camera can provides superior light sensitivity, Mega pixel resolution and high frame rates all in one camera. The maximum framerate is 200,000 fps [54].

Monochromators and high-speed cameras used in this study were consist of four systems allowed to capture the arc plasma radiation with difference line spectrum. The cameras were placed at the back of each monochromator. All high-speed cameras were simultaneously recording line spectrum of arc images at the same time in order to compare and analyzed the experimental results at the same time and same place during welding.

3.2 Experimental setup for the observation of metal transfer behaviors

The observation of metal transfer behaviors system has a capable of capturing molten droplet transfer during GMAW. Figure 3.5 showed a schematic illustration of the experimental setup for the observation of metal transfer behaviors. It consists of the arc plasma source, objective lens and high-speed camera system.

The same arc plasma source in the emission spectroscopic system is used in the observation of metal transfer behaviors experiment. Nikon 200 mm f/4 AF Micro-NIKKOR was used as an objective lens, this lens has the extra-long 200 mm focal length which has a capable to capture the metal droplet transfer with high magnification at suitable focus. The objective lens was placed in front of high-speed camera. The high-speed camera used in this experiment is MIRO eX, Vision Research, Phantom, New Jersey, USA. These camera settings allowed counting droplet frequency and droplet diameter.

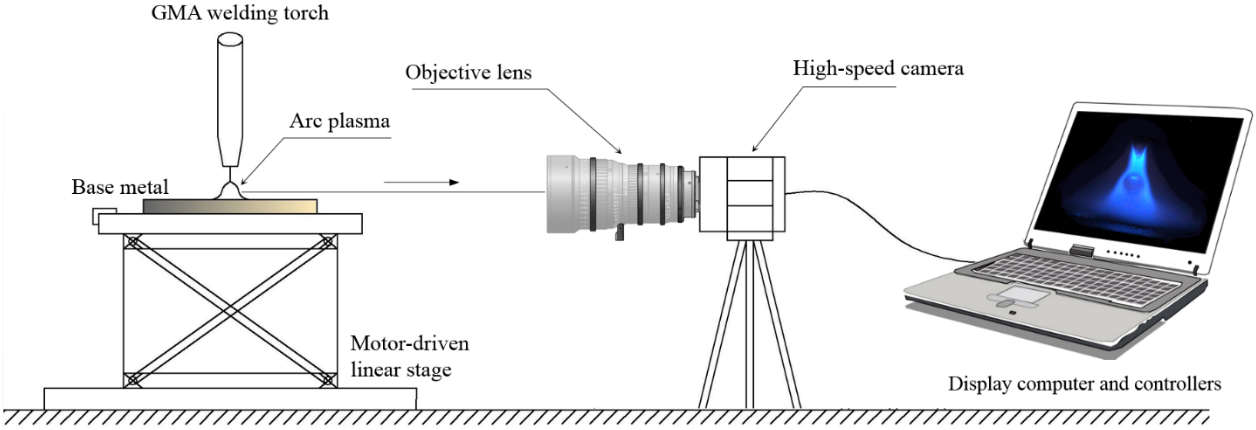

Figure 3.5 Schematic diagram of the experimental setup for the observation of metal transfer behaviors.

3.3 Material and consumables

3.3.1 Base metal

This research, GMAW was performed on carbon steel base metal JIS G 3101 SS400 with thickness of 10 mm and 300 mm long. The materials were selected due to their wide application and also to provide more knowledge on their welding input and output performance. The surface condition of these materials is a smooth surface (Ra values between 0.1 and 0.5 pm). These materials are the most popular for different engineering applications in industry, such as automotive, simple structural components, jigs, fixtures, pharmaceutical equipment, chemical vessels, vacuum vessels, power plant etc [55]. Details of the chemical composition SS400 were given in Table 3.1 and the mechanical properties of JIS G 3101 SS400 were given in Table 3.2.

Table 3.1 The chemical composition of JIS G 3101 SS400 [55]

Material specification	Chemical Composition (%)						
	C	Mn	Cu	Si	P	S	Fe
SS400	0.26-0.29	1.03	0.20	0.28	≤ 0.04	≤ 0.05	98.0

Table 3.2 The mechanical properties of JIS G 3101 SS400 [55].

Material specification	Tensile strength, Ultimate	Tensile strength, Yield	Elongation at Break (in 50 mm)	Modulus of Elasticity
SS400	400 - 550 MPa	250 MPa	23.0 %	200 GPa

3.3.2 Welding wire electrode

GMAW was carried out using with two types of carbon steel wire electrodes. The wire electrodes used in this research are as follow:

JIS Z 3312 YGW11 MG-50 [56] is a kind of gas shielded copper-plated welding wire electrode for low alloy steel, and CO_2 shielding gas or Ar-reached gas shielding gas can be used for protection. Because the titanium element is added into welding wires, crystal grains of fused metal are thinned, the excellent comprehensive mechanical property is obtained, and the welding wires are more suitable for high welding current high-efficiency welding. YGW11 MG-50 wire electrode is suitable for use in a wide variety of applications in the welding of shipbuilding and structural steel. The equivalent specification of YGW11 MG-50 are ASME / AWS A5.18 ER70S-G. The wire diameter of YGW11 MG-50 used in this research was 1.2 mm and the chemical composition was given in Table 3.3.

JIS Z 3312 YGW11 KC-500 [57] is a carbon steel wire electrode which was developed by JFE Steel Corporation, Japan and the so-called J-STAR (JFE Spray Transfer Arc). The characteristics of this wire electrode were high arc stability and low spatter with pure carbon dioxide shielding gas. Normally, GMAW arc using conventional carbon steel wire electrode with pure carbon dioxide shielding gas were produced high amount of spatter. By adding rare earth metal (REM) elements as arc stabilizing, YGW11 KC-500 wire electrode can reduce the amount of spatter generated during arc at high welding current above 250 A, DCEN with pure carbon dioxide shielding gas. YGW11 KC-500 wire electrode demonstrated better arc stability, smooth metal transfer and smaller droplet size comparing with wire diameter [57]. This phenomenon can be classified as a spray transfer mode. The wire diameter of YGW11 KC-500 used in this research was 1.2 mm and the chemical composition was given in Table 3.3.

Table 3.3 Chemical composition of wire electrode.

Composition (wire mass %)	C	Si	Mn	P	S	Ti	Others
JIS Z3312 YGW11 MG-50 [56]	0.04	0.73	1.58	0.01	0.01	0.22	-
JIS Z3312 YGW11 KC-500 [57]	0.05	0.70	1.60	0.01	0.01	0.20	REM

3.4 Welding parameters

The welding parameters used as variables in this study include welding current, welding arc voltage, shielding gas, wire electrode specification and travel speed. The welding parameters and the combination welding parameters used in this research are shown in Table 3.4. All the welding was performed as bead-on-plate welding and the plates were prepared such that there is no mill scale on the surface and also clean the surface by wire brush or electronic grinder.

Table 3.4 Welding parameters and the combination welding parameters

Electrode specification	Electrode polarity	Shielding gas compositions	Welding Current (A)	Wire feed Speed (m/min)	Welding arc voltage (V)	Travel speed (m/min)	CTWD (mm)	Shielding gas Flow rate (L min^{-1})
YGW11 MG-50	DCEP	Pure CO_2	300	13.2	33.0	0.6	20	20
	DCEP	Pure Ar	300	8.2	35.7	0.6	25	20
	DCEP	20% CO_2 + 80% Ar	270	11.3	29.0	0.45	20	20
	DCEP	20% CO_2 + 80% Ar	290	12.5	32.5	0.45	20	20
	DCEP	20% CO_2 + 80% Ar	300	10.8	33.5	0.6	20	20
	DCEP	20% CO_2 + 80% Ar	310	13.9	35.5	0.6	20	20
	DCEP	20% CO_2 + 80% Ar	330	14.2	36.0	0.6	20	20
	DCEP	20% CO_2 + 80% Ar	350	15.0	37.0	0.6	20	20
	DCEP	20% CO_2 + 80% Ar	370	16.5	38.5	0.6	20	20
	DCEP	40% CO_2 + 60% Ar	300	10.5	35.3	0.6	20	20
	DCEP	60% CO_2 + 40% Ar	300	10.5	33.5	0.6	20	20
	DCEP	80% CO_2 + 20% Ar	300	10.5	33.5	0.6	20	20
YGW11 KC-500	DCEN	Pure CO_2	300	13.1	33.0	0.6	20	20
	DCEN	Pure Ar	300	13.5	36.0	0.6	25	20
	DCEN	20% CO_2 + 80% Ar	300	13.5	33.5	0.6	20	20
	DCEN	40% CO_2 + 60% Ar	300	13.5	33.5	0.6	20	20
	DCEN	60% CO_2 + 40% Ar	300	13.5	33.5	0.6	20	20
	DCEN	80% CO_2 + 20% Ar	300	13.5	33.5	0.6	20	20
	DCEP	Pure CO_2	300	13.5	33.0	0.6	20	20

Chapter 4

Experimental results

4.1 Plasma characteristics of GMAW using pure carbon dioxide shielding gas

In this section, two representative characteristics as a heat source, which are the plasma temperature and metal vapor concentration are investigated by optical emission spectroscopy techniques. Moreover, the temperatures of metal droplets are measured by two-color temperature measurement technique. In order to obtain the radial profile of line intensity using Abel inversion, the axisymmetric arc plasma is required. Nevertheless, the GMAW arc plasma of pure carbon dioxide, 80% CO_2 + 20% Ar, 60% CO_2 + 40% Ar, 40% CO_2 + 60% Ar and 20% CO_2 + 80% Ar shielding gas were difficult to preformed axisymmetric arc plasma as shown in appendix A and B. In order to check this, preliminary measurements are made with two cameras simultaneously recording the arc image and placed along two perpendicular directions. Results show that the symmetry is quite good at the time before droplet detachment. For this reason, only line intensity images of arc plasma before droplet detachment were selected.

4.1.1 Intensity distribution of GMAW with pure carbon dioxide shielding gas

Figure 4.1 shows the spectral images of O I 777.3 nm line and Fe I 538.3 nm line. Yellow dotted lines show the outline of the electrode. These images were taken during welding with 300 A. The results show that both of O I and Fe I are distributed in the arc column at the same time. This indicates that the carbon dioxide plasma and Fe plasma mix with each other. This fact is different from the arc plasma using 100% Ar welding with a current of above 250 A [76] in which the arc plasma has a dual structure consisting of Ar plasma region apart from the arc axis and Fe-reached region near the arc axis as shown in Figure 4.2.

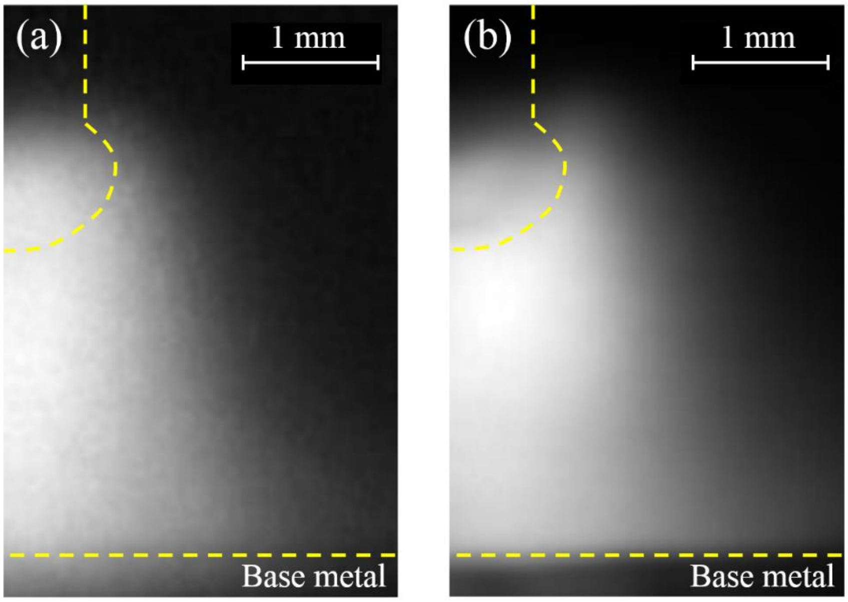

Figure 4.1 Line spectral images of (a) O I at 777.3 nm and (b) Fe I at 538.3 nm at the welding current of 300 A with DCEP polarity.

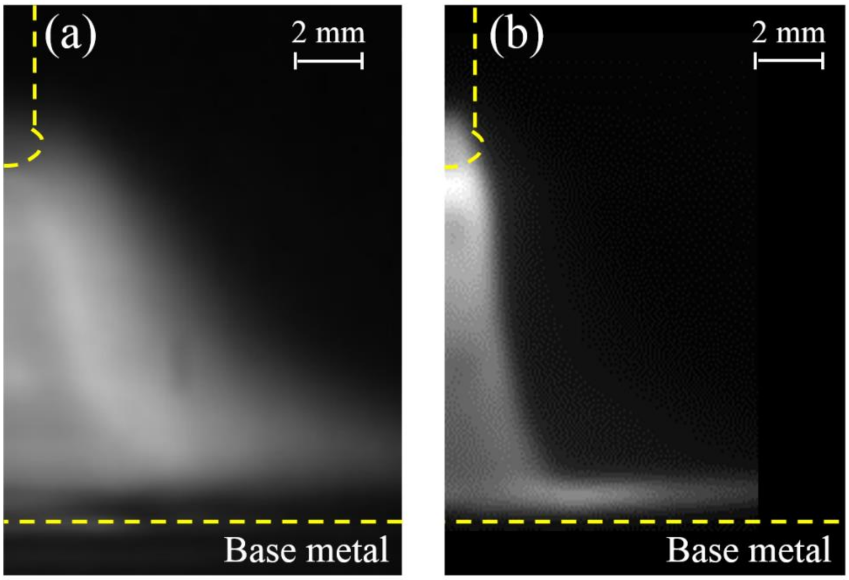

Figure 4.2 Line spectral images of (a) Ar I at 696.5 nm and (b) Fe I at 538.3 nm at the welding current of 270 A with DCEP polarity [76].

4.1.2 Plasma temperature distribution and Fe vapor concentration

Figure 4.3 (a) shows an instantaneous distribution of Fe plasma temperature in 300 A with DCEP polarity using a MG-50 wire electrode. The temperature distribution shows the highest value over 8,000 K at the center of the arc column. However, the distribution widely spreads with a range from 7,000 to 7,500 K. Figure 4.3 (b) shows the concentration distribution of Fe vapor. The distribution shows the highest value over 60 % mole fraction near the tip of the wire. It can be explained that the constriction of arc plasma near the arc axis leads to the increase of joule heating and promotes the high vaporization of Fe at the near surface of wire electrode.

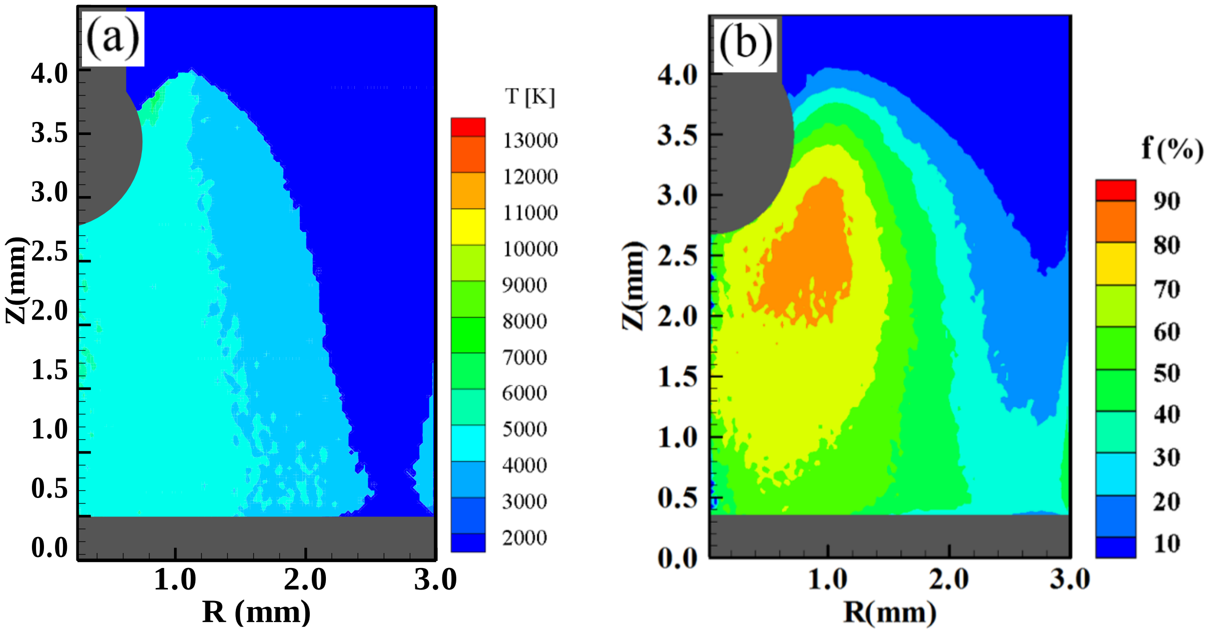

Figure 4.3 Instantaneous distribution of (a) plasma temperature and (b) concentration of Fe vapor at the welding current of 300 A with DCEP polarity.

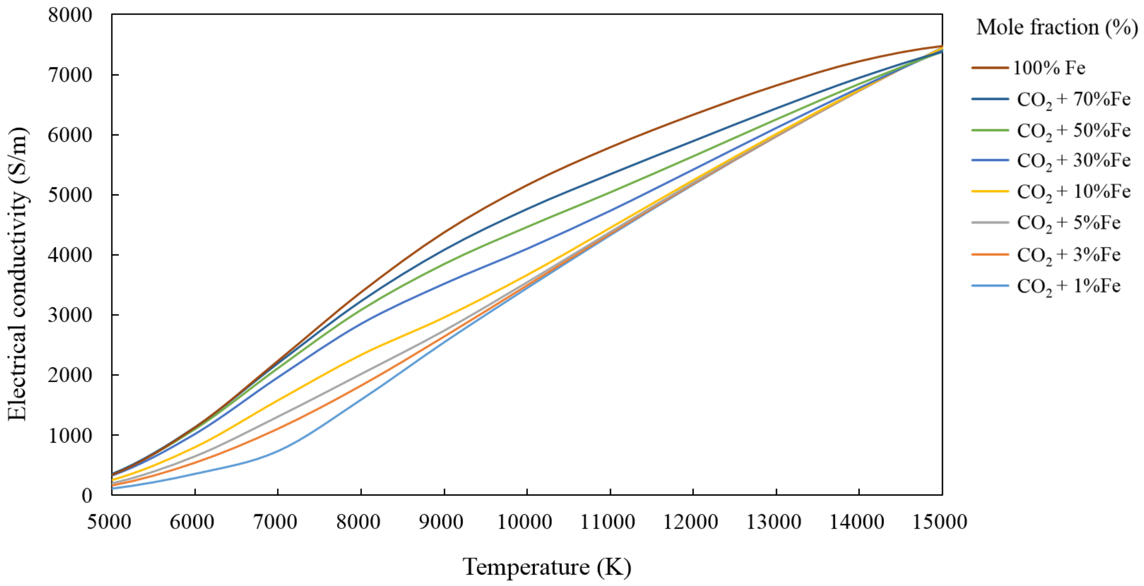

Figure 4.4 Relationships between temperature and electrical conductivity of Fe atoms for different Fe mole fraction [59]

4.1.3 Electrical conductivity distribution

The electrical conductivity distribution is one of the main characteristics which tells the pathway of electrical current. Figure 4.4 shows the relationships between temperature and electrical conductivity for different Fe mole fractions. Using these relations, the electrical conductivity distribution in GMAW can be obtained as shown in Figure 4.5. The result shows that the maximum electrical conductivity is located at the center of the arc column. It can be conjectured that the electrical current goes along the central axis of the arc column.

The current density concentrates on the bottom tip of the metal droplet. This means that the center of the arc column has higher Joule heating. The strong axial component of electromagnetic force can be accomplished by high current density at the bottom tip of the metal droplet. An increasing force in the lower part of the droplet which induces an upward movement of globule developed at the tip of the wire electrode [24].

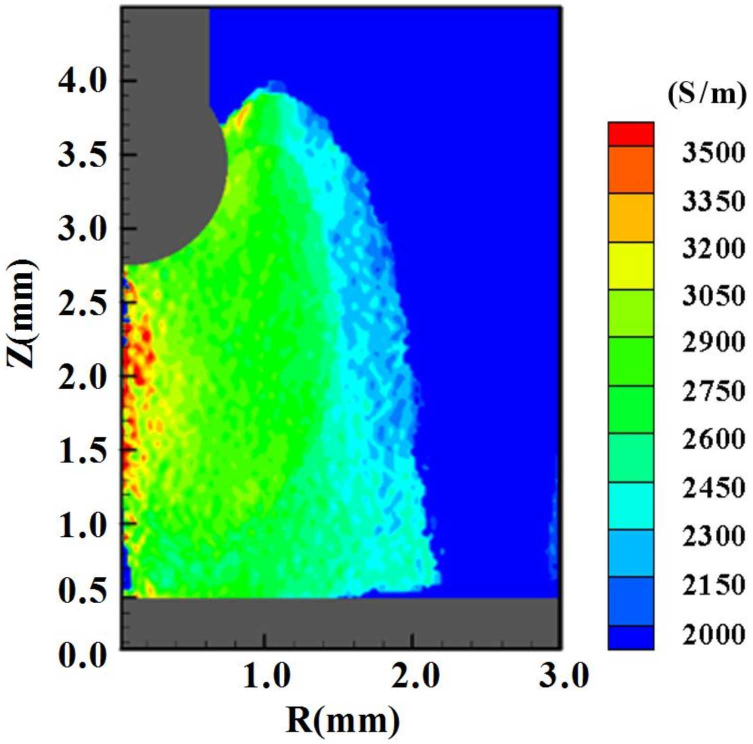

Figure 4.5 Instantaneous distribution of electrical conductivity at the welding current of 300 A with DCEP polarity.

4.2 Plasma characteristics of the globular to spray transition

In this section, experimental measurements of the plasma main parameters, plasma temperature distribution and metal vapor concentration, were presented. In order to understand the metal transfer mechanism and the globular to spray transition current, the optical emission spectroscopies using the Fowler-Milne method and two-lines relative intensity method were carried out for the GMAW with 80% Ar + 20% CO_2. The images of argon and Fe line spectra and arc appearances were obtained by high-speed camera system which can provide information of dynamic change of the plasma and electrodes. The spectroscopic data were converted to the arc plasma temperature and metal vapor concentration by data processing under the assumption of local thermodynamic equilibrium.

The high speed cameras (NAC, MEMRECAM GX-1) were used to capture the arc plasma radiation. The cameras were placed at the back of each monochromator. The 16-bit images were captured with the frame rate of 2,000 frames per second (fps) and the exposure time of 1,000 μs. These camera settings allowed recording plasma radiation at high temporal resolution. The optical emission spectroscopy system and monochromators were illustrated in Figure 3.1 in chapter 3. Moreover, colour images of arc plasma were captured by using high-speed digital colour camera (Phantom, Miro eX). These camera settings allowed counting droplet frequency and droplet diameter. The optical system for high-speed colour images and schematic diagram were presented in Figure 3.5 in chapter 3.

4.2.1 Arc appearance of GMAW with difference welding current

Figure 4.6 showed the colour images of the arc plasma and metal droplet transfer at the time after detachment of droplet. A white dashed line indicated the YGW 11 MG-50 wire electrode with 1.2 mm in diameter. The arc plasma images were captured from the direction which was perpendicular to travel direction. The metal droplets were formed at the tip of wire electrode and then detached to the weld pool. The metal droplet size decreased with increase of welding current. When the welding current was 270 A, the metal droplet was obviously larger than the dimeter of wire electrode. It meant that the metal droplet transfer mode was globular transfer. In contrast, the metal droplet was smaller than the diameter of the wire electrode. The transfer mode became spray transfer mode at the welding current of 350 A.

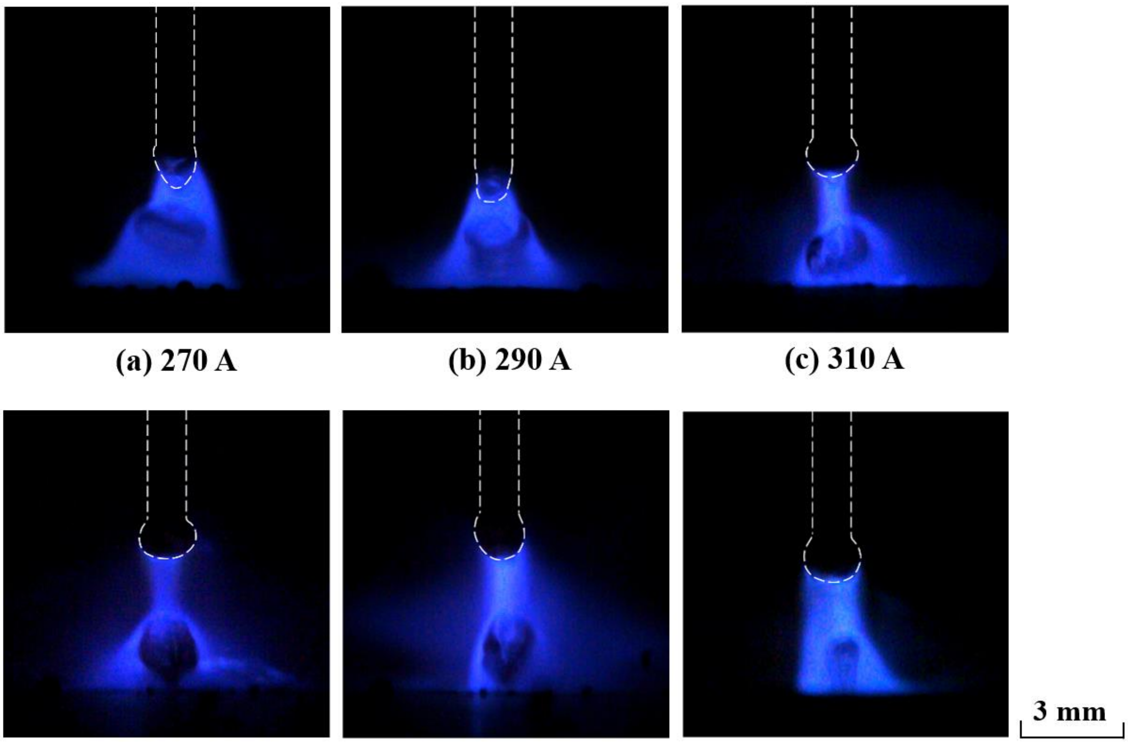

(a) 270 A (b) 290 A (c) 310 A

(d) 330 A (e) 350 A (f) 370 A

Figure 4.6 Arc appearance of GMAW of different welding currents using YGW 11 wire electrode in 80% Ar + 20% CO_2 shielding gas.

4.2.2 Effect of welding current on metal droplet diameter and detachment frequency

Figure 4.7 show the influence of welding current on droplet diameter and droplet frequency. The results showed that the droplet diameter decreased as the welding current increased and it was smaller than the diameter of wire electrode when the welding current was around 330 A. The globular to spray transition was observed at the welding current range of 330 – 350 A.

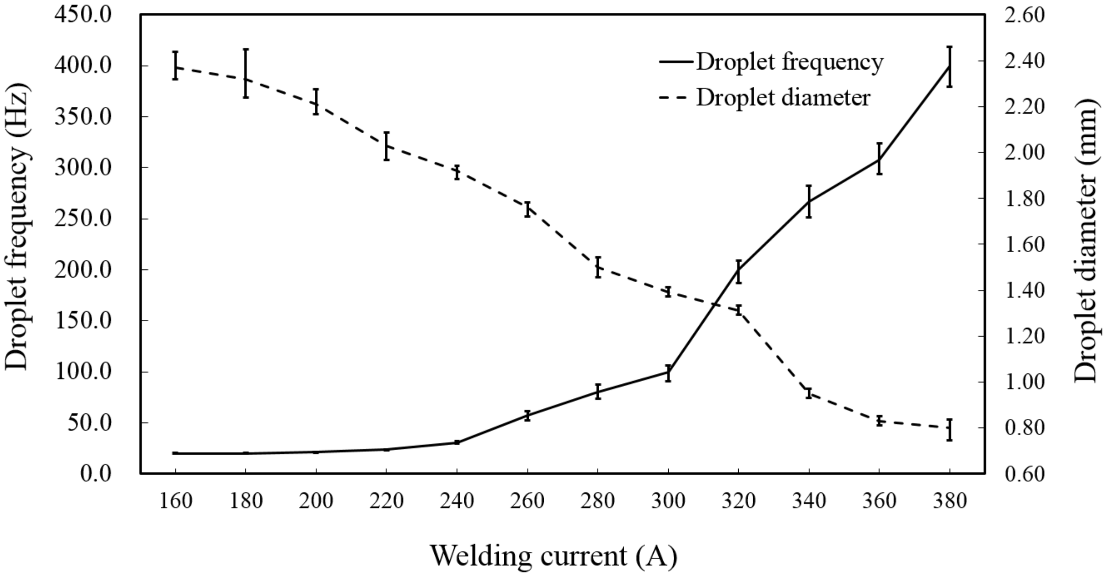

Figure 4.7 Influence of welding current on droplet diameter and droplet frequency using 1.2 mm YGW 11 wire electrode in 80% Ar + 20% CO_2 shielding gas.

4.2.3 Arc plasma temperature of GMAW with difference welding current

Figure 4.8 shows the temperature distribution profile with different welding current of the argon and carbon dioxide plasma. These temperatures were calculated from the Ar I 696.5 nm line using the Fowler-Milne method. The welding current seem to have a little influence on plasma temperature. The maximum temperature is about 11,000 K. It can be clearly identified that the profile shapes of temperature change depending on metal transfer mode. At the welding current of 310 A, the transfer mode was globular and the high temperature region still included the arc axis. However, the high temperature region moved away from the arc axis when the transfer mode changes from globular to spray transfer. It should be noted that the plasma temperature obtained from the Fowler-Milne method is valid only in high intensity distribution of Ar I line spectrum at the region apart from the arc axis.

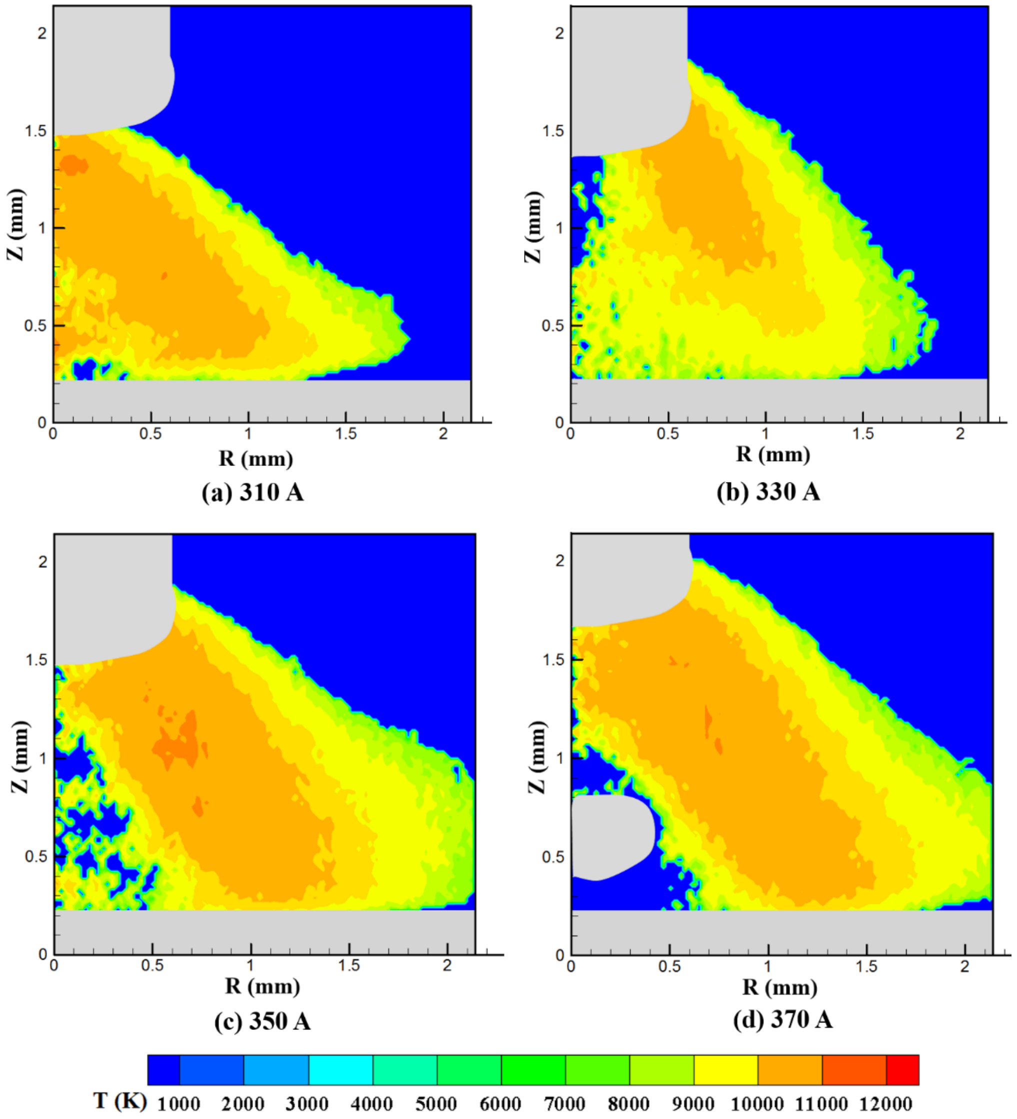

(a) 310 A

(b) 330 A

(c) 350 A

(d) 370 A

Figure 4.8 Instantaneous distribution of the arc plasma temperature in GMAW with different welding current.

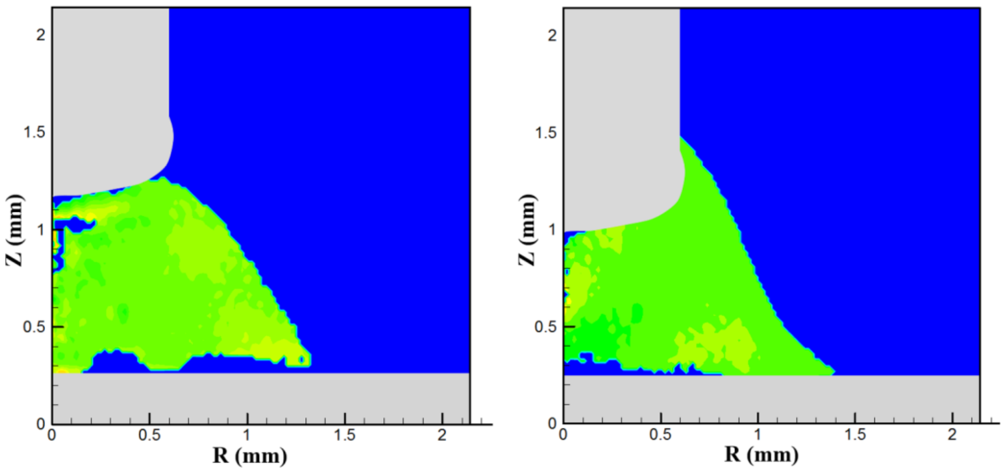

(a) 310 A (b) 330 A

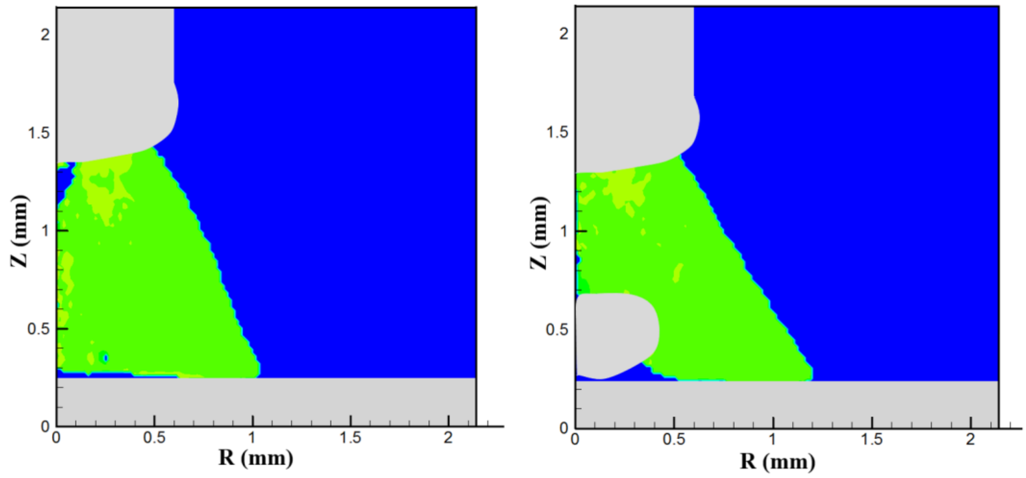

(c) 350 A (d) 370 A

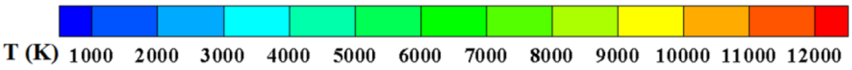

Figure 4.9 Instantaneous distribution of the Fe plasma temperature in GMAW with different welding current.

Figure 4.8 showed the temperature distribution profile with different welding current of Fe plasma. These temperatures were calculated from the iron lines intensity ratio of Fe I 537.1 nm and Fe I 538.3 nm using two-lines relative intensity method. It can be seen that the profile shapes of temperature changed little. In all welding currents ranging from 310 - 370 A, the uniform distribution of Fe plasma was found in the arc axis with the average temperature around 7,500 K. These results indicated that the temperature of Fe plasma was lower than that of argon and carbon dioxide plasma.

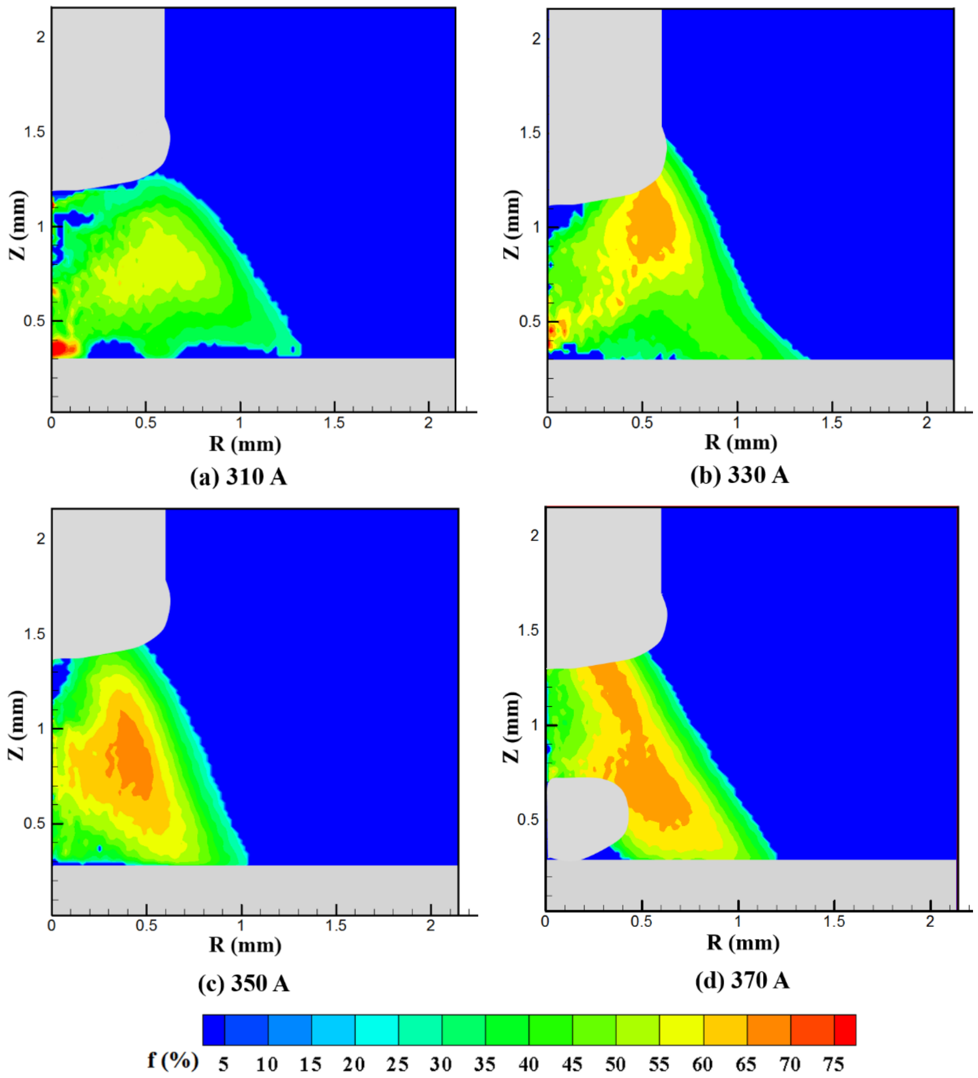

(a) 310 A

(b) 330 A

(c) 350 A

(d) 370 A

Figure 4.10 Instantaneous distribution of the Fe vapor concentration in GMAW with different welding current.

4.2.4 Behavior of metal vapor in plasma

Figure 4.10 showed the metal vapor concentration with different welding current and it was increased gradually with increasing welding current. It can be explained that the increase of the welding current leads to the increase of ohmic heating and promotes the vaporization of Fe at the surface of wire electrode.

It is well known that the presence of metal vapor decreases the plasma temperature by increasing the plasma radiation [25 – 29, 66]. That is the main factor for the temperature fall of central region observed in spray transfer mode. This means that the center of arc column in spray transfer mode had a high radiative emission coefficient and the temperature of arc become lower due to the radiative cooling.

4.3 Effect of rare earth metal on plasma characteristics of GMAW using pure carbon dioxide shielding gas

The mode of metal transfer depends on various welding parameters and has an important influence on welding quality. The most common transfer modes in GMAW are short-circuit, globular, and spray transfer. Direct current electrode positive (DCEP) polarity has the characteristics of deep penetration, very good arc stability, and the ability to operate in any of the metal transfer modes. Direct current electrode negative (DCEN) polarity has the characteristic of low penetration, higher wire melting rates for a given current, and low heat input, but has been largely limited to globular transfer. As a result of the globular transfer, DCEN polarity suffers from stability problems and therefore has had very limited use. These problems are easily solved by the addition of rare earth metal elements to the wire electrode.

In this section, the experimental measurements of the main plasma parameters of GMAW with REM-added wire electrode are presented. Arc plasma temperature, electron density, and metal vapor concentrations were obtained from oxygen and iron spectral lines. The spectroscopic data were compared with images obtained with a high-speed camera, which provided information on the temporal evolution of the plasma and electrodes. The line intensity determination allows obtaining the temperature by applying the optical emission spectroscopy method by assuming Local Thermodynamic Equilibrium (LTE).

The optical emission spectroscopy using the Fowler-Milne method and two-lines relative intensity method were carried out for the GMAW with pure carbon dioxide shielding gas. The welding was performed at direct current mode at a welding current of 300 A, an arc voltage of 33.5 V on carbon steel grade SS400, and travel speed of 60 cm/min. The two types of wire electrodes that were used in the experiment were JIS Z3312 YGW11 MG-50 and YGW11 KC-500 (JIS Z3312).

The spectra of O I 777.3 nm and 780.0 nm lines, which respectively presented the maximum emission and a background spectrum, are used to measure the plasma temperature by the Fowler-Milne method. The background spectrum was selected from arc light spectra of GMAW with pure carbon dioxide shielding gas.

The background spectrum was used for subtracting the continuum components in the spectra from discrete spectral lines. This technique improves the accuracy of measurements. The Fe I at 537.1 nm and 538.3 nm lines were used to measure the temperature of Fe plasma and Fe vapor concentration by the two-line relative intensity method. The images of oxygen, Fe line spectra and arc appearances were obtained by high-speed camera system which can provide information of dynamic change of the plasma and electrodes. The spectroscopic data were converted to the arc plasma temperature and metal vapor concentration by the data processing under the assumption of local thermodynamic equilibrium (LTE).

4.3.1 Arc appearance of GMAW with pure carbon dioxide shielding gas

Figure 4.11 shows dynamic two-dimensional arc color images from the high-speed camera of the GMAW arc plasma behavior under pure carbon dioxide shielding gas, welding current 300 A, and an arc voltage of 33.5 V.

When welding with the MG-50 wire electrode, as shown in Figure 4.11 (a) and 4.11 (b), large droplets formed at the tip of the electrode as in globular transfer mode. As shown in Figure 4.11 (b), the resulting arc was unstable and spatter was unacceptable. A major problem inherent to the use of DCEN polarity in GMAW is a strong repulsing force that acts on the molten end of the wire electrode as electrons are emitted from the cathode roots and transfer to the anode. These cathode roots and their high mobility are a result of many complex reactions within arc stream and at the cathode [67, 68]. An influence of a repulsive electromagnetic force of higher dissociation energy needed for carbon dioxide shielding gas has a great effect of the repelled metal droplet. In addition, these type of arc attachment are classified as spot mode with a highly constricted attachment on cathode [70]. In contrast, as shown in Figure 4.11 (a), more stable and less amount of spatter on the base metal surface was observed.

The images of arc plasma and droplet formation of the wire electrode with REM added (KC-500) were presented in Figure 4.11 (c) and 4.11 (d). The resulting of DCEP polarity, large droplets form at the tip of the electrode as same as MG-50 electrode. Thus, REM elements did not affect arc plasma and droplet formation in DCEP polarity. In contrast, the conical arc shape with small metal droplet diameter were presented in DCEN polarity as in shown Figure 4.11 (d). It can be clearly identified that the small metal droplets like in spray transfer is affected by REM added wire electrode with DCEN polarity. These changes could be caused by the lower the work function of the filler wire material and could thus make the emission of electrons more efficient and stabilize the cathode spot. It is also important to note that the arc attachment of KC-500 wire electrode are classified as diffuse mode over a large area of the cathode surface [70].

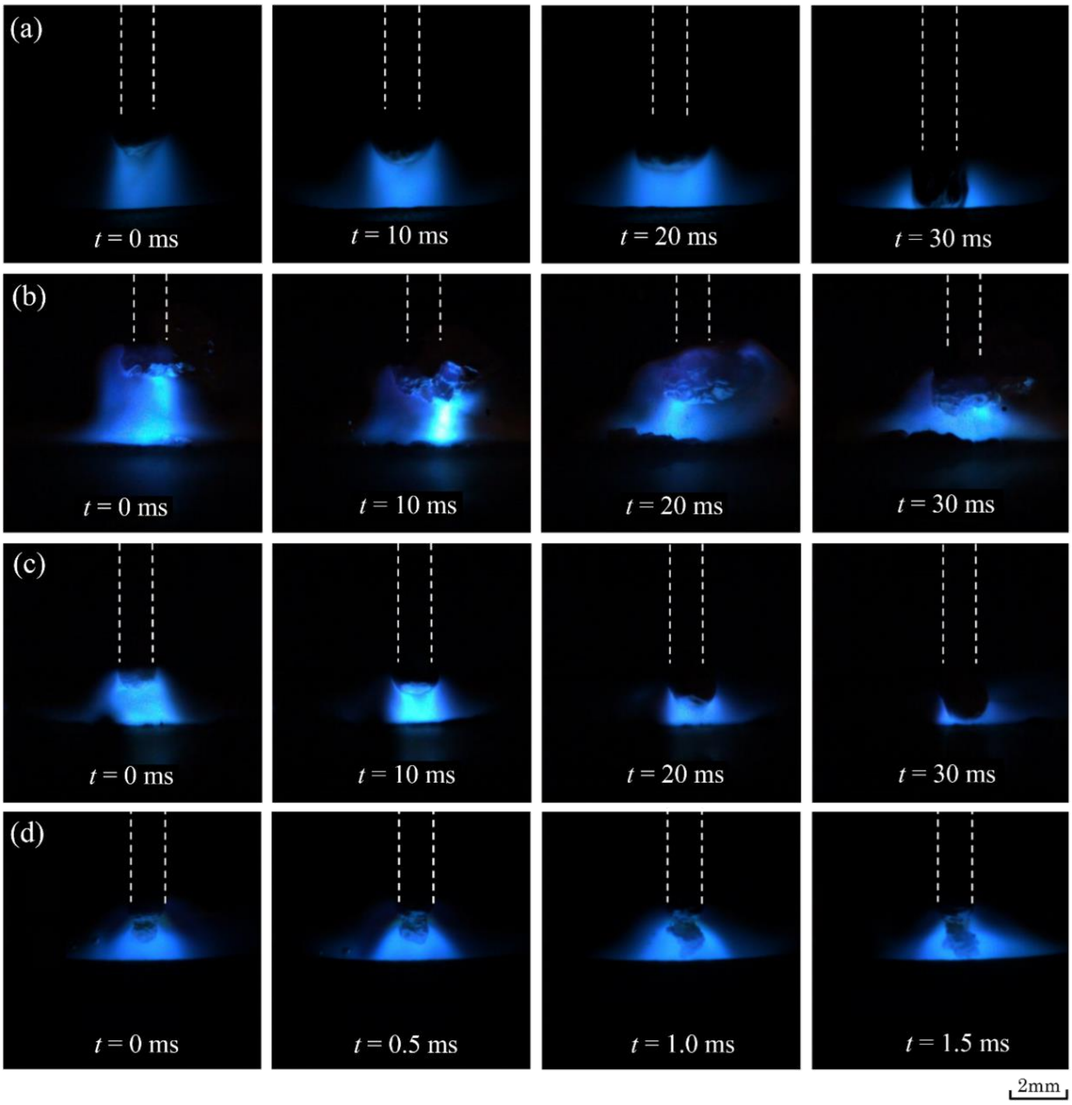

Figure 4.11 Arc appearance of GMAW of difference welding polarity and welding electrode (a) MG-50 wire electrode with DCEP; (b) MG-50 electrode with DCEN; (c) KC-500 wire electrode with DCEP; (d) KC-500 wire electrode with DCEN polarity.

For the high-speed color images presented in this study, it can be seen that the size of the droplet for the KC-500 wire electrode with DCEN polarity is much smaller than those of other conditions. The droplet diameter was smaller than the wire electrode observed in spray transfer mode.

4.3.2 Plasma properties of rare earth metal-added wire electrode with DCEN polarity

It can be clearly identified that the profile shapes of the line spectrum intensity image of O I at 777.3 nm in the left part of Figure 4.12 and Fe I at 538.3 nm in the left part of Figure 4.13 were separated into two regions. O I intensity image appeared at the region apart from the arc axis. On the other hand, Fe I intensity image appeared at the region near the arc axis. The right part of Figure 4.12 shows an instantaneous distribution of carbon dioxide plasma temperature. These temperatures were calculated from the O I 777.3 nm line using the Fowler-Milne method. The temperature distribution shows the highest value of over 13,500 K in a region apart from the arc axis. It should be noted that the plasma temperature obtained from the Fowler-Milne method is valid only in high intensity distribution of O I line spectrum at the region apart from the arc axis. However, as shown in the right part of Figure 4.13, an instantaneous distribution of Fe plasma temperature was lower than carbon dioxide plasma region. The temperature distribution of Fe plasma region was reached at around 7,250 – 7,500 K in a region of arc axis. Finally, it should be noted that the Fe plasma temperature obtained from the two-line relative intensity is valid only in high metal vapor concentration region near the arc axis.

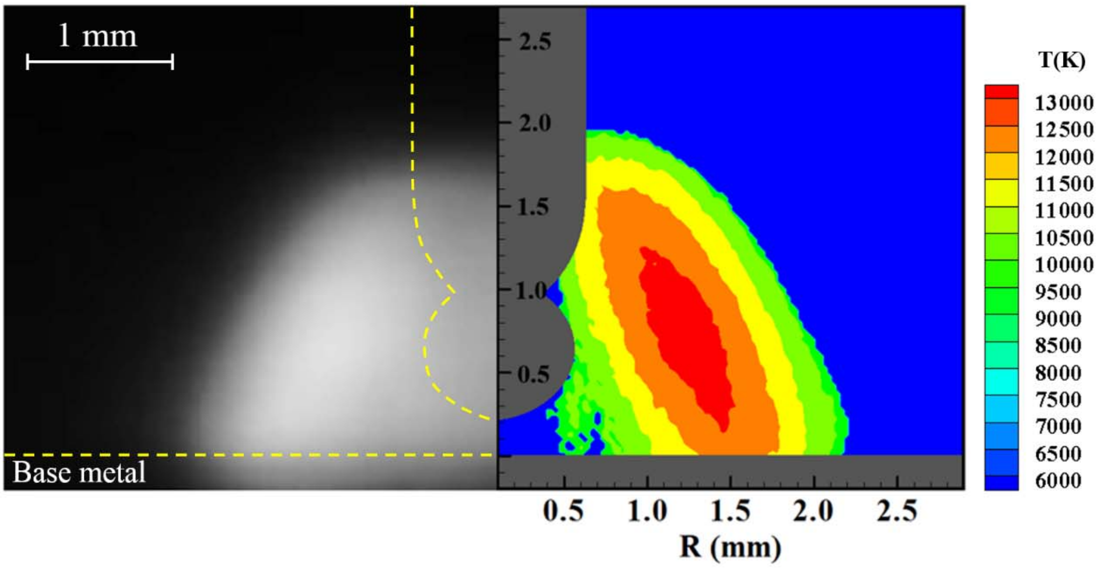

Figure 4.12 Line spectrum image of O I at 777.3 nm (left) and instantaneous distribution of carbon dioxide plasma temperature (right) at a welding current of 300 A arc with pure carbon dioxide shielding gas, KC-500 wire electrode, DCEN polarity.

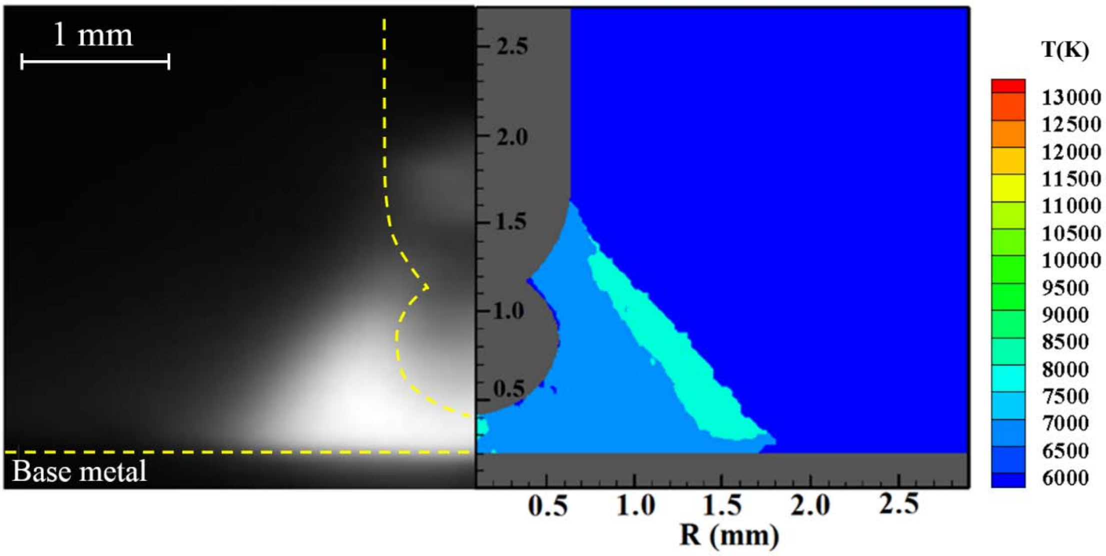

Figure 4.13 Line spectrum image of Fe I at 538.3 nm (left) and instantaneous distribution of Fe plasma temperature (right) at a welding current of 300 A arc with pure carbon dioxide shielding gas, KC-500 wire electrode, DCEN polarity.

Concentration distributions of Fe vapors are shown in Figure 4.14. The left part is the line spectrum intensity image of Fe I 538.3 nm. The right part is the concentration distribution of Fe vapor which was calculated by using relationship of Fe plasma temperature. The concentration of Fe vapor shows the highest value near the tip of the wire electrode.

The dominant effect of radiation can be explained by the relationship of plasma temperature and radiative emission coefficient for each mole fraction of Fe as shown in Figure 4.15. Similarly, the presence of metal vapor decreases the plasma temperature by increasing the plasma radiation [66]. This means that the center of the arc column in REM added wire electrode (KC-500) with DCEN mode shows a high radiative emission coefficient and the temperature of arc became lower from the effect of radiative cooling.

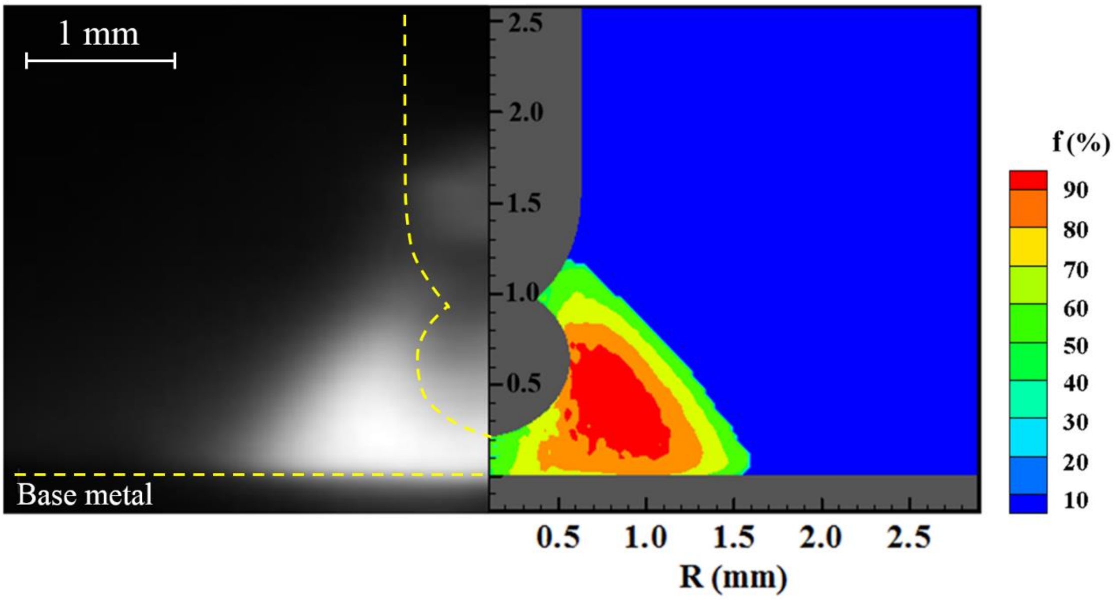

Figure 4.14 Line spectrum image of Fe I at 538.3 nm (left) and concentration of Fe vapor (right) at a welding current of 300 A arc with pure carbon dioxide shielding gas, KC-500 wire electrode, DCEN polarity.

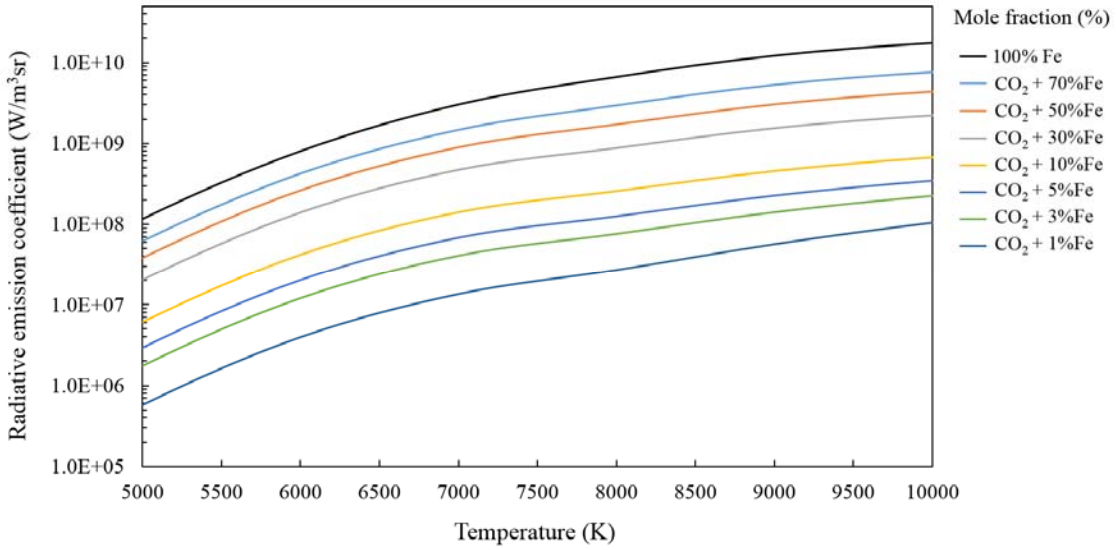

Figure 4.15 Relationships between plasma temperature and radiative emission coefficient for each Fe mole fraction [16].

The electrical conductivity distribution is one of the main characteristics which indicates the pathway of the electrical current. Figure 4.4 in section 4.1.2 shows the relationships between temperature and electrical conductivity for different Fe mole fractions [59]. Using these relationships, the electrical conductivity distribution in GMAW can be obtained as shown in Figure 4.16. The result shows that the maximum electrical conductivity is located at apart of arc axis. It can be conjectured that the electrical current goes through the arc at the region apart from the arc axis. It should be noted that the electrical conductivity of carbon dioxide plasma is valid only in high intensity distribution of O I line spectrum at the region apart from the arc axis, and also the electrical conductivity of Fe plasma is valid only in high metal vapor concentration region near the arc axis.

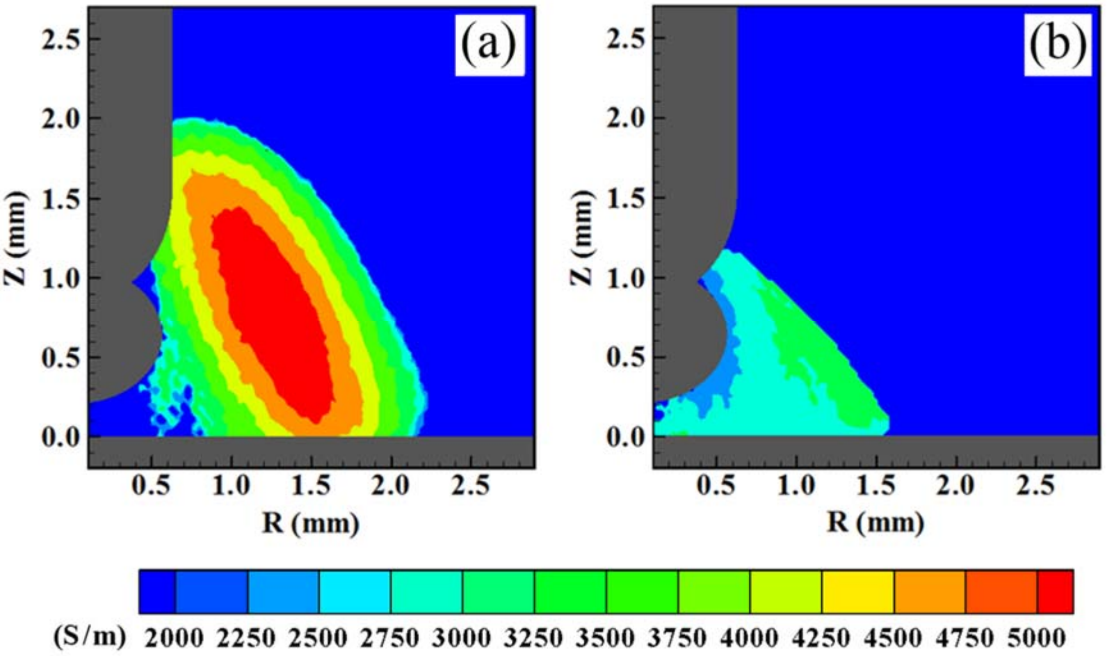

Figure 4.16 Distribution of the electrical conductivity (a) carbon dioxide plasma region and (b) Fe plasma region in 300 A arc with pure carbon dioxide shielding gas, KC-500 wire electrode, DCEN polarity.

4.3.3 Plasma properties of rare earth metal-added wire electrode and conventional wire electrode with DCEP polarity

Figure 4.17 (a) and (b) shows the spectral images of O I 777.3 nm line and Fe I 538.3 nm line using the MG-50 wire electrode. The white dotted line shows the outline of the wire electrode. These images were taken during welding with a current of 300 A. The results show that both O I and Fe I are distributed in the arc column at the same time which indicates that the carbon dioxide plasma and Fe plasma mix with each other. Similarly, for the KC-500 wire electrode, Figure 4.17 (c) and (d) show results of both O I and Fe I are distributed near center of arc column.

Figure 4.18 (a) and (b) shows an instantaneous distribution of plasma temperature for MG-50 and KC-500 wire electrode. The temperature distribution shows the highest value over 7,500 K in the region of arc axis. Consequently, the distribution of plasma temperature for MG-50 and KC-500 wire electrode with DCEP polarity was different from the distribution of plasma temperature for KC-500 with DCEN polarity.

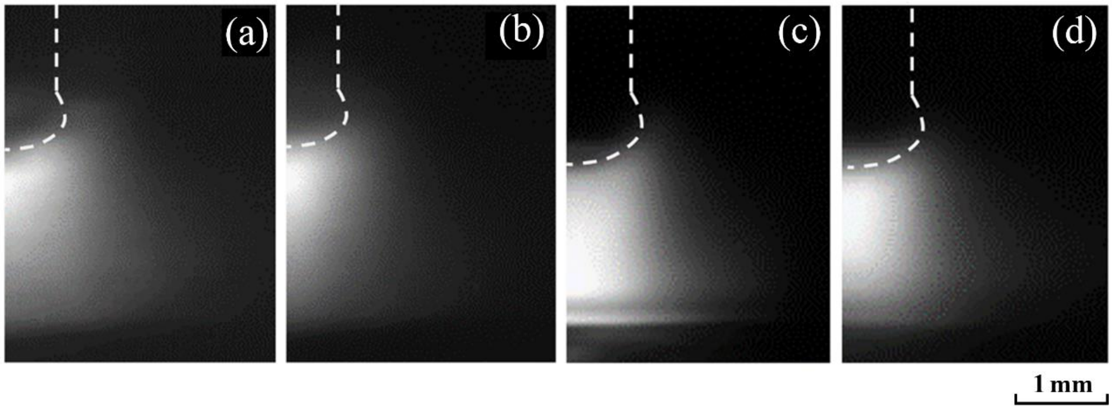

Figure 4.17 Line spectral images of (a) Fe I 538.3 nm line, MG-50 wire electrode with DCEP mode; (b) O I 777.3 nm line, MG-50 wire electrode with DCEP mode; (c) Fe I 538.3 nm line, KC-500 wire electrode with DCEP mode; (d) O I 777.3 nm line, KC-500 wire electrode with DCEP polarity.

Figure 4.19 (a) shows the concentration distribution of Fe vapor using MG-50 with DCEP polarity. The distribution shows the highest value of over 70 % mole fraction near the tip of the wire. Similarly, for the KC-500 wire electrode, Figure 4.18 (b) shows that the highest value of concentration distribution was over 70 % mole fraction near the tip of the wire. Moreover, as a results of high-speed color images, the metal droplet transfer was globular transfer mode. The metal droplet was retained at the wire tip during its growth by surface tension and metal vapor jet reaction. It is well known that the presence of metal vapor decreases the plasma temperature by increasing the plasma radiation [69, 70]. That is the main factor for the temperature fall of central region observed in KC-500 and MG-50 wire electrode with DCEP mode.

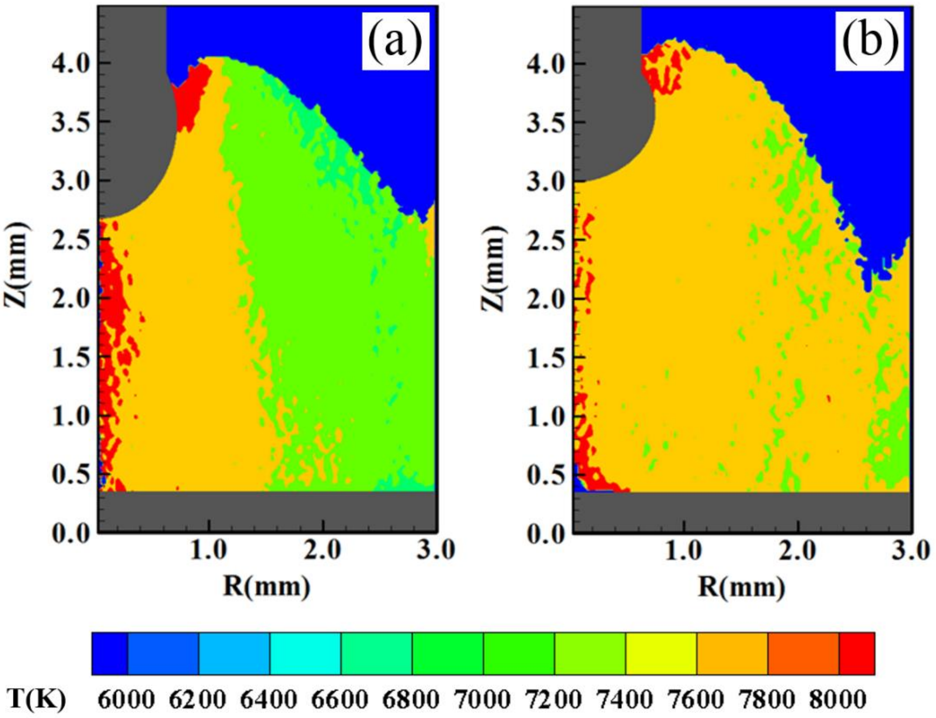

Figure 4.18 An instantaneous distribution of the plasma temperature of (a) MG-50 wire electrode and (b) KC-500 wire electrode in 300 A arc with DCEP polarity.

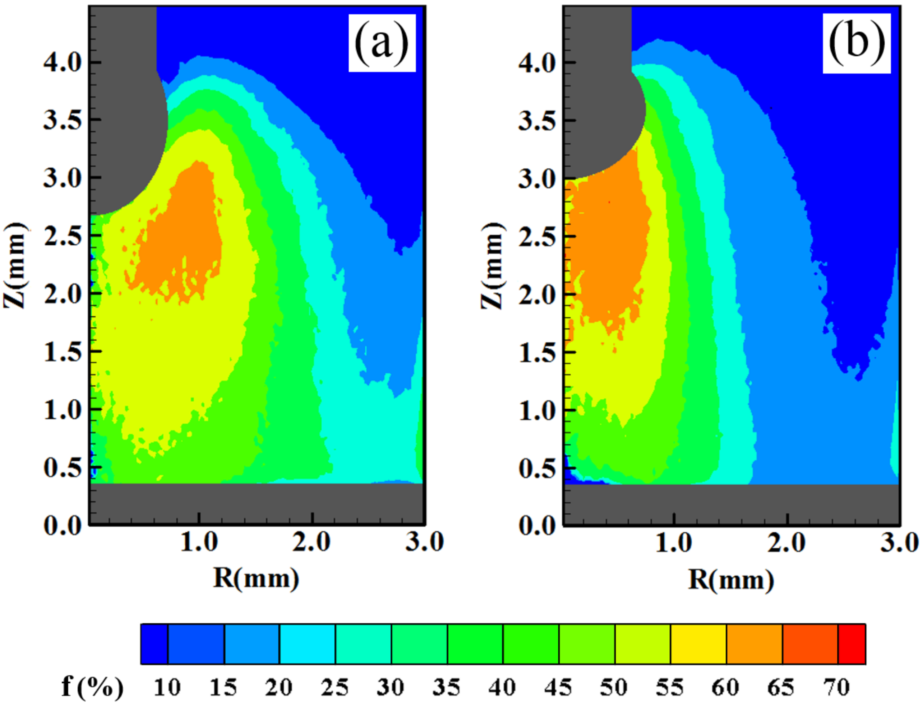

Figure 4.19 An instantaneous distribution of Fe vapor concentration for (a) MG-50 wire electrode and (b) KC-500 wire electrode in 300 A arc with DCEP polarity.

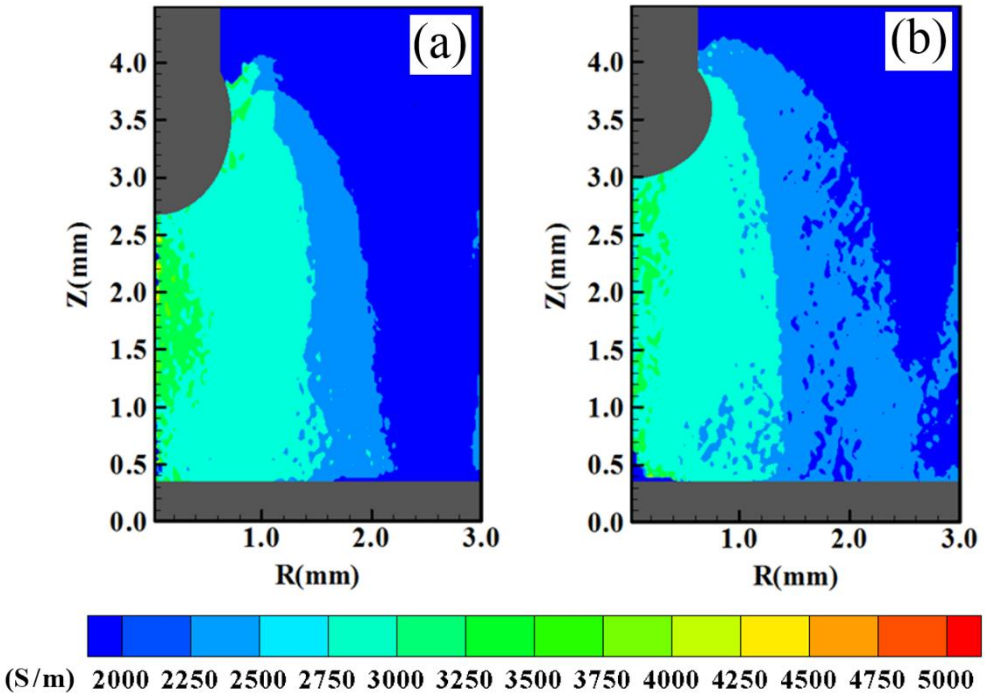

Figure 4.20 An instantaneous distribution of the electrical conductivity distribution for (a) MG-50 wire electrode and (b) KC-500 wire electrode in 300 A arc DCEP polarity.

Figure 4.20 (a) and (b) shows the electrical conductivity distribution of the MG-50 and KC-500 wire electrode with DCEP mode. The results of both wire electrode show that the maximum electrical conductivity is located at the center of the arc column. It can be conjectured that the electrical current goes along the central axis of the arc column. The current density concentrates at the bottom tip of the metal droplet, which is the closest point to the base metal. The strong axial component of electromagnetic force can be accomplished by high current density at the bottom tip of the metal droplet. When the current lines diverge in the droplet, the Lorentz force acts at right angles to these current lines [11]. An increasing force in the lower part of the droplet which induces an upward movement of globule developed at the tip of the wire electrode [24].

4.3.4 Cathode spot behavior of rare earth metal-added wire electrode with pure carbon dioxide shielding gas

The relationship of the current density of a thermionic emission to the work function and temperature of the emitting material can be derived from the Richardson-Dushman equation [71, 72]. This equation shows that an increase of the current density at the cathode corresponds to a significant decrease in the work function. Meanwhile, the lower work function of REM in the KC-500 wire electrode makes the emission of electrons more efficient and works to stabilize the cathode spot in DCEN mode. It can demonstrate that the high current density at the cathode tip and electrical current going through the arc at the region apart from arc axis as shown in Figure 4.16 can produce the Lorentz force [70], resulting high pinching effect that can promote the droplet detachment. As shown in Figure 4.11 (d), the spray transfer mode was observed and this mode resulted in smooth and uniform weld beads.

All things considered, the results of the KC-500 wire electrode with DCEN mode showed that the arc plasma had a dual structure consisting of a high-temperature region apart from the arc axis and a low temperature region near the arc axis due to the influence of the metal vapor. The effects of REM elements on the emission of electrons may have a significant influence on the high current density and electromagnetic pinch force at the tip of wire electrode. We have demonstrated that a stable spray transfer mode with lower amount of spatter can be achieved by using KC-500 wire electrode with DCEN mode for given welding conditions. Unlike the conventional wire electrode with pure carbon dioxide shielding gas, the process does not exhibit a spray transfer mode. The result shows poor appearance of weld bead and high levels of spatter.

4.4 Effect of shielding gas composition on the plasma characteristics of rare earth metal-added wire electrode

This section, the influence of shielding gas mixture between carbon dioxide and argon gas on REM-added wire electrode were discussed in terms of its influence on the arc temperature, metal vapor concentration and droplet transfer characteristics. The spectroscopic data were transformed to the plasma temperature and metal vapor concentration using data processing under the assumption of local thermodynamic equilibrium (LTE).

The GMAW was performed with a direct current power source and conventional GMAW torch. The distance between contact tip to base metal was 20 mm. Six shielding gas compositions, pure argon, pure carbon dioxide, 80% Ar + 20% CO_2, 60% Ar + 40% CO_2, 40% Ar + 60% CO_2 and 20% Ar + 80% CO_2, were considered in the study. The gas flow rate was set at 20 L min^{-1}. The welding was performed using direct current polarity with a welding current of 300 A on carbon base metal JIS G 3101 SS400 with thickness of 10 mm. The travel speed was 60 cm min^{-1}. This research, GMAW was performed with two types of wire electrode, JIS Z3312 YGW11 MG-50 and JIS Z3312 YGW11 KC-500. The wire diameter of used in this research was 1.2 mm and the chemical composition of wire electrode are given in Table 3.3 in chapter 3.

The spectra of Ar I 696.5 nm line was chosen to measure arc plasma temperature of GMAW with pure argon, 40% CO_2 + 60% Ar and 20% CO_2 + 80% Ar shielding gas mixtures because of its separation from other lines and its strong maximum emission coefficient. The spectra of O I 777.3 nm line was chosen to measure arc plasma temperature of GMAW with pure carbon dioxide, 80% CO_2 + 20% Ar, and 60% CO_2 + 40% Ar shielding gas mixtures.

4.4.1 Arc appearance of GMAW with difference shielding gas composition

Figure 4.21 and Figure 4.22 showed the colour images of the arc plasma and metal droplet transfer at the time after detachment of droplet of the YGW11 MG-50 wire electrode with DCEP polarity and the YGW11 KC-500 wire electrode with DCEN polarity, respectively. The arc plasma images were captured from the direction which was perpendicular to travel direction. The metal droplets were formed at the tip of wire electrode and then detached to the weld pool. As shown in Figure 4.21 (a) to (f), it was seen that the metal droplet was obviously larger than the diameter of wire electrode at the welding with pure carbon dioxide, 80% CO_2 + 20% Ar, 60% CO_2 + 40% Ar, 40% CO_2 + 60% Ar and 20% CO_2 + 80% Ar shielding gas. In contrast, the metal droplet was smaller than the diameter of wire electrode and the transfer mode became spray transfer mode at the pure Ar shielding gas.

When welding with the YGW11 MG-50 wire electrode, as shown in Figure 4.21, it was clearly identified that the arc-anode attachment region was increased gradually with increasing argon content in shielding gas and the arc was covered the entire droplet and the transfer mode became spray transfer mode at the welding of pure argon shielding gas, which has a low-ionization energy.

Figure 4.22 showed the colour images of the arc plasma and metal droplet transfer at the time after detachment of droplet of the YGW11 KC-500 wire electrode with DCEN polarity. The results showed that the metal droplet size tended to gradually increase with increasing argon content in shielding gas which was opposite behaviour to conventional wire electrode of YGW11 MG-50. The metal transfer mode was spray transfer at the welding with pure carbon dioxide, 80% CO_2 + 20% Ar, 60% CO_2 + 40% Ar shielding gas. Furthermore, it can be seen that the arc profile was conical arc shape with a short arc length. These metal transfer behaviour was affected by REM elements. These changes could be caused by the lower the work function of the filler wire material and could thus make the emission of electrons more efficient and stabilize the arc-cathode attachment region.

In contrast, the metal droplet was larger than the diameter of wire electrode and the transfer mode became globular transfer at the conditions of 40% CO_2 + 60% Ar, 20% CO_2 + 80% Ar and pure argon shielding gas. Moreover, it was clearly seen that the arc-cathode attachment region was increased gradually with increasing argon content in shielding gas.

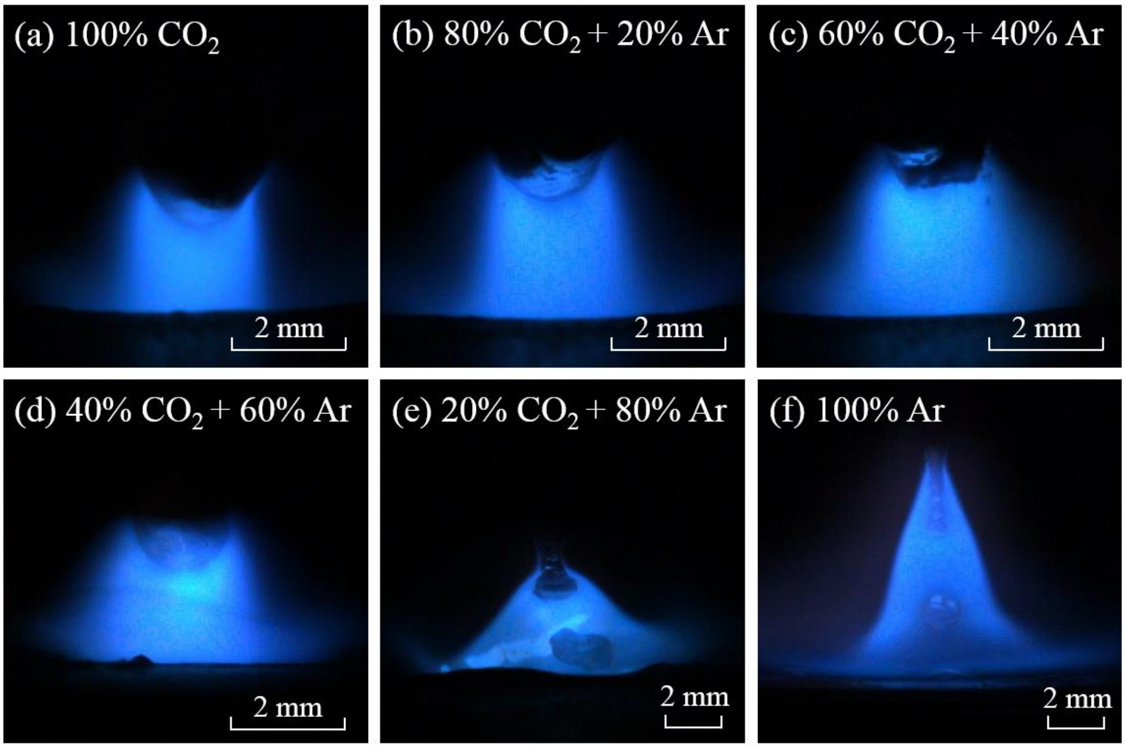

Figure 4.21 Arc appearance of GMAW of difference shielding gas compositions using YGW11 MG-50 with DCEP polarity (a) pure carbon dioxide; (b) 80% CO_2 + 20% Ar; (c) 60% CO_2 + 40% Ar; (d) 40% CO_2 + 60% Ar; (e) 20% CO_2 + 80% Ar; (f) pure argon.

When welding with the YGW 11 KC-500 wire electrode using Ar- reached shielding gas, as shown in Figure 4.22 (d) – (f), the arc-cathode attachment region were moved rapidly. These arc-cathode attachment behaviours and their high mobility are a result of many complex reactions within arc stream and at the cathode [67, 68]. In addition, these types of arc attachment ware classified as spot mode with a highly constricted attachment on cathode [73].

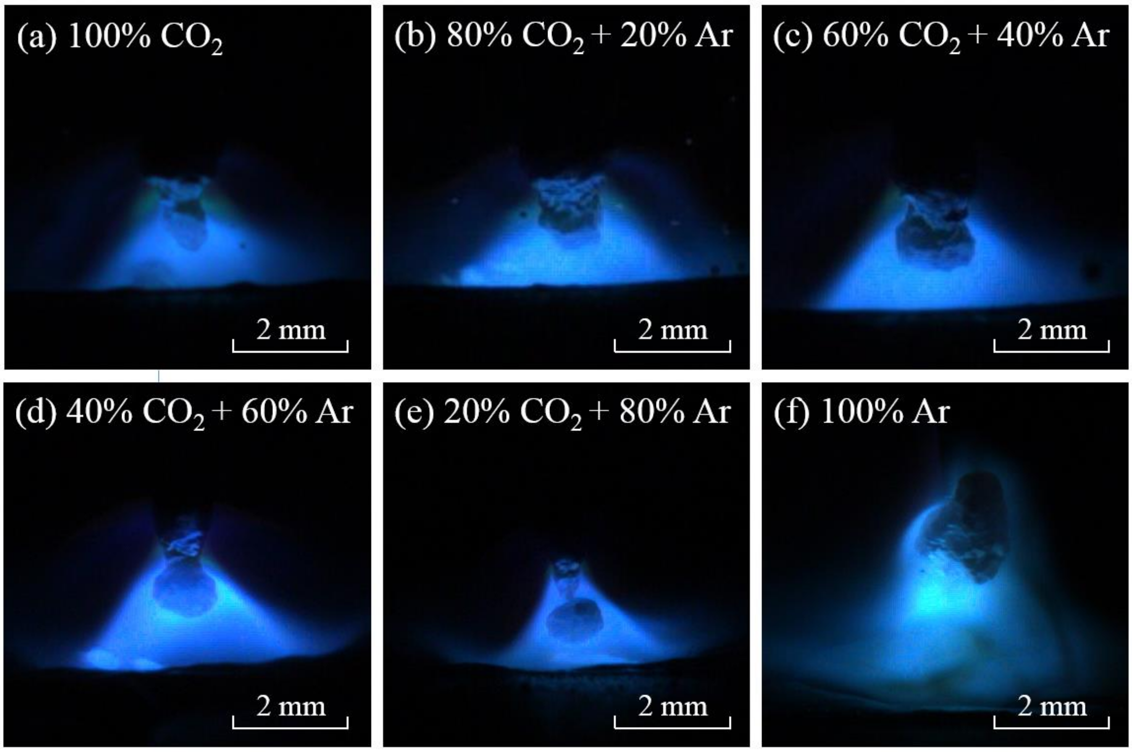

Figure 4.22 Arc appearance of GMAW of difference shielding gas compositions using YGW11 KC-500 with DCEN polarity (a) pure carbon dioxide; (b) 80% CO_2 + 20% Ar; (c) 60% CO_2 + 40% Ar; (d) 40% CO_2 + 60% Ar; (e) 20% CO_2 + 80% Ar; (f) pure argon.

4.4.2 Effect of shielding gas composition on metal droplet detachment frequency

Shielding gas is used not only protect the molten drop and the welded bead, but also to influence metal transfer mode. The molten drop was often repelled by the electromagnetic force and vapor pressure due to vaporization of alloying elements and their oxides. Figures 4.23 showed the droplet detachment frequency of GMAW using YGW 11 MG-50 wire electrode with DCEP polarity. The droplet detachment frequency for pure argon shielding gas was observed to be much higher than those of either pure carbon dioxide or CO_2-argon gas mixtures. With carbon dioxide and CO_2-argon gas mixtures, the droplet detachment frequency was decreased with increasing carbon dioxide content in shielding gas. The reason was that a high content of carbon dioxide increased the energy potential, thereby increasing the current density and the reduction in surface tension due to oxidation by carbon dioxide.

Figures 4.24 showed the droplet detachment frequency of GMAW using the YGW 11 KC-500 wire electrode with DCEN polarity. The results showed that the droplet detachment frequency for pure carbon dioxide suddenly increased and become spray transfer mode at the welding current range of 220 – 240 A. It can be seen that, the droplet detachment frequency gradually decreased with increasing argon content in shielding gas. In all welding currents ranging from 160 – 340 A, the droplet detachment frequency was constant at around 10-20 drop/second for pure argon shielding

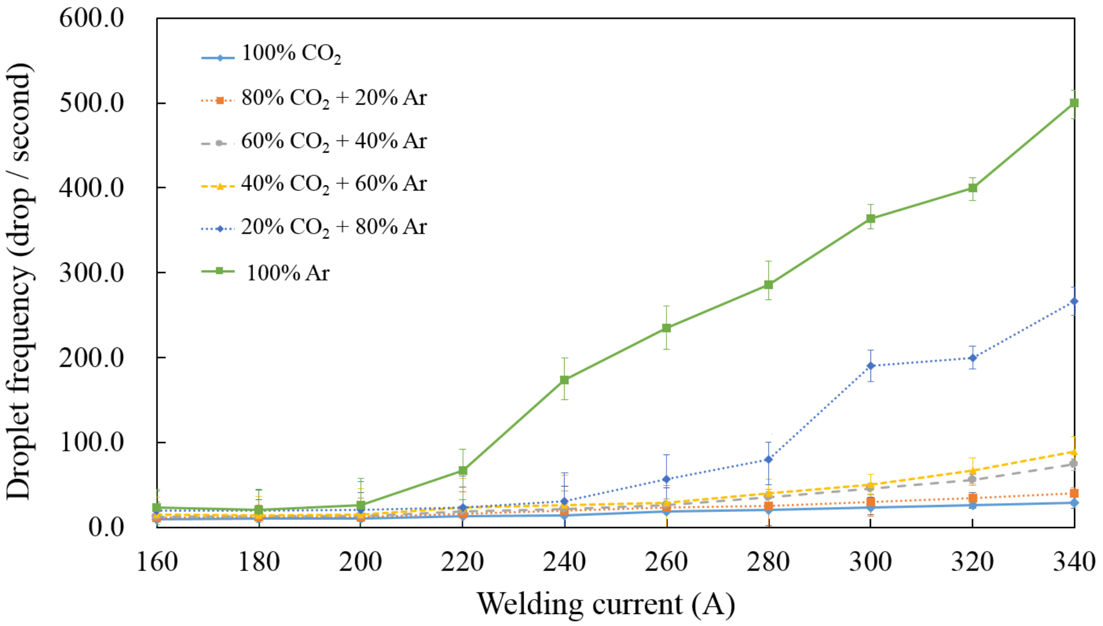

Figure 4.23 Influence of welding current on droplet frequency using 1.2 mm YGW 11 MG-50 wire electrode with DCEP polarity.

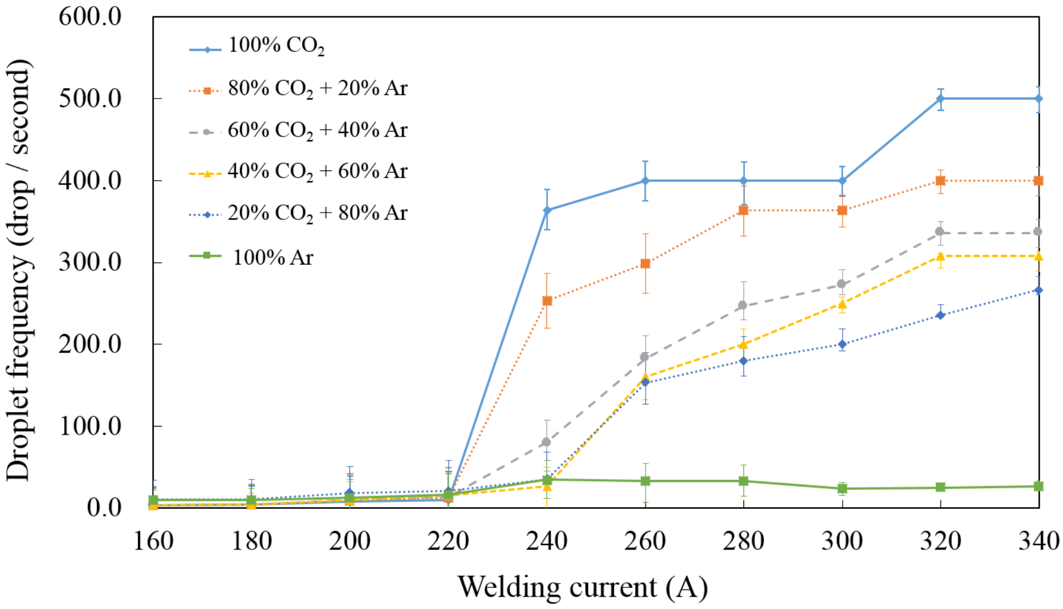

Figure 4.24 Influence of welding current on droplet frequency using 1.2 mm YGW 11 KC-500 wire electrode with DCEN polarity.

4.4.3 Instantaneous distribution of plasma temperature

Figure 4.25 and Figure 4.26 showed the instantaneous distribution of plasma temperature with different shielding gas compositions of the YGW11 MG-50 wire electrode with DCEP polarity and the YGW11 KC-500 wire electrode with DCEN polarity, respectively. These temperatures were calculated using the Fowler-Milne method. As shown in Figure 4.25, it was seen that the profile shapes of temperature change depending on metal transfer mode and shielding gas composition. When welding with the YGW11 MG-50 wire electrode, the high temperature region gradually moved away from the arc axis when increasing argon content in argon-CO$_2$ shielding gas. In the same way, the high temperature region moved away from the arc axis when the transfer mode changes from globular (see Figure 4.25 (a) to (e)) to spray transfer (see Figure 4.25 (f)). With CO$_2$-argon gas mixtures, the metal transfer mode was globular transfer and the high temperature region still included the arc axis. The uniform distribution of plasma was found in the arc axis with the average temperature around 7,500 K. Conversely, at pure argon shielding gas condition, the arc plasma had a two-layer structure. The high temperature region existed away from the arc axis and low temperature exists near the arc axis. The plasma temperature was reached around 12,500 K to 13,000 K.

Figure 4.26 showed the instantaneous distribution of plasma temperature of the YGW11 KC-500 wire electrode with DCEN polarity. The results showed opposite behaviour to the YGW11-MG50 wire electrode. When using CO_2-reached shielding gas (pure carbon dioxide, 80% CO_2 + 20% Ar, 60% CO_2 + 40% Ar shielding gas), the arc plasma had a two-layer structure of high–temperature region away from the arc axis and low–temperature region near the arc axis. Accordingly, the temperature distribution showed the highest value of over 13,500 K in a region apart from the arc axis. The corresponding plasma temperature in the case of Ar-reached shielding gas as shown in Figure 4.26 (d) to (f), which showed the lower temperature distribution compared with CO_2-reached shielding gas conditions. The temperature distribution showed the highest value over 7,500 K in the region of arc axis near the metal droplet.

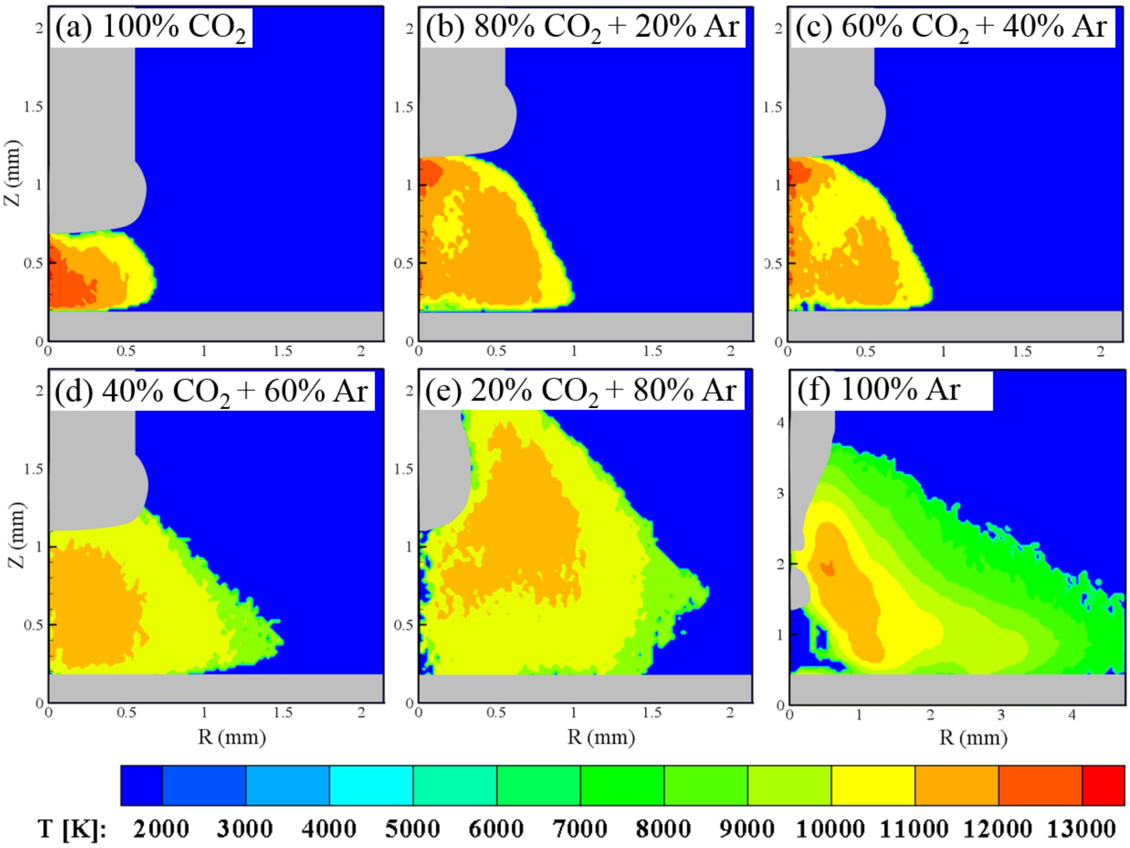

Figure 4.25 Instantaneous distribution of plasma temperature of GMAW of difference shielding gas compositions using YGW11 MG-50 with DCEP polarity (a) pure carbon dioxide; (b) 80% CO_2 + 20% Ar; (c) 60% CO_2 + 40% Ar; (d) 40% CO_2 + 60% Ar; (e) 20% CO_2 + 80% Ar; (f) pure argon.

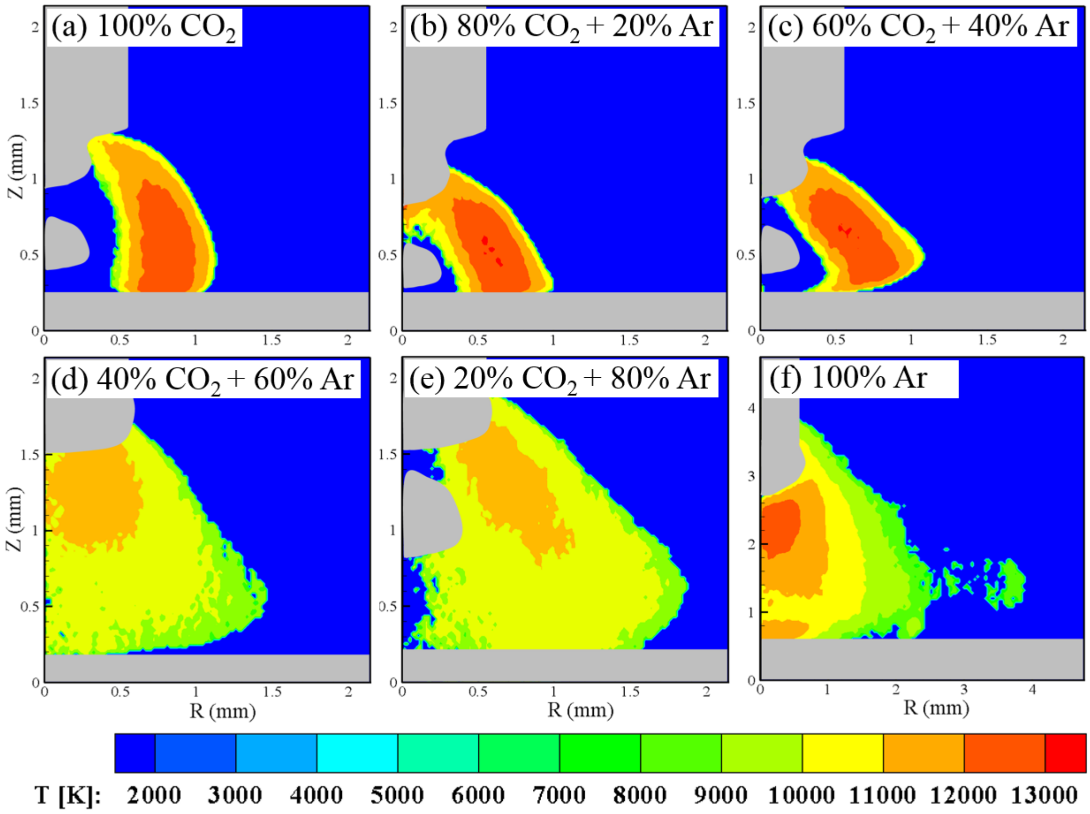

Figure 4.26 Instantaneous distribution of plasma temperature of GMAW of difference shielding gas compositions using YGW11 KC-500 with DCEN polarity (a) pure carbon dioxide; (b) 80% CO_2 + 20% Ar; (c) 60% CO_2 + 40% Ar; (d) 40% CO_2 + 60% Ar; (e) 20%CO_2 + 80% Ar; (f) pure argon.

4.4.4 Instantaneous distribution of Fe plasma temperature

Figure 4.27 and Figure 4.28 showed the instantaneous distribution of Fe plasma temperature with different shielding gas compositions of the YGW11 MG-50 wire electrode with DCEP polarity and the YGW11 KC-500 wire electrode with DCEN polarity, respectively. These temperatures were calculated from the iron lines intensity ratio of Fe I 537.1 nm and Fe I 538.3 nm using two-lines relative intensity method. It can be seen that the profile shapes of temperature slightly changed. In all shielding gas compositions, the uniform distribution of Fe plasma was found in the arc axis with the average temperature around 7,500 – 8,000 K. These results indicated that the temperature of Fe plasma was lower than that of argon and carbon dioxide plasma.

As shown in Figure 4.25 (f) and 4.27 (f), the plasma temperature and Fe plasma temperature for pure Ar shielding gas had a two-layer structure. The high temperature region exists away from the arc axis (see Figure 4.25 (f)) and low temperature region of Fe plasma exists near the arc axis (Figure 4.27 (f)). It can be clearly identified that the welding of YGW11 MG-50 wire electrode with pure argon shielding gas can produced spray transfer mode with a two-layer structure of arc plasma.

Figure 4.28 showed the Fe plasma temperature distribution of the YGW11 KC-500 wire electrode with DCEN polarity. The corresponding plasma temperature in the case of CO_2-reached shielding gas as shown in Figure 4.26 (d) – (f), which showed the conical arc shape with shorter arc length compared with YGW11 MG-50 wire electrode with DCEP polarity. It was noted that the lower the work function of REM elements in filler wire material might influence plasma behavior and droplet transfer mode as described above.

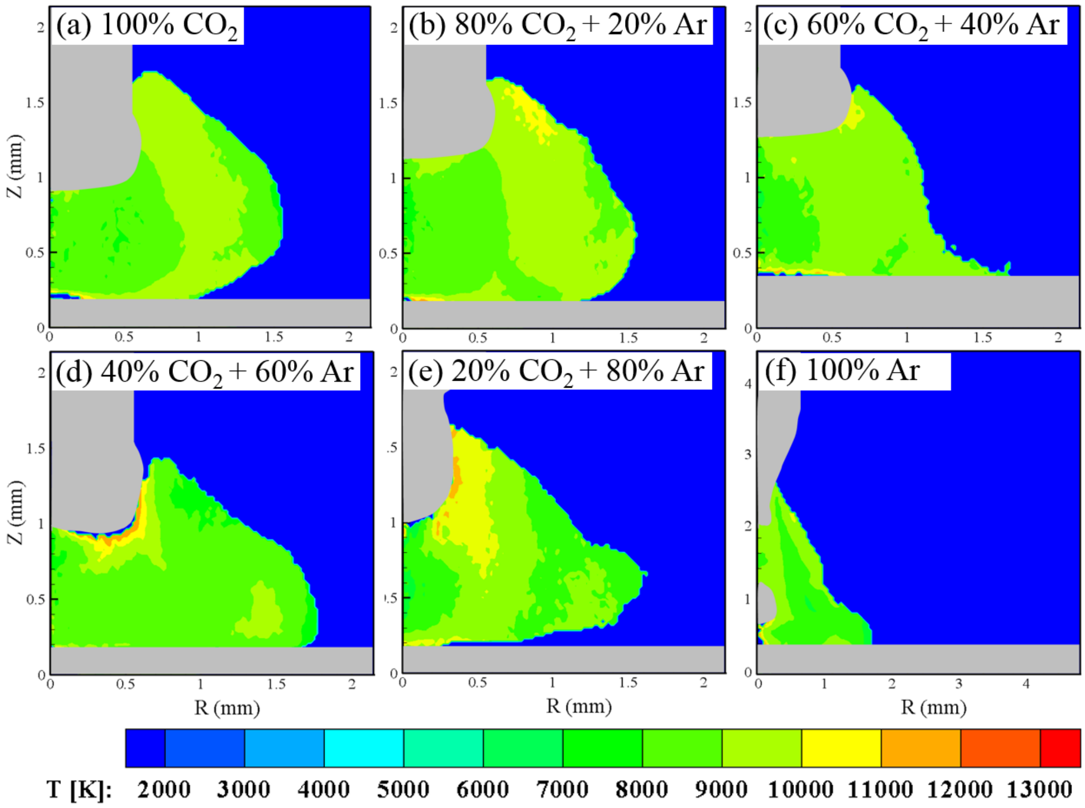

Figure 4.27 Instantaneous distribution of Fe plasma temperature of GMAW of difference shielding gas compositions using YGW11 MG-50 with DCEP polarity (a) pure carbon dioxide; (b) 80% CO_2 + 20% Ar; (c) 60% CO_2 + 40% Ar; (d) 40% CO_2 + 60% Ar; (e) 20% CO_2 + 80% Ar; (f) pure argon.

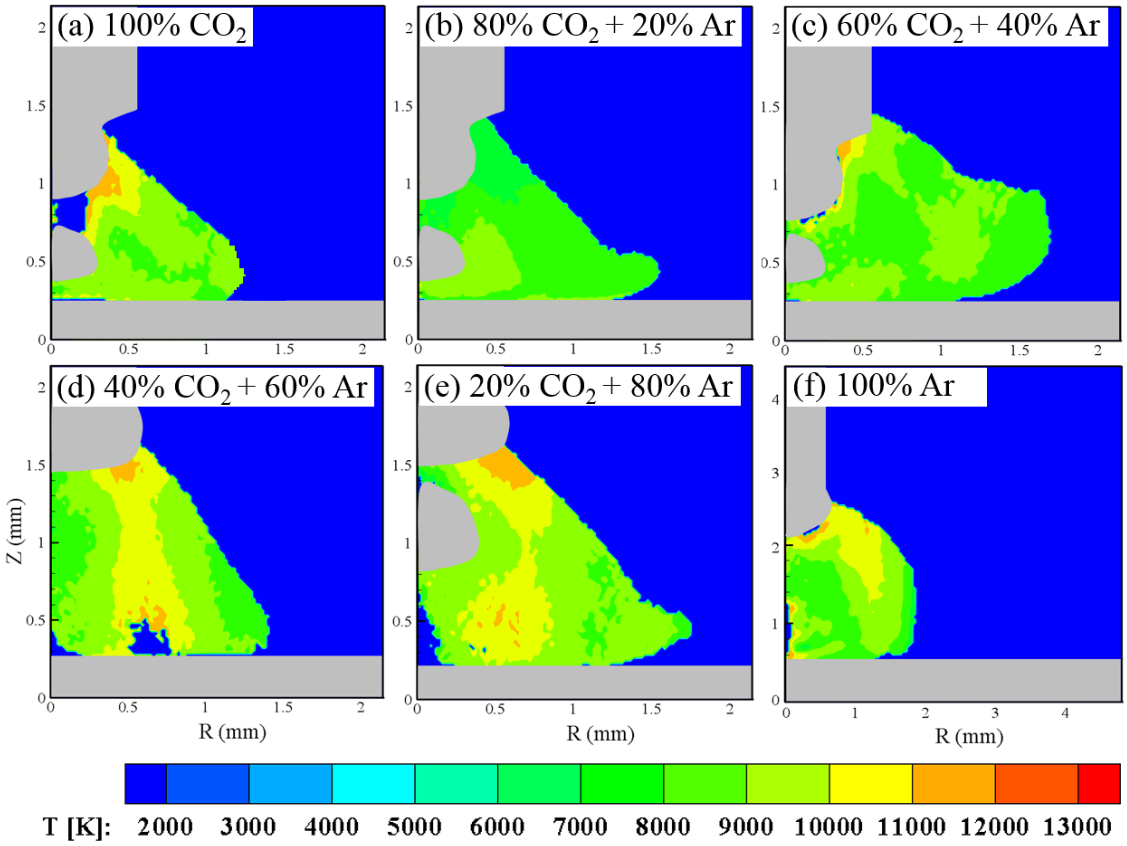

Figure 4.28 Instantaneous distribution of Fe plasma temperature of GMAW of difference shielding gas compositions using YGW11 KC-500 with DCEN polarity (a) pure carbon dioxide; (b) 80% CO_2 + 20% Ar; (c) 60% CO2 + 40% Ar; (d) 40% CO_2 + 60% Ar; (e) 20% CO_2 + 80% Ar; (f) pure Ar.

4.4.5 Behavior of metal vapor concentration in plasma

Figure 4.29 and Figure 4.30 showed the instantaneous distribution of Fe vapor concentration with different shielding gas compositions of the YGW11 MG-50 wire electrode with DCEP polarity and the YGW11 KC-500 wire electrode with DCEN polarity, respectively. It was demonstrated that the concentration of Fe vapor showed the highest value near the tip of the wire electrode. It can be explained that the ohmic heating might promote the vaporization of Fe at the surface of wire electrode. As shown in Figure 4.29, the distribution showed the highest value over 75 % mole fraction near the tip of the wire. However, the distribution was ranging from 65 % to 75 %

It was observed that the distribution of Fe vapor concentration was located at the arc axis. Further, as shown in Figure 4.29 (f), the concentration of Fe vapor in case of pure argon shielding gas was located at the region of low plasma temperature (see Figure 4.25 (f)). It was well-known that the presence of metal vapor is found to have two major effects on the temperature distribution in the arc. First, the temperature is strongly decreased. Second, a local minimum in the dependence of temperature on arc radius is formed on the arc axis due to the increased radiative emission [27 – 29]. That was the main factor for the temperature fall at central region observed in YGW11 MG-50 wire electrode with DCEP polarity with pure argon shielding gas.

Figure 4.30 showed the instantaneous distribution of Fe vapor concentration of the YGW11 KC-500 wire electrode with DCEN polarity. The distribution showed the highest value over 85 % mole fraction near the tip of the wire. It was clearly identified that Fe vapor concentration was higher than that of the YGW11 MG-50 wire electrode. The effects of REM elements on the emission of electrons might have a significant influence on the high current density and also a high concentration of electrode metal vapor near the tip of wire electrode.

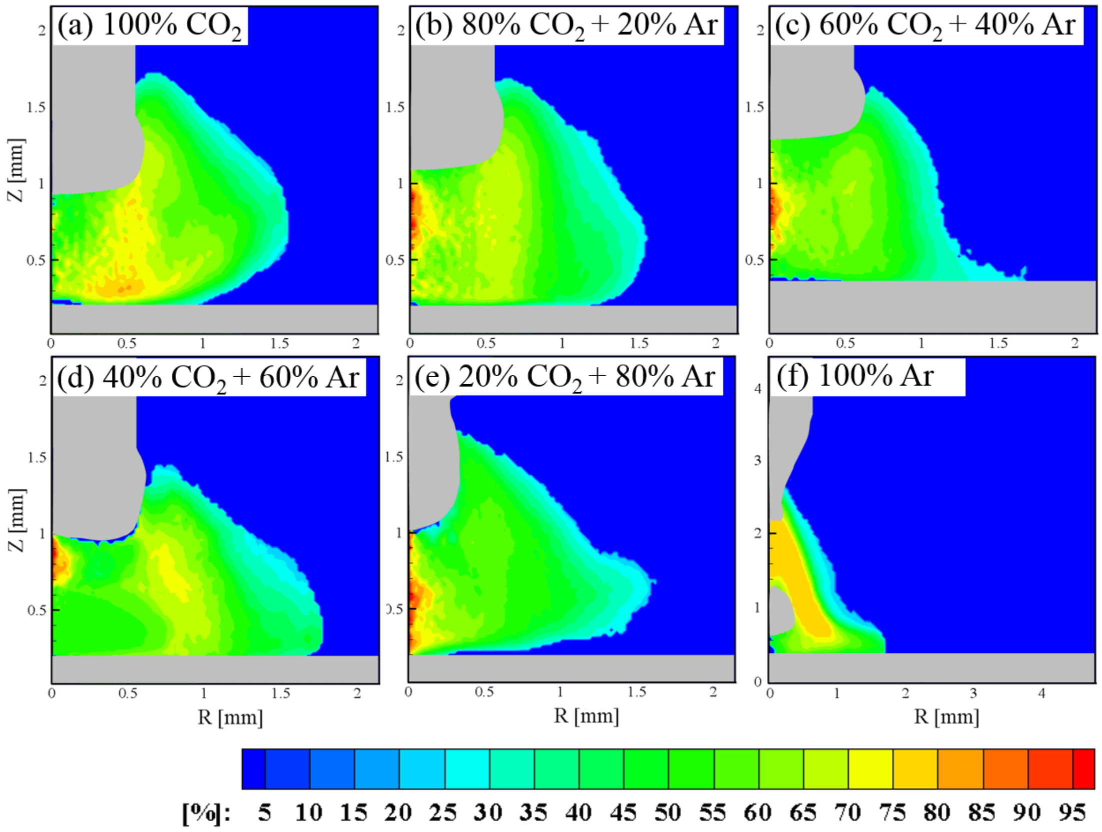

Figure 4.29 Instantaneous distribution of Fe vapour concentration of GMAW of difference shielding gas compositions using YGW11 MG-50 with DCEP polarity (a) pure carbon dioxide; (b) 80% CO_2 + 20% Ar; (c) 60% CO_2 + 40% Ar; (d) 40% CO_2 + 60% Ar; (e) 20% CO_2 + 80% Ar; (f) pure argon.

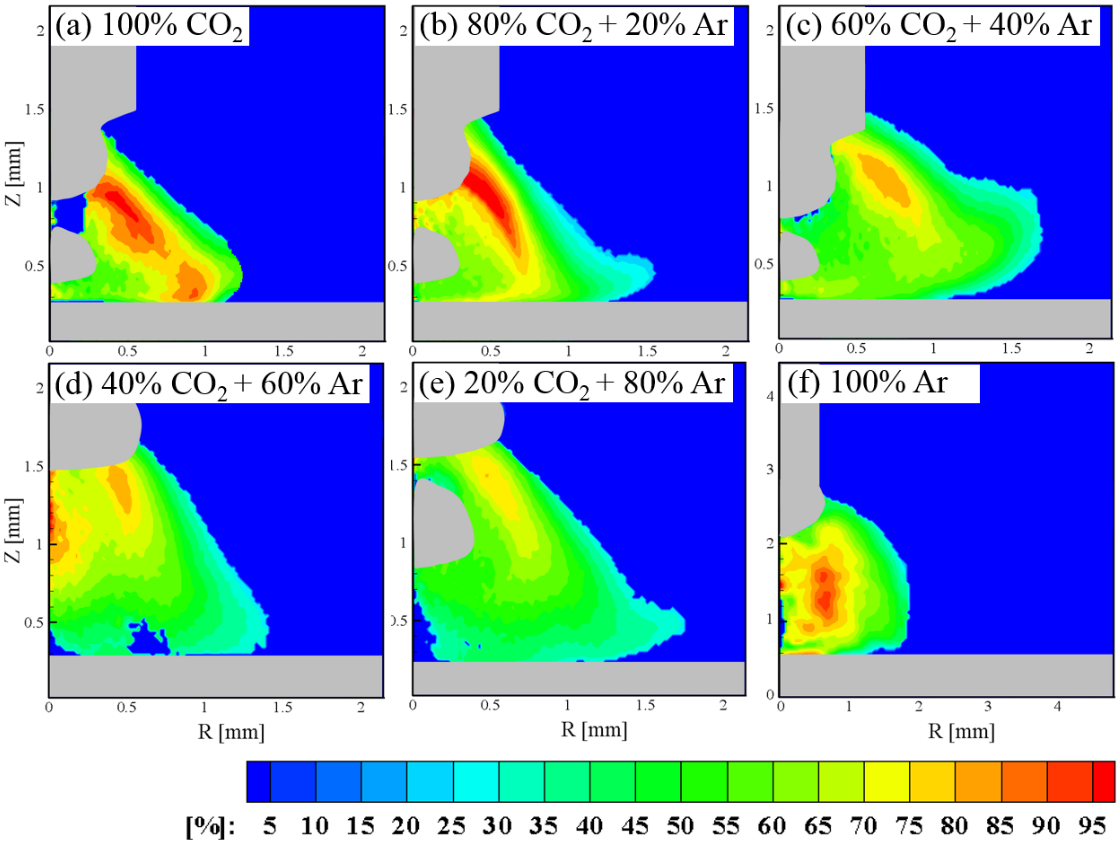

Figure 4.30 Instantaneous distribution of Fe vapour concentration of GMAW of difference shielding gas compositions using YGW11 KC-500 with DCEN polarity (a) pure carbon dioxide; (b) 80% CO_2 + 20% Ar; (c) 60% CO_2 + 40% Ar; (d) 40% CO_2 + 60% Ar; (e) 20% CO_2 + 80% Ar; (f) pure argon.

4.4.6 Influences of rare earth metal elements on GMAW arc plasma

The relationship of the current density of a thermionic emission to the work function and temperature of the emitting material can be derived from the Richardson-Dushman equation [71, 72]. This equation showed that an increase of the current density at the cathode significantly decreased the work function. Meanwhile, the lower work function of REM in the YGW11 KC-500 wire electrode can emit electrons more efficiently and stabilize the cathode spot in DCEN mode with CO_2-reached shielding gas. Consequently, high current density at the cathode tip and electrical current going through the arc can produce the Lorentz force [70], resulting in high pinching effect that can promote the droplet detachment. As shown in Figure 4.22 (a) - (b), the spray transfer mode was observed, resulting in smooth and uniform weld beads.

4.5 Effect of rare earth metal on metal droplet temperature

In this section, two-color temperature measurement is adopted to obtain the temperatures of metal droplets during GMAW with pure carbon dioxide shielding gas. The YGW11 MG-50 and YGW11 KC-500 wire electrodes were used in the experiment. Metal droplets are also photographed by a high-speed digital color camera (Phantom Miro eX1) with two-color temperature measurement algorithm (Thermera-HS, Nobby-tech). The theoretical intensity ratio of red to green sensors is converted into the temperature.

During arc welding of GMAW with pure carbon dioxide shielding gas, the metal droplet is covered with the arc plasma. It is difficult to measure the droplet temperature distribution. Therefore, the droplet temperature is measured immediately after the arc is extinguished. Each image is taken by different image color sensors corresponding to their respective wavelength sensitivities [74]. The welding power source was controlled by wave form control, this function can switching instantaneously from the welding current to a low current within 0.5 ms. The evaluation of the accuracy of metal droplet temperature measurement was showed in section 2.11.

Figure 4.31 shows a photograph and a two-dimensional distribution of the droplet temperature immediately after the arc plasma is extinguished of MG-50 wire electrode with DCEP polarity. White-dashed lines show the outline of the wire electrode. The result shows that the temperature at the lower area of the droplet is higher locally. As the result in section 4.1 and 4.3, the behaviors of GMAW arc plasma using pure carbon dioxide shielding gas was concentrated and constricted at the center of arc column. So, it can be conjectured that the arc root is located near bottom of molten metal droplet. The maximum surface temperature was 2,600 K located at bottom tip of molten droplet (the same area of arc root). However, the average surface temperature was 2,100 K. With DCEP welding polarity, the base metal is negative and the greatest amount of heat goes into the part where the electrons can be more stably emitted. This is primarily due to oxides on the base metal surface, which facilitate the electron emission process. The end result is a much more stable arc, Accordingly, DCEP polarity with conventional wire electrode is used almost exclusively with GMAW.

Figure 4.32 shows a photograph and a two-dimensional distribution of the droplet temperature of

MG-50 wire electrode with DCEN polarity. It clearly seen that the temperature distribution was lower and more uniform compared with MG-50 wire electrode with DCEP polarity. The average surface temperature was 1,900 K. The thermionic emission of wire electrode might difficult to achieve with this surface temperature range of the metal droplet. Thus, in GMAW of conventional carbon steel wire electrode with DCEN polarity produces an arc that very erratic and difficult to control due to lower surface droplet temperature and their high mobility of cathode spot.

Figure 4.33 shows a photograph and a two-dimensional distribution of the droplet temperature of KC-500 wire electrode with DCEP polarity. The average surface temperature was 1,900 -2,000 K. With DCEP polarity, the electron are emitted from base metal surface and goes through the molten metal droplet surface. Accordingly, the rare earth metal added wire electrode contained an elements that the electrons can easily emitted. So, the thermionic emission at the tip of wire electrode cannot achieve which causes the mobility of anode spot around molten droplet surface of wire electrode as seen in section 4.3.1.

Figure 4.34 shows a photograph and a two-dimensional distribution of the droplet temperature of KC-500 wire electrode with DCEN polarity. The average metal droplet temperature was around 2,500 K. This results showed the highest droplet temperature compared with other welding conditions. This change might be caused by the thermionic emission process of molten droplet of wire electrode. During arc, the molten droplet of wire electrode were performed having heated by conduction heat from arc plasma. The high metal droplet temperature coupled to the rare earth metal element in wire electrode of KC-500 can easily emitted electrons. So, the arc plasma of KC-500 electrode with DCEN polarity can provide highly efficiency of thermionic emission process. Accordingly, the concentration and constricted of arc plasma for carbon dioxide shielding gas can produces high electromagnetic pinch force. It can be concluded that the thermionic emission process of KC-500 wire electrode with pure carbon dioxide, resulting in a high concentration of conical arc shape, stable arc discharge with small molten droplet diameter liked spray transfer mode.

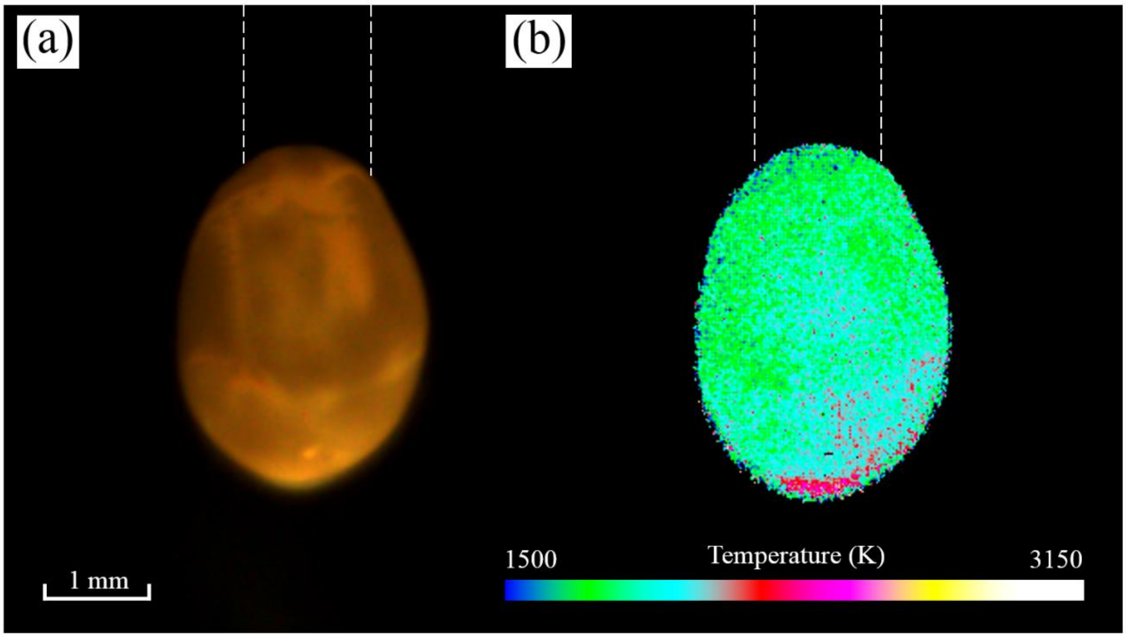

Figure 4.31 Metal droplet immediately after the arc is extinguished of MG-50 wire with DCEP polarity (a) High speed color image, (b) two-dimensional distribution of surface temperature

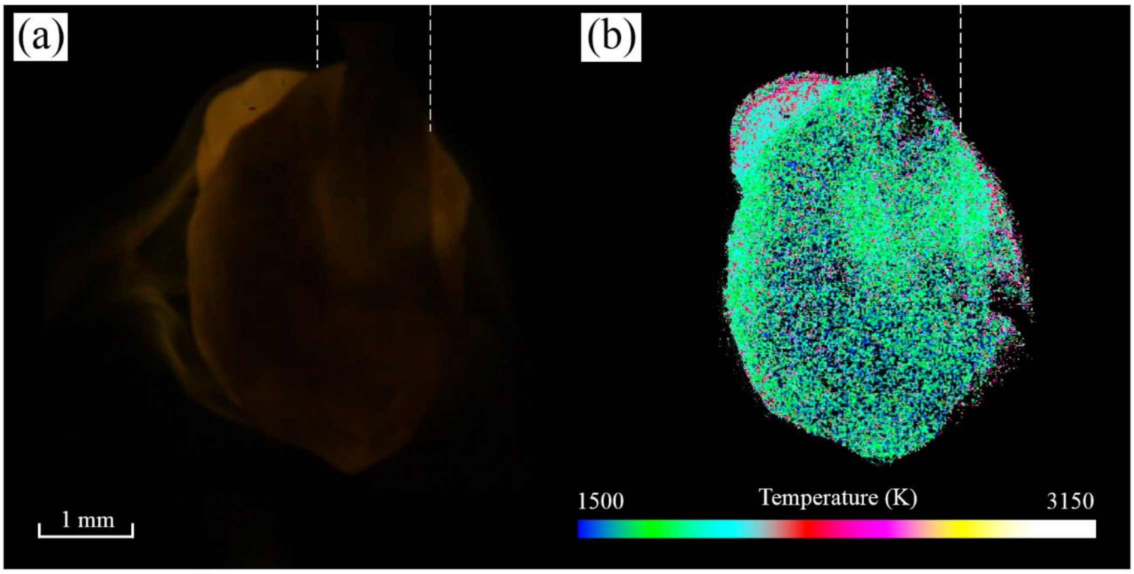

Figure 4.32 Metal droplet immediately after the arc is extinguished of MG-50 wire with DCEN polarity (a) High speed color image, (b) two-dimensional distribution of surface temperature

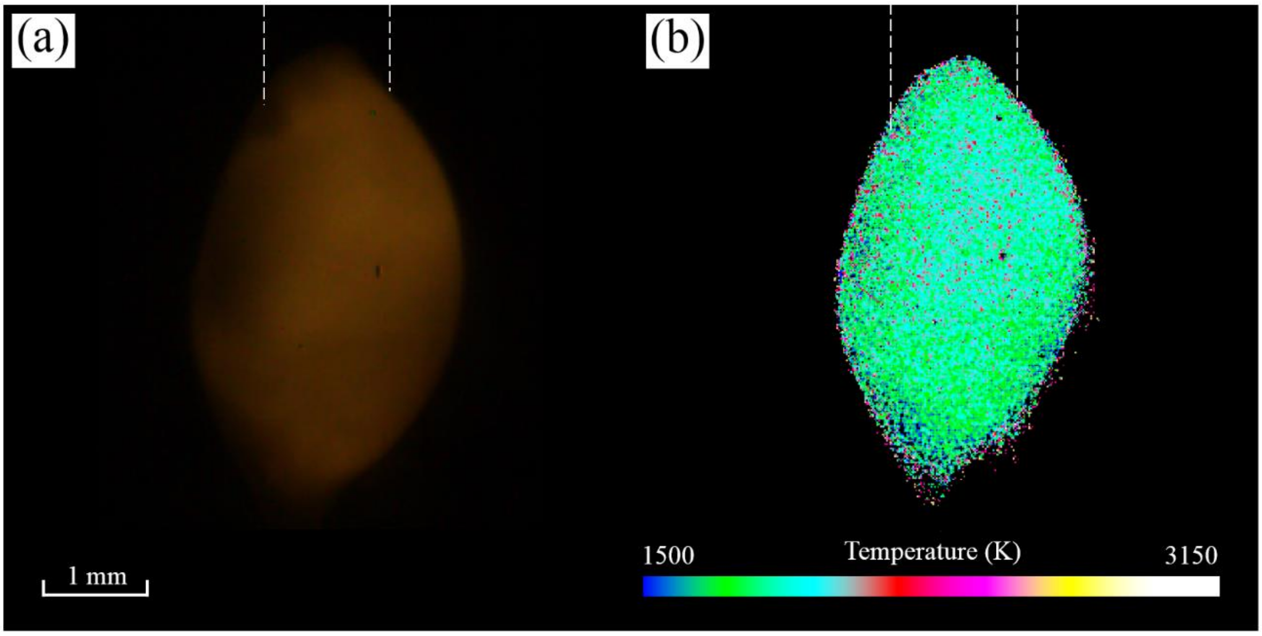

Figure 4.33 Metal droplet immediately after the arc is extinguished of KC-500 wire with DCEP polarity (a) High speed color image, (b) two-dimensional distribution of surface temperature

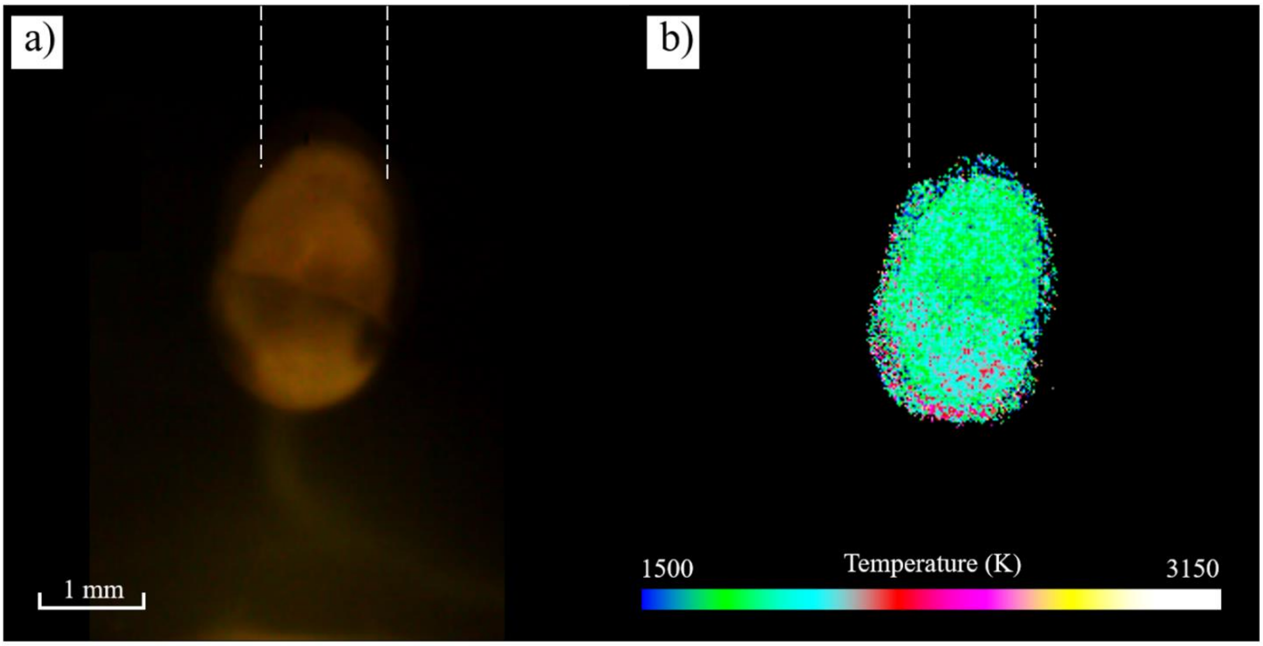

Figure 4.34 Metal droplet immediately after the arc is extinguished of KC-500 wire with DCEN polarity (a) High speed color image, (b) two-dimensional distribution of surface temperature

Chapter 5

Mechanisms of GMAW using carbon dioxide shielding gas

This chapter presents mechanisms of arc plasma characteristics, metal droplets transfer mode and surface temperature of metal droplet in gas metal arc welding with conventional carbon steel electrode (MG-50) and rare earth metal added wire electrode (KC-500) by compared between direct current electrode negative polarity and direct current electrode polarity.

During gas metal arc welding with MG-50 wire electrode, DCEP polarity using pure carbon dioxide shielding gas, the arc plasma was composed of carbon dioxide plasma and Fe plasma in the arc column and mixed together in arc column. The use of pure carbon dioxide shielding gas, the constricted arc plasma with highest plasma temperature was located near the arc axis. The highest plasma temperature can produced the highest metal droplet temperature located at the bottom tip of wire electrode near the arc root region. Moreover, the electrical goes through the arc plasma mainly in the arc axis and induced the strong axial component of the electromagnetic force or Lorentz force with high pressure below the tip of electrode. These force can induced the upward movement of repelled droplet and metal transfer mode becomes globular transfer mode. The schematic illustration of mechanisms of gas metal arc welding with MG-50 wire electrode, DCEP polarity shows in Figure 5.1 (a).

The use of MG-50 wire electrode with DCEN polarity, the arc plasma was also composed of carbon dioxide plasma and Fe plasma in the arc column and mixed together in arc column. The arc plasma behavior show that the unstable movement of cathode spot with lower surface droplet temperature. These behaviors were decrease time average of current density at the tip of wire electrode. The results of electromagnetic force or Lorentz force become low and plasma jet flow cannot induced the separation of Fe vapor and carbon dioxide plasma in arc column. Therefore, metal droplet transfer mode become globular transfer mode. The schematic illustration of mechanisms of gas metal arc welding with MG-50 wire electrode, DCEN polarity shows in Figure 5.1 (b).

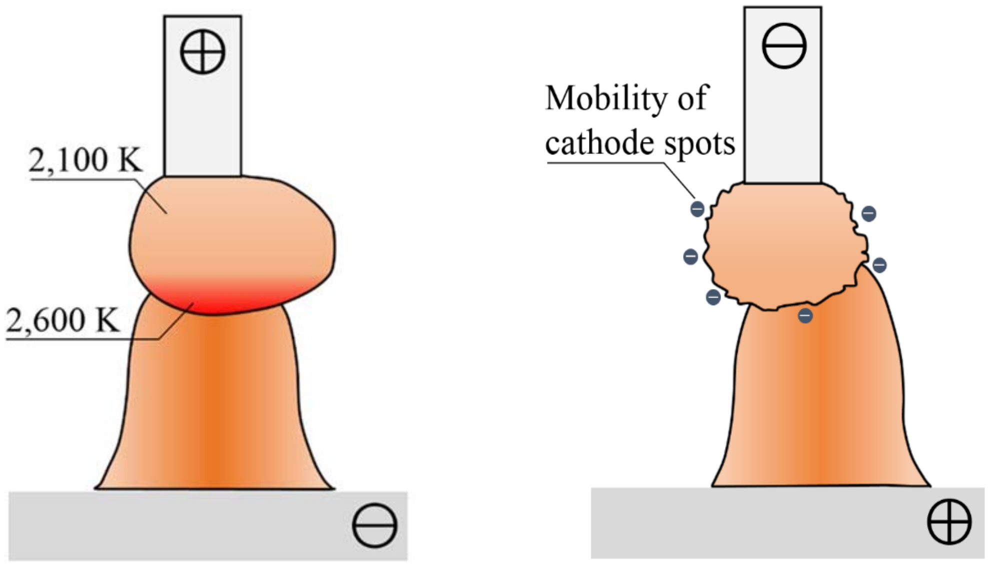

(a) MG-50 electrode, DCEP (b) MG-50 electrode, DCEN

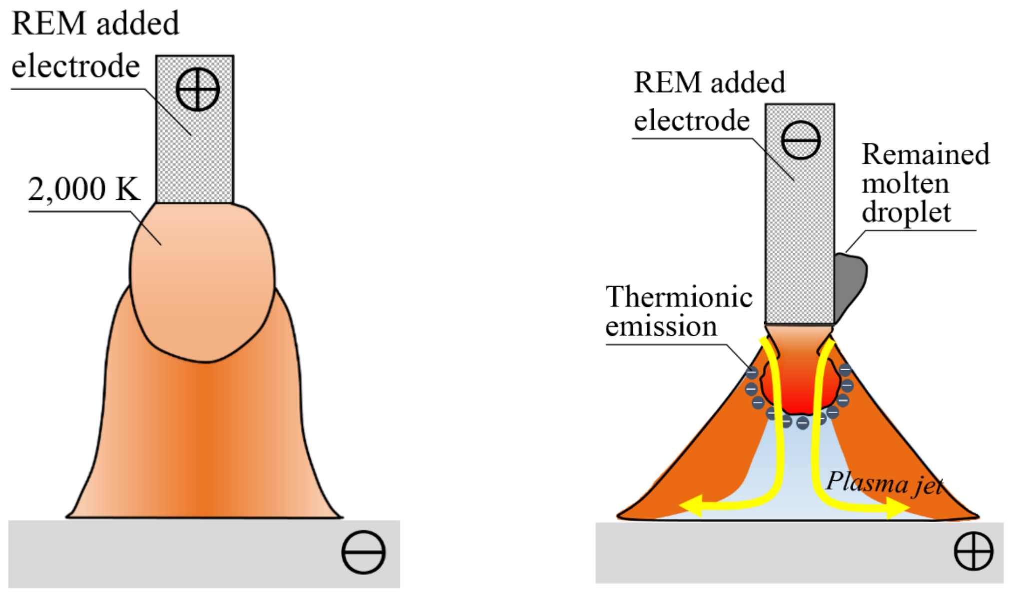

(c) KC-500 electrode, DCEP (d) KC-500 electrode, DCEN

Figure 5.1 Schematic illustration of the relationship of the plasma characteristic and metal droplet behavior of GMAW using pure carbon dioxide shielding gas: (a) MG-50 electrode, DCEP polarity; (b) MG-50 electrode with DCEN polarity; (c) KC-500 electrode, DCEN polarity; and (d) KC-500 electrode, DCEN polarity.

The gas metal arc welding with rare earth metal added wire electrode (KC-500) using DCEP polarity showed the arc plasma characteristics nearly the same as MG-50 wire electrode with DCEP polarity in which the arc plasma was composed of carbon dioxide plasma and Fe plasma in the arc column and mixed together in arc column. The arc attachment region was wider area around the tip of metal droplet. The diffuse of arc attachment region was effected to the uniform droplet temperature and decreasing of melting rate of wire electrode. However, metal droplet transfer mode become globular transfer. The schematic illustration of mechanisms of gas metal arc welding with KC-500 wire electrode, DCEP polarity shows in Figure 5.1 (c).

Lastly, the use of KC-500 wire electrode with DCEN polarity showed completely different mechanism with MG-50 wire electrode. The rare earth metal added to wire can reduced the work function of cathode electrode. The result of surface metal droplet temperature showed highest average temperate compared with other welding conditions and welding wire electrodes. The thermionic emission process with high current density can be achieved according to the relationship explained by Richardson-Dushman equation. Subsequently, the high electromagnetic force or Lorentz force can produced the strong plasma jet flow in arc axis. These strong plasma jet flow can produced the separation of Fe vapor and carbon dioxide plasma in arc column. Therefore, the arc plasma was consist of two- layer structure of high-temperature region of carbon dioxide plasma at the area apart of arc axis and low temperature region of Fe plasma in the area of arc axis. The highest electrical conductivity is located at carbon dioxide plasma at the area apart of arc axis and the electrical current goes through the arc at the region apart from the arc axis. Consequently, high electromagnetic force can pinch the metal droplet to a smaller size than wire electrode with high metal droplet frequency. Metal droplet transfer mode become spray transfer with less amount of spatter. The schematic illustration of mechanisms of gas metal arc welding with KC-500 wire electrode, DCEP polarity shows in Figure 5.1 (d).

Chapter 6

Conclusions

In this thesis the optical emission spectroscopic studies of plasma characteristics of gas metal arc welding have been presented in order to characterize the thermal plasma and metal droplet transfer behaviors. Difference topics such as the plasma main parameters, metal droplet behaviors for both consumable wire electrode, conventional carbon steel wire electrode (YGW11 MG-50) and rare earth metal added wire electrode (YGW11 KC-500) have been discussed. Further, the analysis of mixture shielding gas between carbon dioxide and argon been performed and their effect on rare earth metal element has been shown. An experimental set-up has been developed which allows these spectral lines simultaneously recorded at the same time during welding. The background spectral for spectrum line of oxygen and argon were subtracting the continuum spectra from a discrete spectral line. The evaluation method involves the Fowler-Milne method and Two-line relative intensity method with Able-inverted measured emission coefficients. Furthermore, high-speed video cameras with two-color temperature measurement algorithm has been used to measure surface metal droplet temperature.

An optical plasma diagnostics of a conventional carbon wire electrode with pure carbon dioxide shielding gas has been introduced which is based on the optical emission spectroscopic and the visualization of metal droplet transfer were obtained. It has been shown that the resulting intensity distributions of spectrum image of oxygen and argon were distributed near center of the arc column. This indicates that the carbon dioxide plasma and Fe plasma mix with each other in the arc column. Moreover, it has been shown that the highest plasma temperature was distributed at the center of the arc column. Similarly, the distribution of Fe vapor concentration shows the highest values over 60% mole fraction near the tip of wire electrode. The electrical conductivity distribution results shown maximum value located at the center of the arc column. It can be conjectured that the electrical current goes along the central axis of the arc column. The current density concentrates on the bottom tip of the metal droplet. When the current lines diverge in the droplet, the Lorentz force acts at right angles to these current lines. An increasing force in the lower part of the droplet which induces an upward movement of globule developed at the tip of the wire electrode. The metal transfer mode of this conventional wire electrode with pure carbon dioxide shielding gas become the globular transfer mode.

Also, 80% Ar + 20% CO_2 different shielding gas mixture used in industrial process has been analyzed the plasma characteristics and metal transfer behaviors. It has been seen that center of the arc column in globular transfer mode was composed mainly of argon and CO_2 as well as Fe, where the plasma temperature was around 7,500 K. During transition current, argon, CO_2 and Fe plasma tended to gradually change from localizing near the arc axis to a two–layer structure consisting of high–temperature region away from the arc axis and low–temperature region near the arc axis. With increases in welding current above 350 A, he metal transfer was spray transfer mode which the plasma temperature reached over 11,000 K away from the arc axis and around 7,000 K of Fe- reached region near the arc axis.

The effects of rare earth metal added in wire electrode of gas metal arc welding process have also been analyzed and compared to conventional carbon steel wire electrode. This part, the optical emission spectroscopic was successfully used to measure plasma main plasma parameters in GMAW with pure carbon dioxide shielding gas shielding gas. The results of rare earth metal added wire electrode (YGW11 KC-500) wire electrode with DCEN mode showed that the arc plasma had a dual structure consisting of a high-temperature region apart from the arc axis and a low temperature region near the arc axis due to the influence of the metal vapor. Moreover, the maximum electrical conductivity was located at apart of arc axis. It can be conjectured that the electrical current goes through the arc at the region apart from the arc axis. This was due to the lower work function of the rare earth metal elements giving the emission of electron more efficiently, resulting in a high pinching effect that can promote the droplet detachment like spray transfer. Unlike the YGW11 MG-50 wire electrode with pure carbon dioxide shielding gas shielding gas, the process does not exhibit a spray transfer mode. The result shows poor appearance of weld bead and high levels of spatter.

The effect of carbon dioxide and argon shielding gas composition on plasma characteristics of rare earth metal added wire electrode was also analyzed. By using YGW11 MG-50 wire electrode with the CO_2-reached shielding gas temperature drop was observed in the main part of the plasma column while the Fe vapor concentration seemed to increase towards the axis. The metal transfer mode was spray transfer mode with welding current above 250 A for pure carbon dioxide shielding gas.

Finally, the metal droplet temperature and thermionic emission are also influences on the plasma behavior of GMAW. From the results of metal droplet temperature of MG-50 wire electrode with DCEP polarity, the temperature at the lower area around arc root is higher locally. The electron can easily emitted from cathode base metal due to oxides on the base metal surface. However, the GMAW arc plasma with carbon dioxide shielding gas can cause high concentration of arc plasma and constricted arc near the bottom tip of wire electrode, resulting high electromagnetic force which induces an upward movement of globular transfer mode. Conversely, the high metal droplet temperature of KC-500 wire electrode with DCEN polarity can cause highly efficiency of thermionic emission process. Meanwhile, the thermionic emission process of wire electrode can produced high current density with high electromagnetic force at the arc axis. The strong plasma jet flow can produced the separation of Fe-vapor and carbon dioxide plasma. The metal transfer mode become spray transfer.

References

[1] Howard, B.C., and Scott, C.H., *Modern Welding Technology,* Fifth Edition, Pearson/Prentice Hall, New Jersey (2002), pp. 250-255.

[2] Manz, A.F., *Welding Power Handbook*, Union Carbide Corporation, Tarrytown, New York (1973), pp. 374-375.

[3] Althouse, A., Turnquist, C., Bowditch, W. and Bowditch, K., *Modern Welding*, Eleventh Edition, Goodheart-Willcox Publisher, South Holland, Illinois, (2012), pp. 142-145.

[4] American Welding Society, *Welding Handbook,* Eighth Edition, Vol. 2, *Welding Processes.* Miami, FL, American Welding Society, (1998), pp. 955.

[5] ASM International*, ASM Handbook. Welding, Brazing, and Soldering,* First Edition, Vol. 6, 1993: ASM International.

[6] Lincoln Electric Company, *The Procedure Handbook of Arc Welding,* Fourteenth Edition, The Lincoln Electric Company, (2000).

[7] Lancaster, J.F., *The Physics of Welding*, Second Edition, Oxford, Pergamon Press, (1986).

[8] Lesnewich, A.*, Control of Melting Rate and Metal Transfer in Gas-Shielded Metal-Arc Welding Part I - Control of Electrode Melting Rate*, Welding Journal. Vol. 37, No.8 (1958), pp. 343s-353s.

[9] IIW, *Classification of Metal Transfer,* Welding in the World, Vol. 15, No. 5/6, (1977), pp. 113-116.

[10] Amson, J.C., *Lorentz force in the molten tip of an arc electrode*, British Journal of Applied Physics, Vol. 16, (1965), pp. 1169-1179.

[11] Kim, Y.S. and Eagar, T.W., *Analysis of metal transfer in gas metal arc welding*, Welding Journal, Vol. 72, No. 6, (1993), pp. 269s-278s.

[12] Rhee, S. and Kannatey, A.E., *Observation of Metal Transfer during Gas Metal Arc Welding,* Welding Journal, Vol. 71, No. 11, (1992), pp. 381-386.

[13] Rhee, S. and Kannatey, A.E., *Analysis of Arc Pressure Effect on Metal Transfer in Gas-Metal Arc-Welding,* Journal of Applied Physics, Vol. 70, No.9, (1991), pp. 5068-5075.

[14] Waszink, J.H. and Graat, L.H.J., *Experimental Investigation of the Forces Acting on a Drop of Weld Metal,* Welding Journal, Vol. 62, No. 4, (1983), pp. 108s-116s.

[15] Spraragen, W., Bela, A., and Lengyel, *Physics of the Arc and the Transfer of Metal in Arc Welding,* Welding Journal Vol. 22, No.1, (1943), pp. 2-42.

[16] Muller, A., Greene, W.J., and Rothschild G.R., *Characteristics of Inert-Gas-Shielded Metal Arcs*, Welding Journal, Vol. 31, No. 8, (1951), pp. 717-727.

[17] Ludwig, H.C., *Metal Transfer Characteristics in Gas-Shielded Arc Welding*, Welding Journal, Vol.36, (1957), pp. 23s-26s.

[18] Haidar, J., *An analysis of the formation of metal droplets in arc welding,* Journal of Physics D: Applied Physics, Vol. 31 No.10 (1998), pp. 1233-1244.

[19] Chen, M.A., Wu, C.S., Li, S.K., and Zhang, Y.M., *Analysis of active control of metal transfer in modified pulsed GMAW [MIG/MAG welding]*, Science and Technology of Welding and Joining, Vol. 12, No. 1, (2007), pp. 10-14.

[20] Lincoln Electric Company, *The Procedure Handbook of Arc Welding,* Fourteenth Edition, The Lincoln Electric Company, (2000).

[21] Lancaster, J.F., *The Physics of Welding*. Second Edition, Oxford, Pergamon Press, (1986).

[22] Larry, J., *Welding Principles and Application*s, seventh Edition, Delmar Cengage Learning, Clifton Park, New York (2012).

[23] Haidar, J., and Lowke, J.J., *Effect of* CO_2 *shielding gas on metal droplet formation in arc welding*, IEEE Transactions on Plasma Science, Vol. 25, No.5, (1997), pp. 931-936.

[24] Cuiuri, D., Norrish, J., and Cook, C.D., *Novel Control Techniques for* CO_2 *Shielded Gas Metal Arc Welding*, Trends in Welding Research Proceedings of the 6th International Conference, (2003), pp. 979-984.

[25] Zielinska, S., Musiol, K., Dzierzega, K., Pellerin, S., Valensi, F., Izarra, de. C., and Briand, F., *Investigations of GMAW plasma by optical emission spectroscopy,* Plasma Sources Science and Technology, Vol. 16, (2007), pp. 832–838.

[26] Wilhelm, G., Gott, G., Schopp, H., and Uhrlandt, D., *Study of the welding gas influence on a controlled short-arc GMAW process by optical emission spectroscopy*, Journal of Physics D: Applied Physics, Vol. 43, (2010), 434004.

[27] Rouffet, M.E., Wendt, W., Goett, G., Kozakov, R., Schoepp, H., Weltmann, K.D., and Uhrlandt, D., *Spectroscopic investigation of the high-current phase of a pulsed GMAW process,* Journal of Physics D: Applied Physics, Vol. 43, (2012), 434003.

[28] Valensi, F., Pellerin, S., Boutaghane, A., Dzierzega, K., Zielinska, S., Pellerin, N. and Briand, F., *Plasma diagnostics in gas metal arc welding by optical emission spectroscopy*, Journal of Physics D: Applied Physics, Vol. 43, (2010), 434002.

[29] Schnick, M., Fuessel, U., Hertel, M., Haessler, M., Spille-Kohoff, A., and Murphy, A.B., *Modelling of gas–metal arc welding taking into account metal vapour*, Journal of Physics D: Applied Physics, Vol. 43, (2010), 434008.

[30] Lu, S., Fuji, H., and Nogi, K., *Marangoni convection in weld pool in* CO_2*–Ar-shielded gas thermal arc welding,* Metallurgical and Materials Transactions, Vol. 35, (2004), pp. 2861–2867.

[31] Lu, S., Fuji, H., and Nogi, K., *Weld shape variation and electrode oxidation behavior under Ar-(Ar-CO2) double shielded GTA welding,* Journal of Materials Science & Technology Vol. 26, (2010), pp. 170–176.

[32] Poopat, B., and Warinsiriruk, E., *Investigation of parameters affecting behavior of Metal transfer in MAG-M welding process: The effect of shielding gas composition*, The Second South-east Asia International Welding Congress, (2010), pp. 128–137.

[33] Soonrach, R., and Poopat, B., *Effect of oxygen addition in argon/carbon dioxide gas mixture on metal transfer behavior in gas metal arc welding,* International Journal of Mechanical and Production Engineering, Vol. 4, (2016), pp. 50–45.

[34] Boulos, M.I., Fauchais, P., and Pfender, E., *Thermal Plasmas Fundamentals and Applications, Vol. 1*, Springer, New York (1994).

[35] Tanaka, Y., Yamachi, N., Matsumoto, S., Kaneko, S., Okabe, S., and Shibuya, M., *Thermodynamic and Transport Properties of* CO_2*,* CO_2*–*O_2*, and* CO_2*–*H_2 *Mixtures at Temperatures of 300 to 30,000 K and Pressures of 0.1 to 10 MPa,* Electrical Engineering in Japan, Vol. 163, No. 4, (2008), pp. 18-28.

[36] Węglowski, M., *Investigation on the arc light spectrum in GTA welding*, Journal of Achievements in Materials and Manufacturing Engineering, Vol. 20, No. 1, (2007), pp. 519-522.

[37] Hinrichs, J.F., *Radiation and arc welding: New data to enhance safety*, Welding and Metal Fabrication, Vol. 51, No. 2, (1978), pp. 102-103.

[38] Pattee, H.E., Myers, L.B., Evans, R.M., and Monroe, R.E., *Effect of Arc Radiation and Heat on Welders*, Welding Journal, Vol. 52, No. 5, (1973), pp. 297-308.

[39] Kohmoto, K., *Variation of degree of blue light hazardous damage by the crystalline lens deterioration*, Document International Institute of Welding MIS VIII-1630-92, (1992).

[40] Kennebeck, M., *Eye Damage from Radiation in Arc Welding: Recognition Evaluation and control*, Welding in the World, Vol. 33, No. 1, (1994), pp. 14-16.

[41] Bennett, A.P., and Harlem, F., *Measuring the UV radiation hazard to welders* Welding and Metal Fabrication, Vol. 48, No. 10, (1980), pp. 541-549.

[42] Agapiou, G., and Kasiouras, C., *A detailed analysis of the MIG spectrum for the development of laser-based seam tracking sensor*, Optics & Laser Technology, Vol. 31, No. 2, (1999), pp. 157-161.

[43] Li, P.J., and Zhang, Y.M., *Precision Sensing of Arc Length in GTAW Based on Arc Light Spectrum*, Journal of Manufacturing Science and Engineering, Vol. 123, No. 1, (2001), pp. 62-65.

[44] Ton, H., *Physical properties of the plasma–MIG welding arc*, Journal of Physics D: Applied Physics, Vol. 8, (1975), pp. 922–933.

[45] Zielinska, S., Pellerin, S., Dzierzega, K., Valensi, F., Musiol, K., and Briand, F., *Measurement of atomic Stark parameters of many Mn I and Fe I spectral lines using GMAW process*, Journal of Physics D: Applied Physics, Vol. 43, (2010), pp. 1-9.

[46] Pellerin, S., Musiol, K., Pokrzywka, B., and Chapelle, J., *Investigation of a cathode region of an electric arc*, Journal of Physics D: Applied Physics, Vol. 27, (1994), pp. 552-528,

[47] Bockasten, K., *Transformation of observed radiances into radial distribution of the emission of a plasma*, Journal of the Optical Society of America, Vol. 51, No. 9, (1961), pp. 943 - 947.

[48] Griem, H.R., *Plasma Spectroscopy,* McGraw-Hill, New York. (1964).

[49] DAIHEN Corporation, *Owner's manual for digital inverter DM350, Model: DM-350 P10322,* (2003), Retrieved from http://www.daihen.co.jp/.

[50] DAIHEN Corporation, *Owner's manual for wire feeder Model: CM-741 U5278*, (2003), Retrieved from http://www.daihen.co.jp/.

[51] DAIHEN Corporation, *Owner's manual for blue torch Model: WTCX-3503 U4167*, (1998), Retrieved from http://www.daihen.co.jp/.

[52] Intelligent Actuator Inc., *Product overview brochure for ROBO Cylinders RCS2-SA7C,* (2017), Retrieved from https://www.intelligentactuator.com/pdf/Product _Overview_CE0033-28.6A_EN_LTR_20170706.pdf.

[53] Princeton Instruments, Inc., *Operating Instructions Acton Series SpectraPro-2300i, 0.300 Meter Focal Length Triple Grating Imaging Monochromator / Spectrograph*, (2015), Retrieved from ftp://ftp.princetoninstruments.com/public/Manuals/Acton/ SP-2300i.pdf.

[54] NAC Image Technology, Inc., *Product overview brochure for MEMRECAM GX-1, High Speed Camera System,* (2014) Retrieved from http://www.nacinc.com /datasheets/archive/ Memrecam_GX-1.pdf.

[55] JFE Steel Corporation, *Steel plate specification*, (2007), Retrieved from http://www.jfe-steel.co.jp/en/products/plate/catalog/c1e-001.pdf.

[56] KOBE Steel, Ltd., *Welding business, FAMILIARC, MG-50 specification*, (2016), Retrieved from http://www.kobelco.co.jp/english/welding/files/handbook2016.pdf

[57] Kataoka, T., and Ikeda, R., *Development of ultra-low spatter* CO_2 *gas-shielded arc welding process J-STAR® welding,* JFE Technical report. No. 10, (2007), pp. 31-33.

[58] Kramida, A., Ralchenko, Y., Reader, J., and NIST ASD Team., *NIST Atomic Spectra Database (ver. 5.3),* [Online]. Available: http://physics.nist.gov/asd. National Institute of Standards and Technology, Gaithersburg, Maryland, (2015).

[59] Murphy, A.B., *Transport coefficients of air, argon-air, nitrogen-air, and oxygen-air plasmas*, Plasma Chemistry and Plasma Processing, Vol. 15, (1995), pp. 279-307.

[60] Cram, L.E., *Statistical evaluation of radiative power losses from thermal plasmas due to spectral lines*, Journal of Physics D: Applied Physics, Vol. 18, (1985), pp. 401-411.

[61] Menart, J., and Malik, S., *Net emission coefficients for argon-iron thermal plasmas*, Journal of Physics D: Applied Physics, Vol. 35, (2002), pp. 867-874.

[62] Ozawa, M., and Morita, T., *The measurement of heat quantity in melted metals*, Quarterly Journal of the Japan Welding Society, Vol. 32, No. 2, (1963), pp. 130-137.

[63] Ando, K., Nishiguchi, K., and Fukuda, K., *Temperature characteristics of the droplet detaching from the wire tip in MIG welding*, Quarterly Journal of the Japan Welding Society, Vol. 36, No. 10, (1967), pp. 1117–1123.

[64] Maruo H, Hirata Y, and Noda Y., *Heat contents and temperature of metal droplets in pulsed MIG welding*, Quarterly Journal of the Japan Welding Society, Vol. 2 No. 4, (1984), pp. 573–578.

[65] Hirata, Y., Onda, M., Nagaki, H., and Ohji, T., *In-situ measurement of metal drop temperature in GMA short-circuiting welding*, Journal of High Temperature Society, Vol. 30, No. 3, (2004), pp. 140–147.

[66] Schnick, M., Füssel, U., and Hertel, M., *Metal vapour causes a central minimum in arc temperature in gas–metal arc welding through increased radiative emission*, Journal of Physics D: Applied Physics, Vol. 43, (2010), 022001.

[67] Lesnewich, A., *Electrode Activation for Inert-Gas-Shielded Metal-Arc Welding*, The Welding Journal, Vol. 34, No.12, (1955), pp. 1167-1178.

[68] Guile, A.E., *Arc-Electrode Phenomena*, Proceeding of IEE, IEE Reviews, Vol. 118, No.9, (1971), pp. 1131-1154.

[69] Ozcelik, S., and Moore, K., *Modeling, Sensing and Control of Gas Metal Arc Welding,* First Edition, Elsevier Science Ltd., Kidlington, Oxford, (2003).

[70] Scotti, A., Ponomarev, V., and Lucas, W., *A scientific application oriented classification for metal transfer modes in GMA welding*, Journal of Materials Processing Technology, Vol. 212, (2012), pp. 1406-1413.

[71] Matsuda, F., Ushio, M., and Kumagai, T., *Comparative study on fundamental arc characteristics with La-, Y-, Ce-oxide tungsten electrodes*, Quarterly Journal of the Japan Welding Society, Vol.6, No.2, (1988), pp. 199-204.

[72] Tashiro, S., and Tanaka, M., *Electrode and weld pool phenomena in arc welding*, Journal of Plasma and Fusion Research SERIES, Vol. 88, No. 7, (2012), pp. 383-388.

[73] Hartnett, J., *Advances in Heat Transfer: Transport Phenomena in Plasma,* Vol. 40, AE Amsterdam, Academic Press, (2007), pp. 440-442.

[74] Nguyen, N.P., Katada Y., Tanaka, Y., Uesugi, Y., and Yamaguchi, Y., *Cathode diameter and operating parameter effects on hafnium cathode evaporation for oxygen plasma cutting arc*, Journal of Physics D: Applied Physics, Vol. 45, (2012), pp. 11-12.

[75] Haidar, J., and Farmer A.J.D., *Surface temperature measurements for tungsten-based cathodes of high-current free-burning arcs*, Journal of Physics D: Applied Physics, Vol. 28, (1995), pp. 2089-2094.

[76] Shigeta M., Nakanishi S., Tanaka M., and Muephy A.B., *Analysis of dynamic plasma behaviours in gas metal arc welding by imaging spectroscopy,* Welding International, Vol. 31, No. 9, (2017), pp. 669 – 680.

Appendix A: Arc appearance of GMAW at difference time variation using YGW 11 MG 50

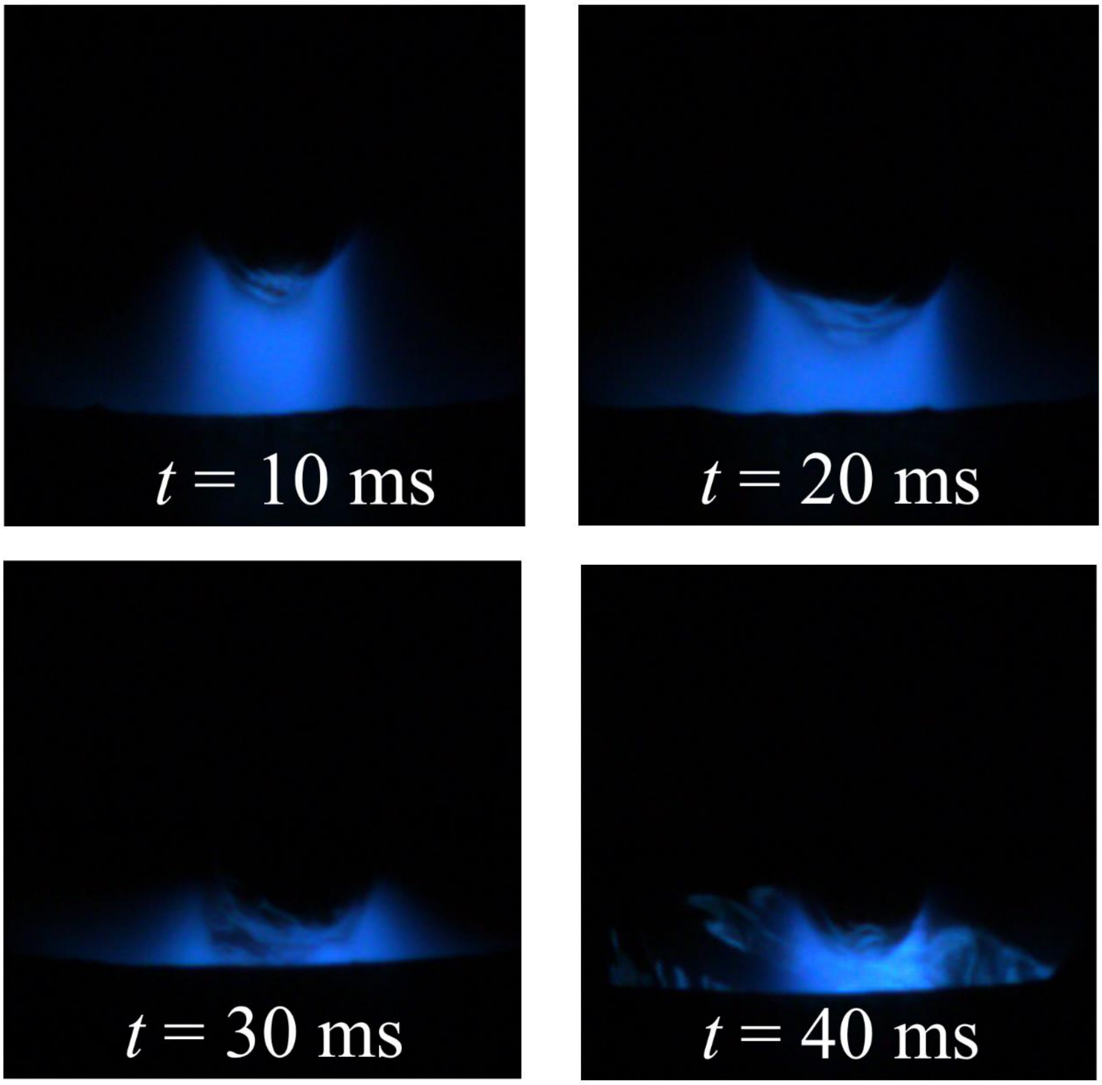

Figure A.1 Arc appearance of GMAW at difference time variation using YGW 11 MG 50 electrode in welding current of 300 A with carbon dioxide shielding gas, DCEP polarity.

Remark: From Figure A.1, the time after droplet detachment is t = 10 ms. It can be seen that the arc plasma was preformed axisymmetric arc plasma.

Appendix B Arc appearance of GMAW at difference time variation using YGW 11 KC 500

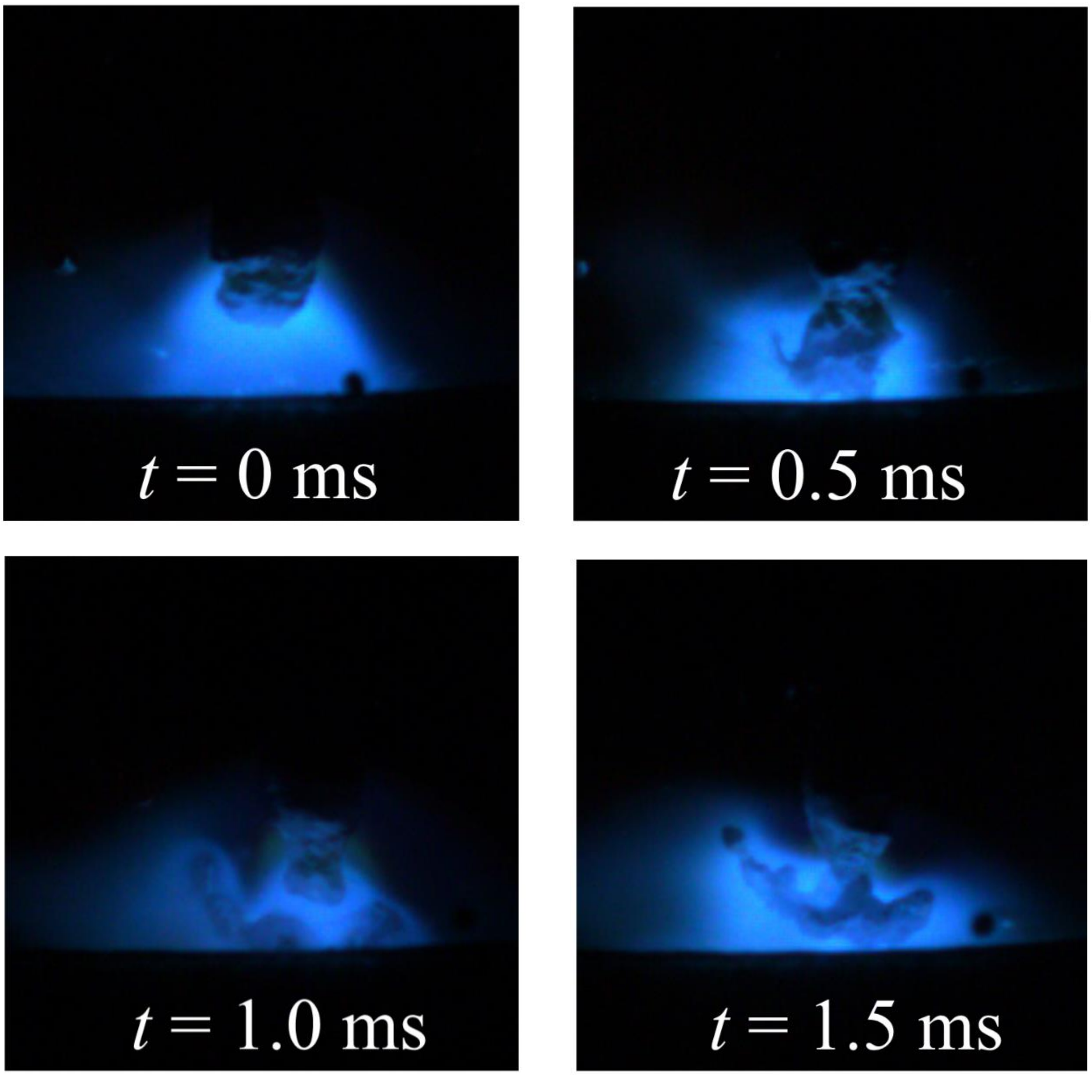

Figure B.1 Arc appearance of GMAW at difference time variation using YGW 11 KC 500 electrode in welding current of 300 A with carbon dioxide shielding gas, DCEN polarity.

Remark: From Figure B.1, the time after droplet detachment is *t* = 0 ms. It can be seen that the arc plasma was preformed axisymmetric arc plasma.

Lit of publications

Peer-reviewed manuscript

1. Titinan Methong, Masaya Shigeta, Manabu Tanaka, Rinsei Ikeda, Muneo Matsushita and Tokihiko Kataoka, *Diagnostic of heat source characteristics in gas metal arc welding using CO_2 shielding gas*, Quarterly Journal of The Japan Welding Society， Vol. 35, No. 2 (2017), page 103s-107s.
2. Titinan Methong, Tasuku Yamaguchi, Masaya Shigeta, Manabu Tanaka, Rinsei Ikeda, Muneo Matsushita and Bovornchok Poopat, *Effect of rare earth metal on plasma properties in GMAW using CO_2 shielding gas*, Welding in the World, Vol. 61, Issue 5, Page 1039-1047. DOI: 10.1007/s40194-017-0491-4.
3. Titinan Methong, Masaya Shigeta, Manabu Tanaka, Rinsei Ikeda, Muneo Matsushita and Bovornchok Poopat, *Visualization of gas metal arc welding on globular to spray transition current*, Science and Technology of Welding and Joining. Vol. 23, No. 1, Page 87-94. DOI: 10.1080/13621718.2017. 1344454.
4. Sarizam Bin Mamat, Titinan Mething, Shinichi Tashiro and Manabu Tanaka, *Droplet temperature measurement in metal inert gas welding process by using two color temperature measurement method,* Quarterly Journal of The Japan Welding Society， Vol. 35, No. 2 (2017), page 160s-164s.
5. Toshifumi Yuji, Shinichi Tashiro, Atsushi Fujimaru, Hiroyuki Kinoshita, Kentaro Yasui, Toshio Bouno, Titinan Methong, Manabu Tanaka, *Observation of the Behavior of Cathode Spots in AC Tungsten Inert Gas Welding on Aluminum Plate*, Quarterly Journal of The Japan Welding Society，Vol. 33, No. 2 (2015), page 135s-138s.
6. Kentaro Yasui, Hiroyuki Kinoshita, Toshifumi Yuji, Atsushi Fujimaru, Toshio Bouno, Shinichi Tashiro, Titinan Methong and Manabu Tanaka, *Proposal of a method of observing cathode spots in AC tungsten inert gas welding*, Advanced Experimental Mechanics, Vol.1 (2016), page 231-236.
7. Toshifumi Yuji, Shinichi Tashiro, Titinan Methong, Hiroyuki Kinoshita, Kentaro Yasui, Toshio Bouno, Noritsugu Kamata, Le Huy Phan and Manabu Tanaka, *Influence of admixture of oxygen into shielding gas on cathode spot behavior*, Quarterly Journal of The Japan Welding Society, Vol. 35 No. 2 (2017), page 47s-50s.

Conference proceedings:

8. Titinan Methong, Masaya Shigeta, Manabu Tanaka, Rinsei Ikeda and Muneo Matsushita, *Influence of Ar-CO$_2$ mixtures on plasma characteristics of rare earth metal-added wire electrode in gas metal arc welding*, The National Symposium on Smart Processing Society for Materials, Environment & Energy, Tokyo, Japan (2017); National Conference (Proceedings and oral presentation).
9. Titinan Methong, Masaya Shigeta, Manabu Tanaka, Rinsei Ikeda, Muneo Matsushita and Tokihiko Kataoka, *Plasma Characteristics of Gas Metal Arc Welding on Globular Spray Transition Current*, the International Welding and Inspection Technology 2017 (IWIT2017), Chantaburi, Thailand; International Conference (Proceedings and oral presentation).
10. Titinan Methong, Masaya Shigeta, Manabu Tanaka, Rinsei Ikeda and Muneo Matsushita *Effect of Shielding Gas Composition on Plasma Characteristics of Rare Earth Metal-added Wire Electrode in Gas Metal Arc Welding*, Japan Welding Society National Conference, Kyushu, Japan (2017); National Conference (Proceedings and poster presentation).
11. Keigo Tanaka, Titinan Methong, Masaya Shigeta and Manabu Tanaka, *Spectroscopic Observation of Dynamic Metal Vapor Behavior in Gas Tungsten Arc Welding*, 70th Annual Assembly of International Institute of Welding (IIW), Shanghai, China (2017); International Conference (Proceedings and oral presentation).
12. 田中　慶吾, Methong Titinan, 茂田　正哉, 田中　学, GTA溶接におけるアークプラズマ中の金属蒸気挙動の観測, （一社）スマートプロセス学会　平成29年度　春季総合学術講演会,大阪, (2017.05.23).
13. 田中　学, 茂田　正哉, Methong Titinan, 池田　倫正, 松田　広志, 松下　宗生, 澤西　央海, REM添加ワイヤを用いたGMA溶接におけるアークプラズマ現象, （一社）溶接学会第238回溶接法研究委員会,東京,(2017.05.15), SW-3674-17.
14. 田中　慶吾, Methong Titinan, 茂田　正哉, 田中　学, GTA溶接におけるアークプラズマ中の金属蒸気挙動の可視化, （一社）溶接学会　平成29年度春季全国大会,東京,(2017.04.19-21).

15. Titinan Methong, Masaya Shigeta, Manabu Tanaka, Rinsei Ikeda, Muneo Matsushita and Tokihiko Kataoka, *Visualization of gas metal arc welding process on globular spray transition current*, International Welding & Joining Conference (IWJC), Gyeongju, Korea (2017); International Conference (Proceedings and oral presentation).
16. Keigo Tanaka, Titinan Methong, Masaya Shigeta and Manabu Tanaka, *Visualization of Metal Vapor Behavior in Gas Tungsten Arc Welding using Helium Gas*, International Welding & Joining Conference (IWJC), Gyeongju, Korea (2017); International Conference (Proceedings and oral presentation).
17. Titinan Methong, Masaya Shigeta, Manabu Tanaka, Rinsei Ikeda, Muneo Matsushita and Tokihiko Kataoka, *Experimental study of the influence of rare earth metal on the plasma properties of* CO_2 *gas metal arc welding*, The National Symposium on Smart Processing Society for Materials, Environment & Energy, Osaka, Japan (2016); National Conference (Proceedings and oral presentation).
18. Titinan Methong, Masaya Shigeta, Manabu Tanaka, Rinsei Ikeda, Muneo Matsushita and Tokihiko Kataoka, *Diagnostic of heat source characteristics in gas metal arc welding using* CO_2 *shielding gas,* The International Symposium on Visualization in Joining & Welding Science through Advanced Measurements and Simulation (Visual-JW 2016), Osaka, Japan (2016); International Conference (Proceedings and poster presentation).
19. Keigo Tanaka, Titinan Methong, Masaya Shigeta and Manabu Tanaka, *Observation of metal vapor behavior during gas tungsten arc welding using helium gas*, The International Symposium on Visualization in Joining & Welding Science through Advanced Measurements and Simulation (Visual-JW 2016), Osaka, Japan (2016); International Conference (Proceedings and poster presentation)
20. Sarizam Bin Mamat, Titinan Methong, Shinichi Tashiro and Manabu Tanaka, *Droplet temperature measurement in gas metal arc welding process by using two color measurement method*, The International Symposium on Visualization in Joining & Welding Science through Advanced Measurements and Simulation (Visual-JW 2016), Osaka, Japan (2016); International Conference (Proceedings and poster presentation).

21. Toshifumi Yuji, Shinichi Tashiro, Titinan Methong, Hiroyuki Kinoshita, Kentaro Yasui, Toshio Bouno, Noritsugu Kamata and Manabu Tanaka, *Influence mixture of oxidant into shielding gas on cathode spot behavior,* The International Symposium on Visualization in Joining & Welding Science through Advanced Measurements and Simulation (Visual-JW 2016), Osaka, Japan (2016); International Conference (Proceedings and poster presentation).
22. Keigo Tanaka, Titinan Methong, Masaya Shigeta, Manabu Tanaka and Anthony B. Murphy, *Measurement of metal vapor behavior in helium plasma during gas tungsten arc welding*, Proceedings of the 31st International Congress on High-Speed Imaging and Photonics, Osaka, Japan (2016) page 616-618; International Conference (Proceedings).
23. Titinan Methong, Masaya Shigeta, Manabu Tanaka, Rinsei Ikeda, Muneo Matsushita, and Tokihiko Kataoka, *Experimental study of the influence of rare earth metal on the plasma properties of gas metal arc welding*, Japan Welding Society National Conference, Gunma, Japan (2016); National Conference (Proceedings and poster presentation).
24. Titinan Methong, Tasuku Yamaguchi, Masaya Shigeta, Manabu Tanaka, Rinsei Ikeda, Muneo Matsushita and Tokihiko Kataoka, *Effect of rare earth metal on plasma properties in GMAW using* CO_2 *shielding gas*, 69th Annual Assembly of International Institute of Welding (IIW), Melbourne, Australia (2016), IIW Doc.212-1435-16; International Conference (Proceedings and oral presentation).
25. Titinan Methong and Manabu Tanaka, *Arc physical properties with droplet transfer phenomenon of gas metal arc welding*, International Institute of Welding 6th Welding Research and Collaboration Colloquium, Hyderabad, India (2016); International Conference (Proceedings and oral presentation).
26. Titinan Methong and Manabu Tanaka, *Study of the plasma behaviors in gas metal arc welding with droplet transfer phenomenon by spectroscopic investigation,* Commission I, IV, XII and SG 212, Intermediate Meeting of International Institute of Welding (IIW), Istituto Italiano della Saldatura (IIS), Genova, Italy (2016), IIW Doc.212-1409-16; International Conference (Proceedings and oral presentation).

27. Titinan Methong, Masaya Shigeta, Manabu Tanaka, Rinsei Ikeda, Muneo Matsushita, and Tokihiko Kataoka, *Plasma diagnostics in* CO_2 *gas shielded arc welding*, Japan Welding Society National Conference, Hokkaido, Japan (2015); National Conference (Proceedings and poster presentation).

Acknowledgements

First and foremost I would like to express my sincere appreciation to my principal supervisor, Professor Manabu Tanaka, Department of Energy control of processing, Joining and Welding Research Institute for giving me the chance to work in his institute and their constant guidance and encouragement. I would also like to thank my doctoral committee members, Professor Hiroshige Inoue, Department of Reliability Evaluation and Simulation, Joining and Welding Research Institute and Professor Satoru Asai, Division of Materials and Manufacturing Science, Graduate School of Engineering for serving as my committee members even at hardship. I am also grateful to all lectures and staff in the Joining and Welding Research Institute (JWRI) and extension in particular, especially Associate Professor Masaya Shigeta and Assistant Professor Shinichi Tashiro for the numerous helpful discussions and very valuable comments on this research.

Further, I would like to thank Dr. Rinsei Ikeda and Dr. Muneo Matsushita from JFE Steel Corporation who provided me a consumable wire electrode to perform experimental studies in this research and the support towards the successful completion of my studies.

I would like to thank Mr. Hisaya Komen, Mr.Tasuku Yamaguchi, Mr. Kyohei Konishi, Mr. Sarizam Bin Mamat and Mr. Keigo Tanaka who were sparkling sources of ideas for the solution of many technical challenges. They were always encouraging and their guidance helped me in the pursuit of my research goals. Many thanks also go to my colleagues from the Department of Energy Control Processing, JWRI for their friendly collaboration over many years, their contribution to all my tasks, the excellent working atmosphere and friendly cooperation.

I would also like to thank Associate Professor Bovornchok Poopat of King Mongkut’s University of Technology Thonburi who was reading my research paper and for interesting discussions. Without his encouragement and constant guidance, I could not have finished my research paper and this dissertation.

Also I would especially like to thank Fonthip Chuprasert for giving me the motivation and unlimited support to realize this achievement. Finally I wish to thank my family for their never ending love and support.

Titinan Methong
January2018